ÉCOLE DE TECHNOLOGIE SUPÉRIEURE
UNIVERSITÉ DU QUÉBEC

THESIS PRESENTED TO
ÉCOLE DE TECHNOLOGIE SUPÉRIEURE

IN PARTIAL FULFILLMENT OF THE REQUIREMENTS FOR
THE DEGREE OF DOCTOR OF PHILOSOPHY
Ph. D.

BY
Rachid Bekhti

GEOMETRICAL, MECHANICAL AND TRANSDUCTION TECHNIQUES FOR DESIGNING MULTI-AXIS FORCE-TORQUE SENSORS FOR ROBOTIC APPLICATIONS

MONTREAL, "DECEMBER 14TH, 2015"

BOARD OF EXAMINERS

THIS THESIS HAS BEEN EVALUATED

BY THE FOLLOWING BOARD OF EXAMINERS:

Prof. Vincent Duchaine, Thesis Supervisor
Department of Automated Manufacturing Engineering at École de Technologie Supérieure

Prof. Philippe Cardou, Thesis Co-supervisor
Department of Mechanical Engineering at Laval University

Prof. Philippe Bocher, President of the Board of Examiners
Department of Mechanical Engineering at École de Technologie Supérieure

Prof. Ilian Bonev, Member of the Jury
Department of Automated Manufacturing Engineering at École de Technologie Supérieure

Prof. Alexis Lussier Desbiens, External Evaluator
Department of Mechanical Engineering at Sherbrooke University

THIS THESIS WAS PRESENTED AND DEFENDED

IN THE PRESENCE OF A BOARD OF EXAMINERS AND THE PUBLIC

ON "DEFENSE DATE"

AT ÉCOLE DE TECHNOLOGIE SUPÉRIEURE

ACKNOWLEDGEMENTS

This thesis is dedicated to:

my parents, Nakhla and Mohammed,

my siblings, Karima, Hayat and Sid-Ahmed,

and my girlfriend, Kate,

for all of their support and encouragement.

"One hand can't applaud." Algerian proverb

First I must thank my supervisor, Professor Vincent Duchaine, for his daily coaching, his support, his competency and his investment in my learning and in the follow-up to this work. I would like to thank my Co-supervisor, Professor Philippe Cardou, for his long-distance help with this thesis, his rigorous overview and insightful opinions, and with a special thought to all those long Skype meetings! I am also grateful to the rest of my thesis committee for evaluating my research: Prof. Ilian Bonev, Prof. Philippe Bocher, and Prof. Alexis Lussier Desbiens.

Thanks to my colleagues at the CoRo laboratory for their happiness and positive attitude.

And thank you to my parents, to my siblings, to Kate... and all those who have supported me during these years.

ASPECTS GÉOMÉTRIQUES, MÉCANIQUES ET DE TRANSDUCTION POUR LA CONCEPTION DE CAPTEURS DE FORCE ET DE COUPLE MULTI-AXES POUR DES APPLICATIONS EN ROBOTIQUE

Rachid Bekhti

RÉSUMÉ

Ce projet s'inscrit dans l'effort initié par Vincent Duchaine, professeur au laboratoire de Commande et de Robotique (CoRo), afin d'améliorer l'interaction physique entre les humains et les robots. Un aspect important de ce projet concerne le retour de force et la capacité du robot à sentir les forces qui lui sont appliquées. Afin de mesurer les forces exercées par exemple sur le poignet d'un robot humanoïde, les capteurs de force et de couple multi-axes sont essentiels. À l'aide de ces capteurs, le robot peut détecter les obstacles, éviter les collisions et faire le travail en toute sécurité. Nous émettons l'hypothèse qu'une meilleure qualité de mesure de la force associée à une strategie de commande en force pourrait contribuer à améliorer la dextérité de ces robots.

À cette fin, nous visons à élaborer de nouvelles méthodes pour concevoir les structures compliantes qui forment le cœur de ces capteurs de force et de couple multi-axes. Les capteurs qui en résulte doivent être sensibles, avec un spectre de force suffisant et capable de mesurer des forces dans toutes les directions. En outre, ils doivent être abordable et compact pour être intégré facilement dans des systèmes robotiques. Cette thèse tente de répondre à trois questions fondamentales: *1*) Quel est le meilleur indice de performance pour évaluer la géométrie de la structure compliante? *2*) Quelle est la meilleure méthode systématique pour concevoir la structure mécanique? et *3*) Quelle est la meilleure technique de transduction pour une meilleure compacité du capteur?

Nous avons commencé notre recherche en examinant le modèle géométrique du capteur pour comprendre les équations par lequel la force et le couple sont calculés. En se basant sur cette analyse, deux indices de performance sont proposées et validées. Nous avons ensuite examiné comment le comportement et les propriétés mécaniques de la structure compliante peuvent être utilisées pour transmettre une estimation précises des forces. Grâce à une méthode de conception systématique avancée basée sur une formulation symbolique de la relation force-déplacement, nous avons conçu un capteur de force triaxial compacte et économique. Notre capteur utilise un seul élement sensible basée sur la technologie capacitive pour détecter efficacement les différentes forces. Afin d'améliorer la conception de l'élément sensible, nous avons proposé une nouvelle technique de transduction. Cette technique nous a permis de construire un élement sensible multiaxial capable de détecter les composantes de la contrainte mécanique–à savoir la contrainte normale, contrainte de cisaillement et de couple. Cette utilisation innovante d'un élement sensible multiaxial nous a permis de réduire la taille du réseau des éléments sensibles et par conséquent de réduire les dimensions globale et le coût du capteur de force et de couple multi-axes. Dans une série d'expériences, nous avons vérifié que notre

élement sensible multiaxial peut mesurer avec succès plusieurs forces, prouvant qu'il est prêt à être utilisé dans de nombreuses applications robotiques.

Mots clés: Capteur force-couple, processus de conception, optimisation structurelle, techniques de transduction

GEOMETRICAL, MECHANICAL AND TRANSDUCTION TECHNIQUES FOR DESIGNING MULTI-AXIS FORCE-TORQUE SENSORS FOR ROBOTIC APPLICATIONS

Rachid Bekhti

ABSTRACT

This project is part of the effort initiated by Vincent Duchaine, Professor at the laboratory of Control and Robotics (CoRo), to enhance the physical interaction between humans and robots. An important aspect of this initiative concerns the force feedback and the ability of the robot to feel the forces that are applied to it. To measure the forces that are exerted on, for instance, a humanoid robot's wrist, multi-axis force-torque sensors are essential. With these sensors, the robot can detect obstacles, avoid collisions, and get the job safely done. We hypothesize that the ability to accurately detect the force measurements that are associated with force control will help to improve the dexterity of such robots.

To this end, we aim to develop new methods for designing the compliant structures that form the core of multi-axis force-torque sensors. The resulting sensors must be highly sensitive to a sufficient range of forces, and they must be capable of measuring forces in all directions. Moreover, they must be compact, so that they can be easily integrated within robotic structures; and of course, they must be cost-effective. This thesis attempts to answer three questions: *1*) What is the best performance index for evaluating the geometry of the compliant structure? *2*) What is the best systematic method to use for designing the mechanical structure? and *3*) What is the best transduction technique for achieving a compact sensor design?

We began our research by investigating the geometric model of the sensor, to better understand the equations by which the force and torque are computed. Based on this analysis, we proposed two performance indices, which we then validated. We next investigated how the behavior and the mechanical proprieties of the structure can be used to convey accurate estimates of the forces. Through an advanced systematic design method, based on a symbolic formulation of the wrench-displacement relationship, we designed a compact and cost-effective triaxial force sensor. Our sensor uses a single capacitive sensing element to detect several forces efficiently. In order to improve the design of the sensing element, we proposed a new transduction technique. This technique allowed us to build a multi-axial sensing element that is able to separate stress components of normal stress, shear stress, and torque. This innovative use of a single multi-axial sensing element allowed us to reduce the size of the network of sensing elements, and consequently lower the total dimensions and cost of the multi-axis force-torque sensor. In a series of experiments, we verified that our multi-axial sensing element can successfully measure multiple forces, proving that it is ready for use in numerous robotic applications.

Keywords: Force-torque sensor, design process, structural optimization, transduction techniques

CONTENTS

Page

LIST OF TABLES

Page

LIST OF FIGURES

Page

LIST OF ABREVIATIONS

3D	Three-Dimensional space
CoRo	Control and Robotics Laboratory
ÉTS	École de Technologie Supérieure
SCALPP	Système de Coupe Automatisé pour Le Prélèvement de Peau en chirurgie des brûlés et orthopédie
FEM	Finite Element Method
CCD	Charge-Coupled Device
GPA	Département de génie de la production automatisée
GUI	Graphic User Interface
DoF	Degrees of Freedom
GISE	Global Index of the Structural Error
LISE	Local Index of the Structural Error
MEAI	Measurement Error Amplification Index
PRR	Prismatic–Revolute–Revolute
RR	Revolute–Revolute
CPM	Cross-Product Matrix
FEA	Finite Element Analysis
CAD	Computer-Aided Design
CDC	Capacitive to Digital Converters
PCB	Printed Circuit Board

PMN-PT	Lead Magnesium Niobate-Lead Titanate
CNC	Computer (or Computerized) Numerical Control
AD	Analog Devices
ASIC	Application-Specific Integrated Circuit
PIC	Peripheral Interface Controller
AD	Analog to Digital
DPSS	Diode-pumped solid-state laser
UV	Ultra-Violet

LISTE OF SYMBOLS AND UNITS OF MEASUREMENTS

min	Minutes
sec	Seconds
°	Degrees
rad	Radian
mm	Millimeter
m	Meter
µm	Micrometer
"	Inches
kHz	Kilohertz
°C	Degrees Celsius
N	Newton
Nm	Newton meter
Nm/rad	Newton meter per radian
MPa	Megapascal

CHAPTER 1

INTRODUCTION

This chapter sets out the background information of the strategy we adopted for the design and optimization of multi-axis force-torque sensors. First, we present some key definitions regarding this technology, and give examples of their applications. We explore the various ways to design such sensors, and consider the limitations of each approach. We then describe the three directions – geometrical, mechanical, and transducer optimization – from which we will approach our design. The chapter concludes with an overview of the rest of our research, wherein we will address each of the issues we have considered.

1.1 Multi-axis force-torque sensors: definitions and applications

The term “force sensor" was introduced with the invention of force-sensing resistors (FSR), which were first patented by Franklin Eventoff in 1977. Like the gyroscope for orientation, and the camera for images, multi-axis force-torque sensors provide information related to the sense of touch. This sensory information can then be used to improve the performance of robots during object-manipulation tasks.

Currently in the field of robotics, a multi-axis force-torque sensor is a system that can measure up to six components of force and torque. Unlike the actuators that are hidden inside various parts of the robot, the multi-axis force-torque sensor is located externally and acts as an extension of the robot. It can be placed on a specific part of the robot’s body like the hand, arm, or leg, or on many parts at the same time. The system is equipped with a compliant structure, which combines sensing elements inside a shielded cover, with a flexible cable, and intelligent data acquisition system. The system has two roles: it first measure forces and torques from all three directions (x, y and z), and then it transmits these data to the robot for interpretation and real-time force control.

Generally speaking, we can separate force-torque sensors into three broad categories. The first type are called uni-axial sensors, since they can measure a force or torque applied in one direction only. Their working principle is based on a simple shaped element, with one or more uni-axial strain gauges mounted on the element to detect the mechanical tension or the strain. These sensors are specifically designed to provide high resolution and low deflection. Their robust construction, low price, and reliability make them suitable for applications requiring highly accurate static force measurements. Many uni-axial sensors have been developed as commercial products, such as the ones depicted in Figure 1.1.

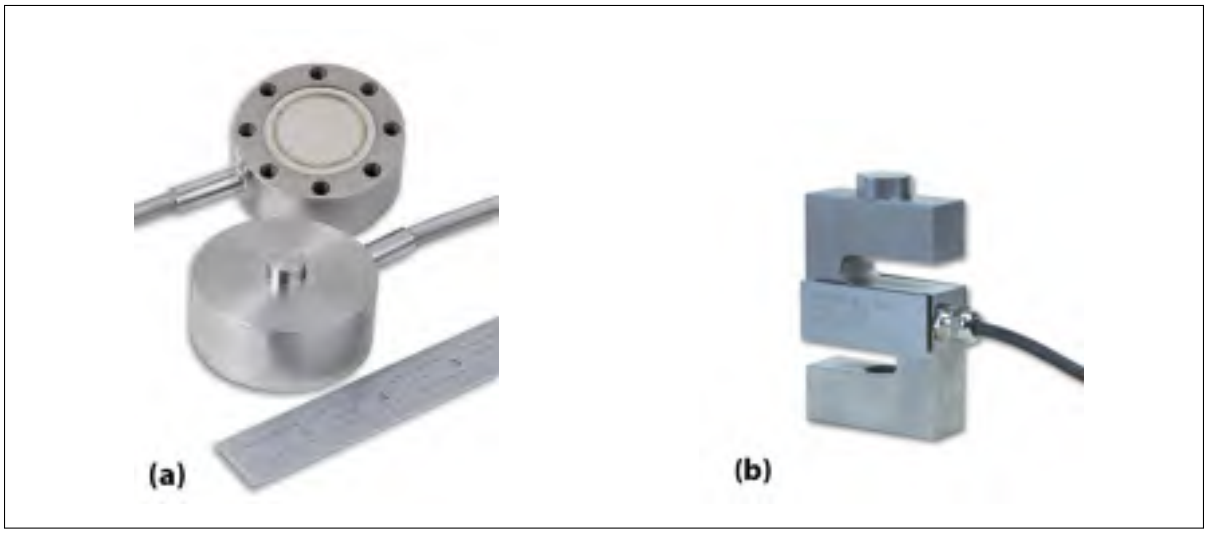

Figure 1.1 Two commercially-available uni-axial force sensors: (a) Miniature compression load cells, (b) S-Beam Load Cells. (Source: www.omega.com)

The second type are known as “tactile force sensors," because the force is applied directly on the sensor. Essentially, arrays of pressure sensors or strain gauges allow the entire surface of an area to be monitored (e.g., artificial skin). These sensors can transmit both the distribution of pressure, and the pattern of force or torque, enabling two-point discrimination with human-like ability. The tactile force sensors that have traditionally been used in robotics generally focus on contact-force determination, for grasp control and object recognition. Figure 1.2 depicts an example of a commercially-available tactile force sensor.

Figure 1.2 Discrete capacitance-based tactile sensor (Source: www.pressureprofile.com)

The third type are referred to as “Multi-axis force-torque sensors", and they measure the forces that oppose the movement of the robot at a single point. Multi-axis force-torque sensors are also known as multi-axis force-torque transducers, six-axis load cells, and multi-axis load cells. They can usually measure forces and torques in multiple directions (up to six axes). The industrial versions represent the vast majority of multi-axis force-torque sensors that are currently being developed. Of these, ATI sensors are the best-known examples (see Figure 1.3). These sensors are generally powerful, as they must be for industrial applications, and they are capable of measuring forces of thousands of Newtons.

This thesis will focus on the third type of sensors; henceforth the general term of multi-axis force-torque sensor will be used when describing this category.

Multi-axis force-torque sensors were noted several decades ago (Whitney, 1985) for their potential to help robots during interactions with new environments. Today, the sensors are used in various applications: surgical, rehabilitation-related, and industrial. The examples discussed below underline the important role of multi-axis force-torque sensors, especially to the next generations of robots. Besides serving the applications discussed in this chapter, the use of such sensors is likely to have a significant impact on the overall field of robotics.

Figure 1.3 The Mini40 6-axis force-torque sensor (Source: www.ati-ia.com)

1.1.1 Surgical applications

Robots are used in many areas of surgery, including neurology, cardiology, orthopaedics, and microsurgery. The presence of robots in surgical procedures has brought many improvements in accuracy and safety, as well as the ability to perform surgical procedures with minimum invasiveness. The role of multi-axis force-torque sensors is to provide feedback so that the surgeon receives as much useful information as possible. For instance, during surgery the sensors allow the surgeon to evaluate the performance of the robot, and to determine the realistic status of the procedure.

The robot SCALPP, shown in Figure 1.4(a), is used for grafting skin for reconstructive surgery. This robot was developed by the laboratory of Robotics and Microelectronics at the Université de Montpellier (France), in collaboration with the burn unit of Montpellier's Lapeyronie Hospital. A six-axis force sensor is placed between the end-effector and the grafting device. The robot commands are adapted according to the data from the sensor, making it possible to regulate the force that is exerted while harvesting the skin. In this case, the sensor must be highly accurate; the robot, in coordination with the surgeon, must procure skin that is just a few tenths of a millimeter in thickness (see Figure 1.4(b)).

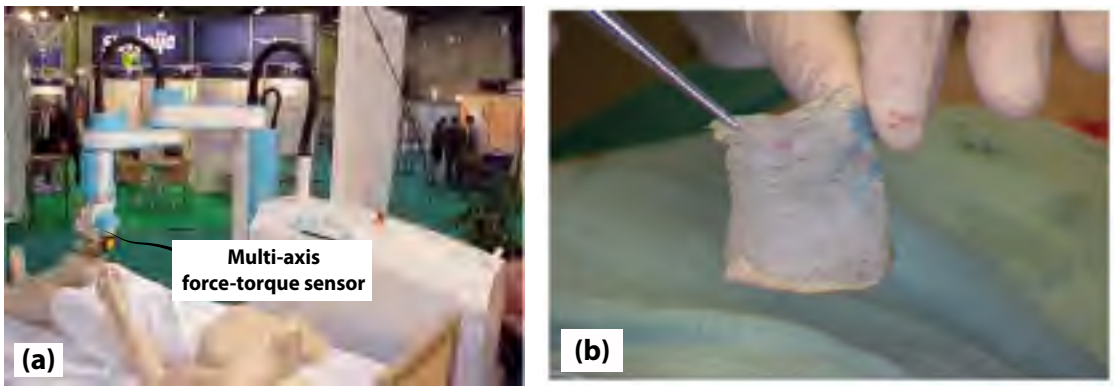

Figure 1.4 SCALPP robot (a) general view; (b) harvesting a skin graft. (Source: www.lirmm.fr)

1.1.2 Physical rehabilitation

In the area of physical rehabilitation, robots are most often used by therapists for training and strengthening the patient's muscles. For this type of application, the robotic system needs to monitor the amount of physical force that is applied by either the user, or by the robot itself. Multi-axis force-torque sensors address this need. For instance, the InMotion hand robot (see Figure 1.5) senses the forces exerted by the patient, and assists the patient as needed, automatically adapting to changed in the patient's abilities. As can be seen from Figure 1.5, the multi-axis force-torque sensor is mounted between the tip of the robotic arm and the end-effector. Sensors developed for this purpose must be particularly robust, as this type of treatment requires the patient to apply forces and torques continuously.

1.1.3 Industrial applications

For industrial robotic applications, researchers have developed a series of special multi-axis force-torque sensors. These are designed to monitor and control the forces that arise during contact between the robot's limbs and the tools it uses (such as a welding tool) when carrying out an automated task. The sensors are typically placed in the robot's wrist, where they monitor

Figure 1.5 InMotion robot, designed for human hand rehabilitation

the manipulation of the tool. This means that the sensors must be reasonably compact, well sized, and mechanically resistant to overload.

One example of how sensors are used in industrial applications is the robotic deburring machine, developed by Norberto Pires *et al.* (2002). As seen in Figure 1.6, a JR3 multi-axis force-torque sensor, which serves as a force control mechanism, is mounted on an industrial robot (ABB IRB 6400). This example shows how these sensors have proven to be a viable solution for industrial use.

1.2 Background

1.2.1 Principle of operation

The design of multi-axis force-torque sensors is a time-consuming process, as it requires the precise application of mechanical and electrical knowledge to the selection of the proper compliant structure and transduction technique. Most of the multi-axis force-torque sensors that have been discussed in the literature (Diddens *et al.*, 1995; Chapuis *et al.*, 2004; Beyeler *et al.*, 2009a; Ranganath *et al.*, 2004b) make use of the same basic operating principle: the multi-axis force-torque sensor uses its compliant body to perceive an applied wrench vector. The spring element in these sensors usually consists of a membrane or crossed-beam structure. The deflec-

Figure 1.6 Force-torque sensors are used in this industrial robotic deburring system
Taken from Norberto Pires *et al.* (2002)

tion caused by the applied wrench induces measurable displacements at preselected locations on the core of the sensor, typically a strain. The displacement is then converted into an electrical signal, such as a voltage variation, using strain gauges and a Wheatstone bridge (Eslami, 2005).

1.2.2 Existing design techniques

The development of multi-axis force-torque sensors is rooted in the design of the engine industry's test instruments. In the 1950s, new devices were needed to test the performance of rocket engines and other emerging developments. Initially, testing-engineers faced problems in collecting the performance information from their tests, as it required the measuring of force

vector with variable magnitude and direction. Doebelin (1985) has reviewed some of the interesting sensors that were designed in this period.

The 1970s saw the emergence of robots in widespread industrial applications. Multi-axis force-torque sensors were connected to a robot end-effector to allow a user to safely interact with unstructured environments. This has extended the range of applications to surgery, rehabilitation, virtual reality, telepresence, and industrial automation, spurring innovations in multi-axis force-torque sensors, as well as a growth in the publications dealing with their design.

The design of multi-axis force-torque sensors can be categorized by the type of the compliant structure, the optimization method and the transduction technique. Here we will review the main developments that have been made in sensor design, by considering each of these factors in turn.

Table 1.1 gives an overview of various approaches to the design multi-axis force-torque sensors, along with their advantages and disadvantages. Since most of these methods are only applied in research settings, we have not gone into detail about the specific characteristics of the sensors. Moreover, there is a great deal of variation between different sensor designs, even when they are based on the same technology, so it made more sense to simply outline the methods instead.

1.2.2.1 Compliant structures

Many of these compliant structures were proposed in the 1990s, such as the kind we called *old generation*, which are based on monolithic elastic structures with strain gauges (Scheinman, 1969). For example, Figure 1.7 depicts one of the oldest elastic structures that was developed for a six-component force-torque sensor; the structure is based on a Maltese cross bar (Chao and Chen, 1997). Made of steel, two opposite rectangular beams were connected to the fixed outer frame. Strain gauges measured the strains at the roots of the four beams.

Table 1.1 Design techniques of force-torque sensors and their relative advantages and disadvantages

Design methodology	Example	Architecture	Optimized characteristic	Axes	Measurement technology	Advantages	Disadvantages
Heuristic	Scheinman (1969)	Maltese cross bar	–	6	Strain gauges	Suited to relatively simple designs	Relies on designer's intuition, so high potential for mistakes Poor reliability
	Nakamura *et al.* (1988)	–	–	6	Strain gauges		
	Liang *et al.* (2010)	Double annulus diaphragm	Interference errors	6	Strain gauges		
FEM analysis	Ricciardi and Borsati (1993)	Laser-welded structure	Cost	6	Strain gauges	3D model Ability to localize high-stress points	Higher computational cost Randomized designs
	Liu *et al.* (2004)	Parallel mechanism	Sensitivity	6	Strain gauges		
	Xin (2009)	Monolothic structure	Cross sensitivities	6	Strain gauges		
FEM analysis combined with optimization	Liu and Tzo (2002)	T-shaped bars	Measurement isotropy	6	Strain gauges	Ability to study a large set of designs	Lengthy solution time Iterative
Kinetostatic analysis	Sorli and Pastorelli (1995)	Stewart platform	Isotropy	6	Resistive	Symbolical model Ability to control spatial resolution via combinations of geometric parameters	Topological analysis only Rough model
	Jia *et al.* (2010)	Stewart platform	Isotropy and sensitivity	6	Piezoelectric		
	Dwarakanath *et al.* (2001)	Stewart platform	Structural isotropy	6	Strain gauges		
	Zhenlin *et al.* (2003)	Stewart platform	Stiffness isotropy	6	Strain gauges		
	Ranganath *et al.* (2004b)	Stewart platform	Sensitivity	6	Strain gauges		
Strain analysis using elasticity theory–stiffness modeling	Weiyi *et al.* (1993)	Mechanically decoupled structure	Cross-sensitivity	6	Strain gauges	Symbolic model enables a better selection of design parameters Speed optimization	Model errors due to creep and shrinkage stresses
	Yu *et al.* (2006)	Strain-deformation expansion mechanism	Stiffness and sensitivity	3	–		
Pseudo-rigid-body-model	Liang *et al.* (2013)	Spatial parallel compliant mechanism	Sensitivity and isotropy	6	Strain gauges	Adapted for elastic members that undergo large deflections	Requires knowledge of kinematic transformations Relative difficulty of analyzing and designing compliant mechanisms
	Chen *et al.* (2013)	Structure with flexural beams	Resolution and range	1	Optical		
Dynamic analysis	Chen and Li (1997)	–	Impact-response	–	–	Takes into account the effects of dynamic behavior	Complex analysis and design procedures
	Chao and Chen (1997)	Maltese cross bar	Weight and natural frequency	6	Strain gauges		
Systematic design procedure	Uchiama *et al.* (1991)	Maltese cross bar	Isotropy	6	Strain gauges	Reduces need for trial-error to find a feasible design solution	Requires a deep understanding of the system
	Bicchi (1992)	Cylindrical beam structure	Accuracy	2-6	Strain gauges		

Dashes indicate that this topic was not specified in the example paper.

The major advantage of this design is its compactness, which reduces the hysteresis and nonlinearity that are associated with bolted construction. However, this structure is highly coupled, which means that the strain caused by certain force-moment components is relatively high. Thus, it does not exhibit uniform sensitivity to the different axes. To resolve this inconsistency, more strain gauges must be added to the structure, which inevitably introduces more complexity to the sensor's construction.

Other researchers have proposed similar methods of structuring the elastic part of the sensor (Chen and Li, 1997; Uchiama *et al.*, 1991). In addition, there has been a structure based on T-bars (Liu and Tzo, 2002). This structure (see Figure 1.8) has been optimized using a Finite Element Method (FEM). The key to this design is the truss behavior, which minimizes the coupling and rigidity of the Maltese cross bar. This is achieved by placing four of the eight beams vertically, rather than horizontally. In 1992, Bicchi (1992) evaluated a simple cylindrical structure whose behavior is almost linear. This structure has the advantage of using the least strain gauges, but the global deflections are minimized, making the structure much more rigid than the Maltese cross-based one.

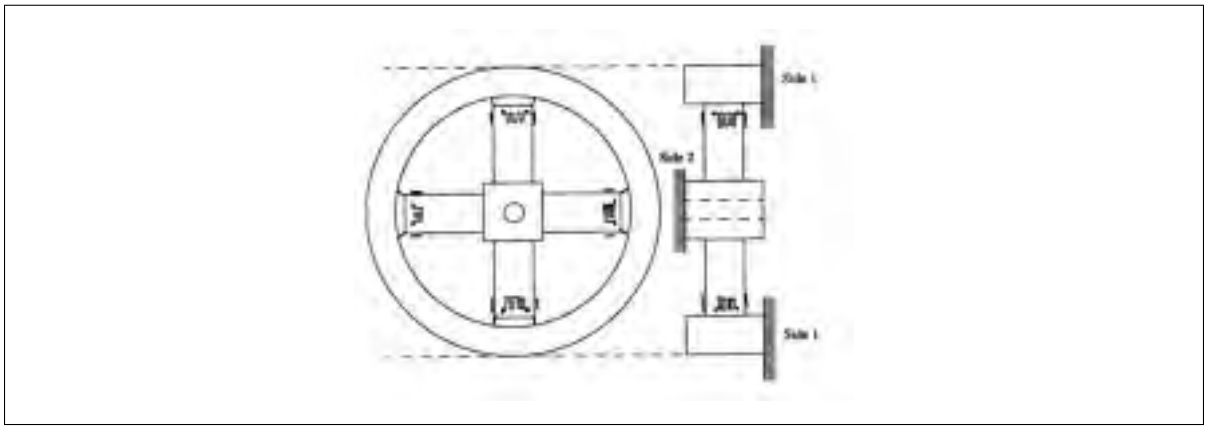

Figure 1.7 Compliant structure based on the Maltese cross bar
Taken from Chao and Chen (1997)

In order to minimize the cross-sensitivities, some researchers rethought the manufacturing method by building a compliant structure with different parts. Ricciardi and Borsati (1993)

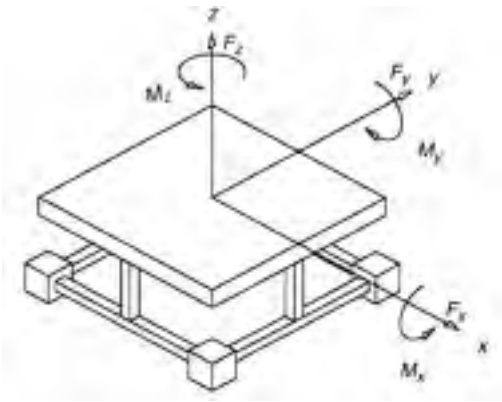

Figure 1.8 Compliant structure based on T-bars
Taken from Liu and Tzo (2002)

used a laser-welded structure to design the flexible element of six-axis force sensor (see Figure 1.9). However, the welding must be extremely secure so as not to cause non-linearities of movement between the welded pieces, as this could provoke variations in sensitivity.

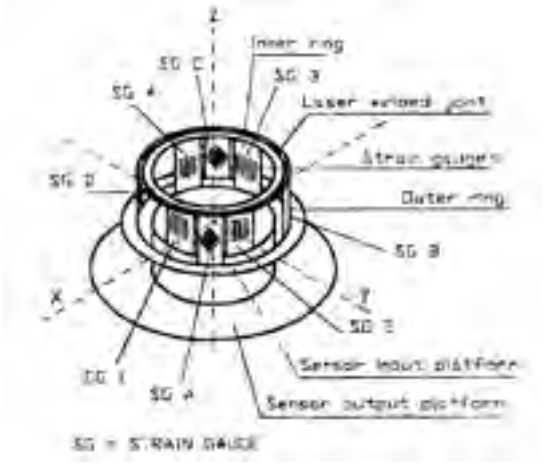

Figure 1.9 Laser-welded compliant structure
Taken from Ricciardi and Borsati (1993)

Recently, Weiyi *et al.* (1993) proposed a novel idea: to build the compliant structure without coupling was proposed. The authors are among the first to highlight the disadvantages of

monolithic structures. Alternatively, they propose the use of a mechanically decoupled compliant structure, which has relatively little coupling and cross-sensitivity (see Figure 1.10).

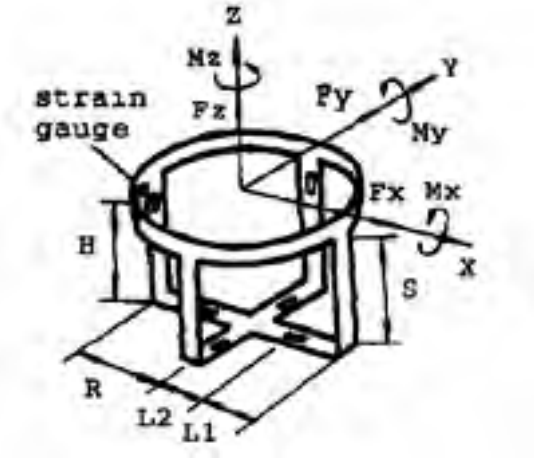

Figure 1.10 Mechanically decoupled structure for a six-degree-of-freedom wrist force sensor
Taken from Weiyi *et al.* (1993)

Another technology, developed in recent years, uses parallel mechanisms to build the compliant structure. Dwarakanath *et al.* (2001) have developed a sensor based on such a parallel mechanism (see Figure 1.11). Their sensor offers good rigidity, and since it can be modeled symbolically, designers are afforded a good knowledge of the coupling. Other researchers, including Kang (2001), developed a multi-axis force-torque sensor based on a Stewart platform (Merlet, 1997). However, these parallel mechanisms have a major limitation, in that the non-monolithic aspect of the structure results in hysteresis, due to the friction generated by the rigid joints that are used to connect the various components of the structure (i.e., the base, the platform and the legs).

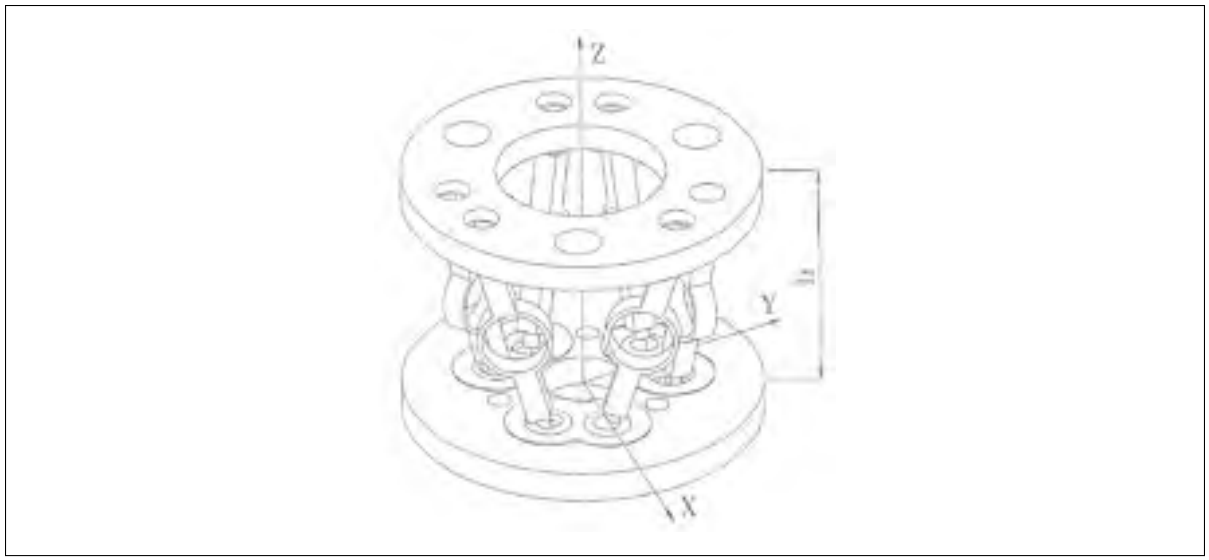

Figure 1.11 Compliant structure based on Stewart platform
Taken from Dwarakanath *et al.* (2001)

1.2.2.2 Optimization methods

With the development of robots aiming towards compactness and high accuracy, it has become even more important to address the problems of force measurement. Multi-axis force-torque sensors not only require high sensitivity in various axial directions with minimal cross-coupling, but they also need to be properly sized to meet the needs of robotic applications. For example, Kim (2004) designed a small 6-axis force sensor to fit the fingers of robot's gripper. This sensor size is 35 mm $\times$ 35 mm $\times$ 85 mm and has a maximum capacity of 20 N for the forces and 1 Nm for the moments. In comparison, the MC3232 six-axis force-torque sensor developed by AMTI for testing of aircraft landing gear equipment has a contact area of 812 mm $\times$ 812 mm–and a capacity of 222 kN for forces and 67.7 kNm for the moments. Recent years have seen several numerical analyses of the mechanical behavior of the elastic element, but many areas, including structure simplification, dynamic behavior and cost, have yet to be as thoroughly discussed.

Published studies in this area tend to focus on the role of structural optimization in improving sensor performance. For instance, Weiyi *et al.* (1993) used the predicted bending strains

obtained from elastic theory, in order to reduce the cross-sensitivity of a six-component force-moment sensor. Also, Liu *et al.* (2004) analyzed an elastic frame structure using the finite element method to find the points where highest strain occurs, which improve the sensor's sensitivity. With on a combination of the FEM and an optimization procedure, Liu and Tzo (2002) created a new structure, based on T-bars, for six-axis force sensors. In 2004, Ranganath *et al.* (2004b) proposed a design based on a kinetostatic analysis of the Stewart-platform, and obtained better sensitivity with a near-singular configuration. Bicchi (1992) took up the challenge of developing a systematic design procedure, and reasserted the importance of linear algebra to provide an appropriate mathematical formulation of the optimal criterion.

1.2.2.3 Transduction techniques

Most multi-axis force-torque sensors use strain gauges as a technological means of inferring the applied wrench (Perry, 1997). As pointed out by Hirose and Yoneda (1990), this displacement-measurement method is responsible for the lower precision and noise sensitivity of commercially available multi-axis force-torque sensors. To circumvent these problems, researchers have proposed alternative measurement techniques, such as optical (Peirs *et al.*, 2004; Takahashi *et al.*, 2003), capacitive (Beyeler *et al.*, 2009b), acoustic (Grahn and Astle, 1984), or inductive (Peshkin, 2007).

Each principle has advantages as well as disadvantages. For instance, the piezoresistive strain gauges can be made using a simple metal wire; but to be used as sensing elements they must be glued to the compliant structure, which implies a loss of sensitivity. We know that optical sensors have great sensitivity, but they are also bulky and require a complex manufacturing process. Inductive sensing elements are generally based on the principle of mutual inductance. They have a high sensitivity, as well as a linear response, but they too necessitate a difficult manufacturing process with numerous steps involved. The acoustic principle can be used instead to make low-cost sensing elements, but it is difficult to decompose the applied force vector.

The capacitive principle has the advantage of a large sensitivity for a wide range of forces, also low sensitivity to temperature, as well as the possibility to perform measurements in 3D. The capacity measurement is well documented in the scientific literature and many circuits, commercial or not can be used. Consequently, capacitive technology was chosen for the realization of the sensing elements presented in this study. This choice was motivated by several criteria. First, the simplicity of the operating principle (variation in capacitance depends on the pressure applied to a deformable structure). Another advantage is that it is possible to decompose the applied force vector and perform simple tests to validate the principle. This technology also has the advantage of requiring fewer steps for fabrication in comparison with other technologies (e.g., optical technology).

1.3 Problem Statement

The solutions proposed in Section 1.2 contribute to a body of multi-axis force-torque sensor designs, but this list is much in need of expansion. These works help to address the question of which method or technology is preferable for a certain application. However, when it comes to the three main aspects of multi-axis force-torque sensor design–the mechanical behavior of the compliant structure, the geometrical optimization, and the transduction technology–most of what they accomplish is focused on just one of these aspects, with little consideration for the others. Furthermore, from a mechanical point of view, their design principles are quite similar. Although each of the multi-axis force-torque sensor design methods has its own advantages, all suffer from at least one of the following drawbacks: *i)* The design and optimization approach has a high computational burden when the finite element method is employed; *ii)* Some important specifications of the application are not taken into account (size, force ranges, stiffness, etc.); *iii)* Due to complex fabrication methods, most of the approaches are relatively expensive to implement.

Researchers have generally focused on the mechanical aspect of the force sensor, as the characteristics of beam designs and deflection are well known. This has led to the development of many types of compliant structures that are based on elastic beam theory. However, the vast

majority of existing compliant structures are simplistic and their design is often based on trial and error. In addition, the designs do not take into account the specifications of the intended application (e.g., the force and torque ranges, material, size, etc.), nor of the appropriate measurement technique (e.g., the displacement ranges). Consequently, the sensors will suffer from structural errors, and will have numerous constraints, such as limited force detection ranges, low sensitivity, coupling and bulkiness.

From a geometrical point of view, beam-based configurations involve relatively complex geometries. These are needed to produce significant displacement or strain in multiple locations (at the compliant structure to be detected by the sensing elements), and to minimize the potential for damage from overloading. However, the optimization methods that are used with these complex geometries are unable to explicitly relate the performance criteria to the sensor geometry and its dimensional parameters. This is due to the lack of information about the kinematics of the compliant structure, as well as the lack of appropriate performance indices, both of which result in structural and geometrical errors and thus prevent optimization. In addition, the customary use of strain gauge transducers is also problematic, because of the potential for interference from the electrically-active robotic environment.

The existing methods of designing multi-axis force sensors are unable to meet the requirements of their applications (as cited in Section 1.1). The sensors produced using these methods are expensive (between $5000 and $15000), difficult to calibrate, sensitive to electromagnetic noise, and frequently subject to the drift of their signals. Additionally, the sensors face conflicting demands in terms of sensitivity and measurement range. Although these disadvantages are physically linked to any sensor, and thus may prove inherent to their design, performance can nonetheless be improved through optimizing the mechanical behavior, geometrical shape and transduction technique.

To address these problems, we must rethink the compliant structure. We aim to improve the sensor's mechanical performance through a deep understanding of the relationship between an applied wrench and the resulting small displacements of the compliant parts of the sensor. In

doing so, we will need to consider the parameters that characterize the sensor design, such as the dimensions, material proprieties, machining processes, and transduction techniques. Our objective is to develop a structure that is easy to analyze, simple to manufacture, and has low coupling effects on the forces and moments.

In addition, we will introduce a new performance index that has not been undertaken in the literature. This will make the optimization procedure more effective, and less heuristic.

Finally, we will use the capacitive sensing principle as the basis of our new sensing element. This means that the capacitive measurements must be calibrated and decoupled in order to provide accurate measurement of forces and torques using the multi-axial sensing element. The stress imaging techniques used by the latter will allow us to increase the sensitivity and the compactness of the sensor.

1.4 Thesis outline

Our research will be presented in three parts. First, we develop a new performance index to synthesize the geometrical architecture of the force-torque sensor. Second, we propose an advanced method to design the mechanical structure of force-torque sensors. Third, we present the realization of a new capacitive readout system for these types of sensors.

The first part of this thesis–the synthesis of the compliant architecture at the sensor's core–is inspired by previous approaches, but here we add a new twist. Several researchers have already devised performance indices from mechanism theory, but our approach includes the innovation of using the changes in the compliant mechanism's geometry as a new performance index. With the application of external forces, the compliant mechanism deviates from its unloaded configuration, and thus, changes in geometry prevent the sensor from exhibiting a linear response. In order to minimize this nonlinear behavior, the potential sources of error are analyzed by applying linear algebra techniques to the expression of the Cartesian force mapping. Two performance indices are then presented and combined. The first index measures the variations of the Jacobian matrix about the unloaded configuration. The second index measures the ampli-

fication of the error arising from the measurement of the joint displacements. The resulting indices can be expressed symbolically, making them easier to evaluate and synthesize. At the conclusion to this first section, we give an example, showing how the performance indices that we have developed may be applied to a simple compliant mechanism.

The second part of our research presents an advanced method to design the compliant structure of force-torque sensors at the design stage. Whereas some researchers have used finite element analysis on the whole compliant structure (or just some of its components), and others have proposed methods based on stress analysis, we take a new approach to this problem. Our work relies on a symbolic formulation of the wrench-displacement relationship, by which we minimize the condition number of the linear input-output relationship. This method is centred on the application requirements, and thus it takes the necessary constraints into account, such as the measurement range, the maximum allowed compliance, and the maximum physical dimensions of the structure. The input-output relationship allows to match the applied forces with the sensor displacements, in order to achieve the desired sensitivity level. The resulting performance index can be expressed symbolically, facilitating the synthesis task. Finally, we illustrate our theory by showing the optimization procedure, design, fabrication and experiments that we conducted with a three-axis force sensor architecture.

The third segment presents a new approach to the design of multi-axial force sensing elements. We show that it is possible to measure multiple forces by detecting each of the stress components–namely normal stress, shear stress, and torque–, separately, with a single sensing element. Multi-axis force-torque sensors have become popular in the field of robotics because they provide valuable information to robots during physical interaction; but these sensors have posed a challenge to researchers during fabrication, as they typically require multiple uni-axial sensing elements scattered over the mechanical structure of the force-torque sensor. We solve this problem by accomplishing the same functionality with just one sensing element. Our sensing element is composed of layers of elastomer, with conductive electrodes integrated within the two sensitive layers. When a force is applied, some (or all) of the electrodes within each layer are compressed, changing the capacitance and providing stress images. Stress-imaging

analysis thus allows us to reliably infer the applied force. In this chapter we describe the design, fabrication, and characterization of our triaxial sensing element. After constructing the prototype, we validate its performance using a series of experiments. The results demonstrate that our stress-imaging analysis method does indeed allow the measurement of multiple force components with a single sensing element.

CHAPTER 2

GEOMETRICAL ANALYSIS OF THE MULTI-AXIS FORCE-TORQUE SENSOR DESIGN

2.1 Introduction

The literature has emphasized the importance of using parallel mechanical systems to build the compliant mechanisms at the core of multi-axis force-torque sensors. The design of these compliant mechanisms was largely inspired by the kinematic design of six degree-of-freedom parallel robotic manipulators. Indeed, several authors (Uchiyama and Svinin, 1995; Dwarakanath *et al.*, 2001; Ranganath *et al.*, 2004b) have designed a variety of multi-axis force-torque sensors based on Stewart platforms (Merlet, 1997). When designing a multi-axis force-torque sensor, perhaps the most crucial step is finding the optimum dimensions of the compliant mechanism in order to measure a desired force range with high precision. To this end, a number of performance-evaluation criteria have already been introduced. Uchiyama and Hakomori (1985); Uchiyama *et al.* (1988) have proposed a systematic design procedure for minimizing the condition number of the compliance matrix of the multi-axis force-torque sensor. Bicchi (1992) has generalized the condition number of the compliance matrix and proposed that this number be the performance index for the design of the sensor's mechanical architecture. Uchiyama and Svinin (1995) have proposed an index for evaluating the isotropy of the multi-axis force-torque sensor as the main indicator of its performance. Ranganath *et al.* (2004a) have dealt with the analysis and design of a Stewart-platform-based multi-axis force-torque sensor in a near-singular configuration. Also, we presented in Chapter 1, a comprehensive list of performance criteria and design approaches.

However, only a few of these performance criteria have considered the changes in geometry to which the compliant mechanism is subjected as it undergoes deformations, and only one study has attempted to evaluate the linearity of the sensor's response to an external wrench. This one study is by Hirose and Yoneda (1990), who have pointed out the problem of nonlinear displacements. These authors propose a method by which one can identify the nonlinear characteristics

due to the forces and moments applied on an arbitrary compliant structure. The solution taken in this study to reduce the effect of nonlinear displacements is based on a nonlinear calibration technique. However, the calibration step intervenes at a very late stage of the design procedure, which may require further signal processing and recurrent adjustments.

In this chapter we propose a method to minimize these structural errors at an early stage of the multi-axis force-torque sensor design. This requires that we minimize the errors caused by changes in geometry. This objective sometimes conflicts with the minimization of the errors resulting from the amplification of the joint displacements measurement-noise, by making the sensor near-isotropic. The changes in geometry are further exacerbated by the necessity of using inexpensive displacement sensors so as to keep the overall cost of the sensor low, with the result that the joint displacements must be larger in order to be detected. If we fail to consider the geometry changes that occur as the compliant mechanism is deformed, our final design of multi-axis force-torque sensor will contain large structural errors. Therefore, to avoid excessive nonlinear calibrations and re-calibrations of the sensor, we must minimize the nonlinear displacements caused by forces and moments applied in different directions from the start of the design process. The current study proposes that we take two factors into account when optimizing the sensor's design: changes in geometry, and the amplification of the errors resulting from the displacement sensors at the measured joints. To this end, we present two indices of the changes in geometry and one index of the measurement error amplification. We then illustrate the proposed approach with some examples of simple mechanisms, and validate the functionality of our method.

The chapter is organized as follows. In Section 2.2, we begin by deriving a mathematical expression of the relationship between the generalized applied forces and the corresponding joint displacements. We then propose two new indices and revisit the condition number. Section 2.3 describes our approach to multi-objective optimization, which uses multiple indices of performance. We apply this approach to a simple serial-two-link planar mechanism in Section 2.4. We also apply our methodology to a parallel 2-PRR mechanism, and present the ensuing discussion in Section 2.5, before drawing to a close in Section 2.6.

2.2 Error analysis

The vast majority of current multi-axis force-torque sensors operate under the same principle: essentially, an applied force is transformed into a measurable displacement. Our example uses a compliant mechanism loaded by an external wrench, **w**, that generates displacements at preselected joints. These displacements are then detected by means of any of the following options: strain gauges, optical sensors (Hirose and Yoneda, 1990), inductive displacement sensors (Piller, 1982; Kang, 2001), or CCD elements (Kvasnica, 1992).

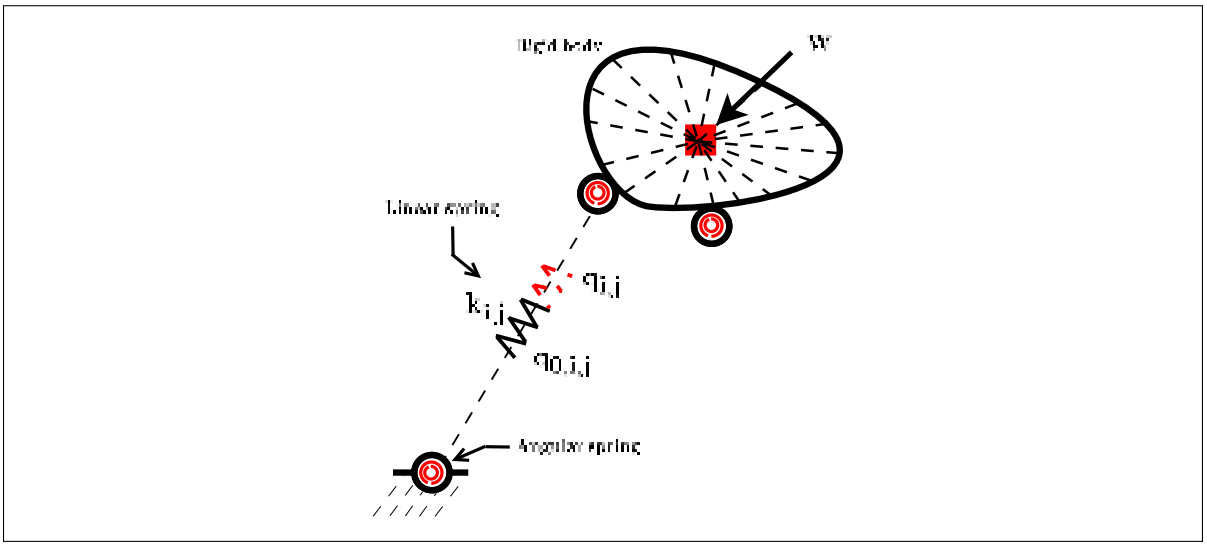

Figure 2.1 Generic rigid-link mechanism with lumped elastic springs at its joints

We model the compliant mechanism of the multi-axis force-torque sensor as a rigid-link parallel mechanism, with lumped elastic springs at its joints. The rigid-link mechanism must have n degrees of freedom, where n is the number of generalized forces it is to measure, i.e., force and torque components. Let us also assume that the mechanism is fully parallel, so that all its m legs are serial kinematic chains, and that each of these legs has exactly n joints allowing for n degrees of freedom. We assume the displacement of the j^{th} spring from the i^{th} leg to be $q_{i,j}$, whether it is angular or linear. Its corresponding elastic spring is assumed to have a proportionality constant $k_{i,j}$ and a free length $q_{0,i,j}$. In order to estimate the n-dimensional wrench

$\mathbf{w}$, only n of the $m \times n$ compliant joints are equipped with displacement sensors. We make no assumptions regarding the location of these sensors with respect to the other joints.

From these definitions, we form the array of the joint displacements of the i^{th} leg, $\mathbf{q}_i \equiv [q_{i,1} \ \cdots \ q_{i,n}]^T$, and, for the complete mechanism, we form $\mathbf{q} \equiv [\mathbf{q}_1^T \ \cdots \ \mathbf{q}_m^T]^T$. The corresponding arrays of the spring constants are $\mathbf{k} \equiv [k_{1,1} \ \cdots \ k_{m,n}]^T$, and the arrays of the free lengths are $\mathbf{q}_0 \equiv [q_{0,1,1} \ \cdots \ q_{0,m,n}]^T$.

Upon defining the matrix $\mathbf{K}_q \equiv \text{diag}(\mathbf{k})$, the potential energy stored in the compliant mechanism may be expressed as

$$V = (1/2)(\mathbf{q} - \mathbf{q}_0)^T \mathbf{K}_q (\mathbf{q} - \mathbf{q}_0). \tag{2.1}$$

Let the array $\mathbf{p}$ representing a small displacement of the suspended mass (the rigid body) be compatible with the measured wrench $\mathbf{w}$, so that we may express the work performed by $\mathbf{w}$ as $\mathbf{p}^T \mathbf{w}$. We now have

$$\begin{aligned}
\mathbf{w} &= \frac{\partial V}{\partial \mathbf{p}} \\
&= \left(\frac{\partial \mathbf{q}}{\partial \mathbf{p}} \right)^T \frac{\partial V}{\partial \mathbf{q}}, \\
&= \left[(\partial \mathbf{q}_1 / \partial \mathbf{p})^T \quad \cdots \quad (\partial \mathbf{q}_m / \partial \mathbf{p})^T \right] \mathbf{K}_q (\mathbf{q} - \mathbf{q}_0), \\
&= \mathbf{H} \mathbf{K}_q (\mathbf{q} - \mathbf{q}_0),
\end{aligned} \tag{2.2}$$

where $\mathbf{H} \equiv [\mathbf{J}_1^{-T} \ \cdots \ \mathbf{J}_m^{-T}]$, and $\mathbf{J}_i \equiv \partial \mathbf{p} / \partial \mathbf{q}_i$ is the Jacobian matrix of the serial chain formed by the i^{th} leg.

This last equation was originally obtained by Salisbury (1980) for a single serial chain, in order to simulate six degree-of-freedom stiffness in a virtual environment. It is placed here to account for fully-parallel mechanisms, and to clarify its link with the application of multi-axis force-torque sensors. Note that Equation (2.2) represents a nonlinear relationship between $\mathbf{w}$ and $\mathbf{q}$, as we consider $\mathbf{H}$ to be a function of $\mathbf{q}$ (symbolically, $\mathbf{H} = \mathbf{H}(\mathbf{q})$). Under these conditions,

Equation (2.2) is the *exact* mathematical description of the force-displacement relationship for the lumped-compliance rigid-link mechanism described above.

As a typical multi-axis force-torque sensor does not have the same measurement ranges and accuracies in all sensitive directions, it becomes difficult to determine the relative importance of these sensitive directions. More academically, this is the classic problem of the dimensionally non-homogeneous Jacobian matrix, which prevents the addition of its entries. We propose to resolve this problem by a method akin to that of Yoshikawa (1985), whereby we normalize the wrench and joint coordinates. The ranges of applied forces and torques that the sensor should be capable of measuring are defined as

$$\mathbf{w}_{\min} \leq \mathbf{w} \leq \mathbf{w}_{\max}, \tag{2.3}$$

where the inequality $\leq$ is taken component-wise. In parallel, we define the ranges of joint displacements as

$$\mathbf{q}_{\min} \leq \mathbf{q} \leq \mathbf{q}_{\max}. \tag{2.4}$$

In practice, these bounds may come from the maximum deformations allowed at the compliant joints, or by the measurement ranges of displacement sensors at these joints. The parameters $\mathbf{w}_{\min}$, $\mathbf{w}_{\max}$, $\mathbf{q}_{\min}$ and $\mathbf{q}_{\max}$ will be known in advance by the designer, so the subsequent normalization should pose no problem.

We obtain the normalized generalized forces $\overline{\mathbf{w}}$ by dividing the applied forces by their corresponding ranges, which yields

$$\overline{\mathbf{w}} \equiv \operatorname{diag}(\mathbf{w}_{\max} - \mathbf{w}_{\min})^{-1}(\mathbf{w} - \mathbf{w}_{\min}). \tag{2.5}$$

Similarly, the normalized joint coordinates $\overline{\mathbf{q}}$ are computed as

$$\overline{\mathbf{q}} \equiv \operatorname{diag}(\mathbf{q}_{\max} - \mathbf{q}_{\min})^{-1}(\mathbf{q} - \mathbf{q}_{\min}), \tag{2.6}$$

and the the normalized free-lengths as

$$\overline{\mathbf{q}}_0 \equiv \text{diag}(\mathbf{q}_{\max} - \mathbf{q}_{\min})^{-1}(\mathbf{q}_0 - \mathbf{q}_{\min}). \tag{2.7}$$

We substitute Equations (2.5), (2.6) and (2.7) into Equation (2.2), which yields the normalized relationship

$$\overline{\mathbf{w}} = \overline{\mathbf{H}}\mathbf{K}_q(\overline{\mathbf{q}} - \overline{\mathbf{q}}_0) + \overline{\mathbf{w}}_0, \tag{2.8}$$

where $\overline{\mathbf{H}} \equiv \text{diag}(\mathbf{w}_{\max} - \mathbf{w}_{\min})^{-1}\mathbf{H}\text{diag}(\mathbf{q}_{\max} - \mathbf{q}_{\min})$ and $\overline{\mathbf{w}}_0 \equiv -\text{diag}(\mathbf{w}_{\max} - \mathbf{w}_{\min})^{-1}\mathbf{w}_{\min}$.

From our initial assumptions, recall that only n of the $m \times n$ joints are equipped with displacement sensors. Symbolically, we thus measure only the variables $\hat{\mathbf{q}} \in \mathbb{R}^n$ out of the variables $\overline{\mathbf{q}} \in \mathbb{R}^{mn}$, and the unmeasured joint displacements are labelled $\check{\mathbf{q}} \in \mathbb{R}^{mn-n}$. The relationship between $\hat{\mathbf{q}}$, $\check{\mathbf{q}}$ and $\overline{\mathbf{q}}$ may therefore be written as

$$\begin{bmatrix} \hat{\mathbf{q}} \\ \check{\mathbf{q}} \end{bmatrix} = \mathbf{P}\overline{\mathbf{q}} = \begin{bmatrix} \hat{\mathbf{P}} \\ \check{\mathbf{P}} \end{bmatrix} \overline{\mathbf{q}}, \tag{2.9}$$

where $\mathbf{P} \in \mathbb{R}^{mn \times mn}$ is a permutation matrix, its submatrices $\hat{\mathbf{P}}$ and $\check{\mathbf{P}}$ possessing n and $mn-n$ rows, respectively. As a permutation matrix is always orthogonal, we may write

$$\overline{\mathbf{q}} = \mathbf{P}^T \begin{bmatrix} \hat{\mathbf{q}} \\ \check{\mathbf{q}} \end{bmatrix} = \hat{\mathbf{P}}^T\hat{\mathbf{q}} + \check{\mathbf{P}}^T\check{\mathbf{q}}. \tag{2.10}$$

From the same reasoning, we obtain $\overline{\mathbf{q}}_0 \equiv \hat{\mathbf{P}}^T\hat{\mathbf{q}}_0 + \check{\mathbf{P}}^T\check{\mathbf{q}}_0$, where $\hat{\mathbf{q}}_0$ and $\check{\mathbf{q}}_0$ are the normalized free-lengths of the springs of the measured and unmeasured joints, respectively. Upon substitution of the latter relationships in Equation (2.8), we obtain

$$\overline{\mathbf{w}} = \overline{\mathbf{H}}\mathbf{K}_q\hat{\mathbf{P}}^T(\hat{\mathbf{q}} - \hat{\mathbf{q}}_0) + \overline{\mathbf{H}}\mathbf{K}_q\check{\mathbf{P}}^T(\check{\mathbf{q}} - \check{\mathbf{q}}_0) + \overline{\mathbf{w}}_0. \tag{2.11}$$

Since the number of degrees of freedom of the mechanism, n, is the same as the number of measured joint displacements, one may infer the complete posture from $\hat{\mathbf{q}}$ alone. Therefore, $\check{\mathbf{q}}$ may be seen as a function of $\hat{\mathbf{q}}$ through the mechanism loop-closure equations, i.e., $\check{\mathbf{q}} = \check{\mathbf{q}}(\hat{\mathbf{q}})$.

Hence, the nonlinear relationship of Equation (2.2) between $\mathbf{w}$ and $\mathbf{q}$ has been transformed to express the relationship between $\overline{\mathbf{w}}$ and $\hat{\mathbf{q}}$. While still representing the generalized applied forces and joint displacements, respectively, these variables are now expressed in units as percentage points of the scales of their corresponding sensors. Even when coming from different sensors, these percentage points are all summed together to compute the indices proposed in the remainder of this chapter. Should the designer require more *relative accuracy* from one sensitive direction than from another, he or she should modify the proposed normalized coordinates, as the current normalization assumes a *uniform relative sensitivity*.

Figure 2.2 provides a visualization of the nonlinear relationship between $\overline{w}_i$, the i^{th} component of $\overline{\mathbf{w}}$, and $\hat{\mathbf{q}}$. In this graph, the multi-axis force-torque sensor input-output relationship $\overline{w}_i(\hat{\mathbf{q}})$ appears as the curved surface on top, and its linear approximation appears below as a plane. In most existing multi-axis force-torque sensors, the small ranges of joint displacements $\mathbf{q}_{\min} \leq \mathbf{q} \leq \mathbf{q}_{\max}$ allow for a linear approximation of the nonlinear relationship of Equation (2.8), as shown in Figure 2.2. However, small ranges of $\mathbf{q}$ require highly sensitive displacement sensors and accurate machining technology, which partly explains the high cost of commercially available multi-axis force-torque sensors.

Multi-axis force-torque sensors of lower cost will generally display less sensitivity, requiring larger joint displacements (i.e., a larger distance between $\mathbf{q}_{\min}$ and $\mathbf{q}_{\max}$) to occur so that they can be detected. The sensors must have a compliant mechanism that can account for the nonlinearity of Equation (2.8). While the level of nonlinearity should be minimized, it is also important that the amplification of the joint measurement-error be as lower as possible.

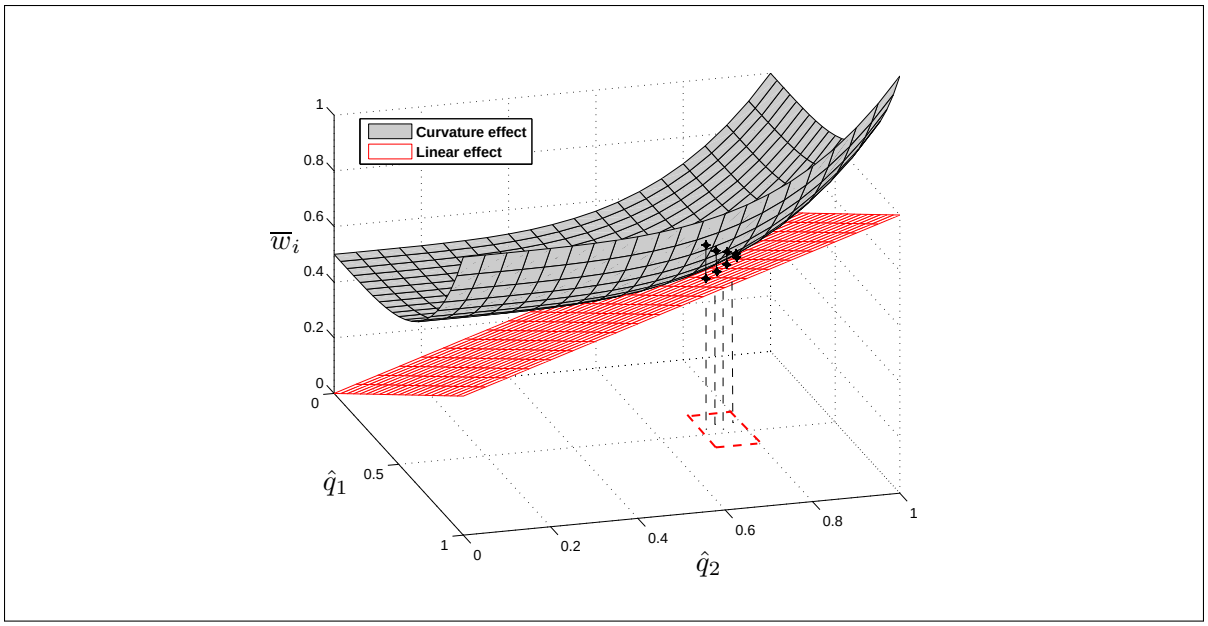

Figure 2.2 The nonlinear relationship between $\overline{w}_i$ and $\hat{\mathbf{q}}$, and its linear approximation

2.2.1 Change in geometry

We propose two indices of the importance of nonlinearity in multi-axis force-torque sensors. The first index takes into account the compliant mechanism behavior over the full range of displacements allowed at its joints. This requires a numerical integration, which is generally computationally intensive. The second index avoids this potential problem by using only local information at the reference posture of the compliant mechanism. Here we describe the global index of the structural error, which we believe is the ideal way to measure the level of nonlinearity.

2.2.1.1 A global index of the structural error

One of the most direct methods of quantifying the level of nonlinearity in Equation (2.8) is through the root-mean-square value of the difference between $\overline{\mathbf{w}}(\hat{\mathbf{q}})$ and its own linear component, over the range $\mathbf{q}_{\min} \leq \mathbf{q} \leq \mathbf{q}_{\max}$ of measurable displacements. This may be expressed

symbolically as

$$\sqrt{\int_0^1 \cdots \int_0^1 \|\overline{\mathbf{w}} - \acute{\mathbf{w}}\|^2 d\hat{q}_1 \cdots d\hat{q}_n}. \tag{2.12}$$

In this expression, the estimated normalized force $\acute{\mathbf{w}}$ is obtained by linearizing $\overline{\mathbf{w}}(\hat{\mathbf{q}})$ about the reference posture $\hat{\mathbf{q}}_0$, which yields

$$\acute{\mathbf{w}} = \overline{\mathbf{H}}_0 \mathbf{K}_q \hat{\mathbf{P}}^T (\hat{\mathbf{q}} - \hat{\mathbf{q}}_0) + \overline{\mathbf{H}}_0 \mathbf{K}_q \check{\mathbf{P}}^T (\check{\mathbf{q}} - \check{\mathbf{q}}_0) + \overline{\mathbf{w}}_0. \tag{2.13}$$

where $\overline{\mathbf{H}}_0 \equiv \overline{\mathbf{H}}(\hat{\mathbf{q}}_0)$. The difference between the two vectors thus becomes

$$\overline{\mathbf{w}} - \acute{\mathbf{w}} = (\overline{\mathbf{H}} - \overline{\mathbf{H}}_0)\mathbf{K}_q \hat{\mathbf{P}}^T (\hat{\mathbf{q}} - \hat{\mathbf{q}}_0) + (\overline{\mathbf{H}} - \overline{\mathbf{H}}_0)\mathbf{K}_q \check{\mathbf{P}}^T (\check{\mathbf{q}} - \check{\mathbf{q}}_0) \tag{2.14}$$

However, note that minimizing the nonlinearity alone generally leads to a mechanism with high sensitivity to applied forces, as the function $\overline{\mathbf{w}}(\hat{\mathbf{q}})$ tends to approach a constant function. This is undesirable, as it will then take only a small force to produce large displacements at the compliant joints.

In order to circumvent this problem, we propose using the ratio of the nonlinearity error to the overall sensitivity of the compliant mechanism, both being measured by a root-mean-square computation, in order to formulate the index. This leads to the index

$$\gamma \equiv \sqrt{\frac{\int_0^1 \cdots \int_0^1 \|\overline{\mathbf{w}} - \acute{\mathbf{w}}\|^2 d\hat{q}_1 \cdots d\hat{q}_n}{\int_0^1 \cdots \int_0^1 \|\overline{\mathbf{w}}\|^2 d\hat{q}_1 \cdots d\hat{q}_n}}. \tag{2.15}$$

We refer to γ as the Global Index of the Structural Error (GISE). In kinematic synthesis, the structural error indicates the deviation in the trajectory of the moving link of a mechanism, i.e., the deviation from the prescribed trajectory which the link was designed to follow. Here, γ measures the deviation of the mechanism from the ideal state, i.e., deviation from the state in which the Jacobian matrix remains constant. This deviation from the ideal state occurs with some mechanisms, especially those with highly non-rigid links. The term "global" here refers

to the whole workspace in which the behavior of the compliant mechanism is being assessed, i.e., the workspace given by $\mathbf{q}_{\min} \leq \mathbf{q} \leq \mathbf{q}_{\max}$. Obviously, one may obtain the most accurate information by considering all the possible mechanism postures. However, this poses a computational problem, especially with six-axis force-torque sensors where one must evaluate a sextuple integral. A better alternative is a local index, as it only requires us to identify the behavior of the compliant mechanism at a single point.

2.2.1.2 A local index of the structural error

An efficient way to circumvent the GISE's computational burden (Equation (2.15)) is to minimize the nonlinearity of Equation (2.11) at the reference posture $\hat{\mathbf{q}}_0$. The ideal mechanical design for this index is the one for which an infinitesimal change of $\hat{\mathbf{q}}$ around the equilibrium configuration will have the least effect on the changes in geometry. The instantaneous relationship between the normalized forces and the joint displacements can be found by differentiating Equation (2.11), which yields

$$d\overline{\mathbf{w}} = d\overline{\mathbf{H}}\mathbf{K}_q(\hat{\mathbf{P}}^T(\hat{\mathbf{q}}-\hat{\mathbf{q}}_0)+\check{\mathbf{P}}^T(\check{\mathbf{q}}-\check{\mathbf{q}}_0))+\overline{\mathbf{H}}\mathbf{K}_q(\hat{\mathbf{P}}^T d\hat{\mathbf{q}}+\check{\mathbf{P}}^T d\check{\mathbf{q}}) \tag{2.16}$$

Using the definition of $d\overline{\mathbf{H}}$, this equation can also be written as

$$d\overline{\mathbf{w}} = \left(\left.\frac{\partial\overline{\mathbf{H}}}{\partial\hat{\mathbf{q}}}\right|_0 \mathbf{K}_q\left(\hat{\mathbf{P}}^T(\hat{\mathbf{q}}-\hat{\mathbf{q}}_0)+\check{\mathbf{P}}^T(\check{\mathbf{q}}-\check{\mathbf{q}}_0)\right) + \overline{\mathbf{H}}_0\mathbf{K}_q\right)(\hat{\mathbf{P}}^T d\hat{\mathbf{q}}+\check{\mathbf{P}}^T d\check{\mathbf{q}}), \tag{2.17}$$

where $(\partial\overline{\mathbf{H}}/\partial\hat{\mathbf{q}})|_0$ is a third-order tensor evaluated at the reference posture $\hat{\mathbf{q}} = \hat{\mathbf{q}}_0$. This expression is somewhat similar to the relation presented by Kao (2000), in their work on the conservative congruence transformation of joint and Cartesian stiffness matrices. As they have proposed, one may expand Equation (2.17) so as to avoid working with a third-order tensor.

This leads us to

$$d\overline{\mathbf{w}} = \Bigg(\left[\left. \frac{\partial \overline{\mathbf{H}}}{\partial \hat{q}_1} \right|_0 \mathbf{K}_q \left(\hat{\mathbf{P}}^T (\hat{\mathbf{q}} - \hat{\mathbf{q}}_0) + \check{\mathbf{P}}^T (\check{\mathbf{q}} - \check{\mathbf{q}}_0) \right) \quad \cdots \right.$$
$$\left. \left. \frac{\partial \overline{\mathbf{H}}}{\partial \hat{q}_n} \right|_0 \mathbf{K}_q \left(\hat{\mathbf{P}}^T (\hat{\mathbf{q}} - \hat{\mathbf{q}}_0) + \check{\mathbf{P}}^T (\check{\mathbf{q}} - \check{\mathbf{q}}_0) \right) \right] + \overline{\mathbf{H}}_0 \mathbf{K}_q \Big) \left(\hat{\mathbf{P}}^T d\hat{\mathbf{q}} + \check{\mathbf{P}}^T d\check{\mathbf{q}} \right). \tag{2.18}$$

To retain just the nonlinear component of $d\overline{\mathbf{w}}$, we compare it against the (linearly) estimated normalized force $\acute{\mathbf{w}}$, as expressed in Equation (2.13). As the Jacobian matrix is a constant in this equation, taking the derivative on both sides simply yields

$$d\acute{\mathbf{w}} = \overline{\mathbf{H}}_0 \mathbf{K}_q (\hat{\mathbf{P}}^T d\hat{\mathbf{q}} + \check{\mathbf{P}}^T d\check{\mathbf{q}}). \tag{2.19}$$

Using this definition, the instantaneous distortion of the geometry due to an applied force can be expressed as

$$d\overline{\mathbf{w}} - d\acute{\mathbf{w}} = \left[\left. \frac{\partial \overline{\mathbf{H}}}{\partial \hat{q}_1} \right|_0 \mathbf{K}_q \left(\hat{\mathbf{P}}^T (\hat{\mathbf{q}} - \hat{\mathbf{q}}_0) + \check{\mathbf{P}}^T (\check{\mathbf{q}} - \check{\mathbf{q}}_0) \right) \quad \cdots \right.$$
$$\left. \left. \frac{\partial \overline{\mathbf{H}}}{\partial \hat{q}_n} \right|_0 \mathbf{K}_q \left(\hat{\mathbf{P}}^T (\hat{\mathbf{q}} - \hat{\mathbf{q}}_0) + \check{\mathbf{P}}^T (\check{\mathbf{q}} - \check{\mathbf{q}}_0) \right) \right] d\overline{\mathbf{q}}. \tag{2.20}$$

where $d\overline{\mathbf{q}} = \hat{\mathbf{P}}^T d\hat{\mathbf{q}} + \check{\mathbf{P}}^T d\check{\mathbf{q}}$ and $d\check{\mathbf{q}} = d\check{\mathbf{q}}(d\hat{\mathbf{q}})$. The magnitude $\|d\overline{\mathbf{w}} - d\acute{\mathbf{w}}\|_2$ of this distortion is to be minimized for all possible values of $\hat{\mathbf{q}}$ and $d\hat{\mathbf{q}}$.

As an alternative to a costly numerical integration of the possible combinations of these parameters, we elect to minimize an upper bound of $\|d\overline{\mathbf{w}} - d\acute{\mathbf{w}}\|_2$. To this end, let us define

$$\overline{\mathbf{F}} \equiv \left[\left. \frac{\partial \overline{\mathbf{H}}}{\partial \hat{q}_1} \right|_0 \mathbf{K}_q \quad \cdots \quad \left. \frac{\partial \overline{\mathbf{H}}}{\partial \hat{q}_n} \right|_0 \mathbf{K}_q \right], \tag{2.21}$$

$$\overline{\mathbf{Q}} \equiv \begin{bmatrix} \overline{\mathbf{q}} - \overline{\mathbf{q}}_0 & \mathbf{0}_n & \cdots & \mathbf{0}_n \\ \mathbf{0}_n & \overline{\mathbf{q}} - \overline{\mathbf{q}}_0 & \cdots & \mathbf{0}_n \\ \vdots & \vdots & \ddots & \vdots \\ \mathbf{0}_n & \mathbf{0}_n & \cdots & \overline{\mathbf{q}} - \overline{\mathbf{q}}_0 \end{bmatrix}, \tag{2.22}$$

thus allowing Equation (2.20) to be rewritten as

$$d\overline{\mathbf{w}} - d\acute{\mathbf{w}} = \overline{\mathbf{F}}\overline{\mathbf{Q}}d\overline{\mathbf{q}}. \tag{2.23a}$$

Thence, the magnitude of the nonlinearity is bounded as

$$\|d\overline{\mathbf{w}} - d\acute{\mathbf{w}}\|_2 = \|\overline{\mathbf{F}}\overline{\mathbf{Q}}d\overline{\mathbf{q}}\|_2, \tag{2.23b}$$

$$\leq \|\overline{\mathbf{F}}\|_2 \|\overline{\mathbf{Q}}d\overline{\mathbf{q}}\|_2, \tag{2.23c}$$

$$\leq \|\overline{\mathbf{F}}\|_F \|\overline{\mathbf{Q}}d\overline{\mathbf{q}}\|_2, \tag{2.23d}$$

where $\|\cdot\|_F$ denotes the Frobenius norm. Notice that the last inequality was obtained from the relationship $\|\overline{\mathbf{F}}\|_2 \leq \|\overline{\mathbf{F}}\|_F$, which is true for any matrix $\overline{\mathbf{F}}$ (see Golub and Van Loan (1996)). In Equation (2.23d), the compliant mechanism design parameters, that were captured in $\|\overline{\mathbf{F}}\|_F$, are decoupled from the displacements which appear in $\|\overline{\mathbf{Q}}d\overline{\mathbf{q}}\|_2$. Therefore, minimizing $\|\overline{\mathbf{F}}\|_F$ reduces the structural error of the mechanism without making any hypothesis on its displacements about the reference posture. We thus propose the following index as a local measure of the structural error:

$$\text{minimize } \lambda^2 \equiv \|\overline{\mathbf{F}}\|_F^2. \tag{2.24}$$

Accordingly, we refer to λ as the Local Index of the Structural Error (LISE) induced by a compliant mechanism. Notice that λ depends on the topology and dimensions of the rigid-link mechanism, as well as on the stiffnesses at its elastic joints and on its unloaded posture $\overline{\mathbf{q}}_0$. All these parameters may be considered as decision variables in problem (2.24).

For the purpose of optimization, it may prove useful to expand the expression of λ as

$$\begin{aligned}
\lambda^2 &= \sum_{j=1}^{n} \left\| \left. \frac{\partial \overline{\mathbf{H}}}{\partial \hat{q}_j} \right|_0 \mathbf{K}_q \right\|_F^2, \\
&= \sum_{j=1}^{n} \operatorname{tr} \left(\mathbf{K}_q^T \left. \frac{\partial \overline{\mathbf{H}}^T}{\partial \hat{q}_j} \right|_0 \left. \frac{\partial \overline{\mathbf{H}}}{\partial \hat{q}_j} \right|_0 \mathbf{K}_q \right), \\
&= \operatorname{tr} \left(\mathbf{K}_q^T \left(\sum_{j=1}^{n} \left. \frac{\partial \overline{\mathbf{H}}^T}{\partial \hat{q}_j} \right|_0 \left. \frac{\partial \overline{\mathbf{H}}}{\partial \hat{q}_j} \right|_0 \right) \mathbf{K}_q \right), \\
&= \operatorname{tr} \left(\mathbf{K}_q^2 \left(\sum_{j=1}^{n} \frac{\partial \overline{\mathbf{H}}^T}{\partial \hat{q}_j} \frac{\partial \overline{\mathbf{H}}}{\partial \hat{q}_j} \right) \Bigg|_0 \right),
\end{aligned} \tag{2.25}$$

where these reformulations were allowed by the linearity of the trace operation and by its invariance under similarity transformations of its matrix argument. The expression obtained in Equation (2.25) may provide the designer with more insight than could be obtained from Equation (2.24) alone, as the stiffness parameters are factored from the geometric ones. Moreover, this formulation may prove more computationally efficient, as the stiffness $\mathbf{K}_q^2$ is only multiplied once, as compared to n times in the latter formula.

2.2.1.3 Validation

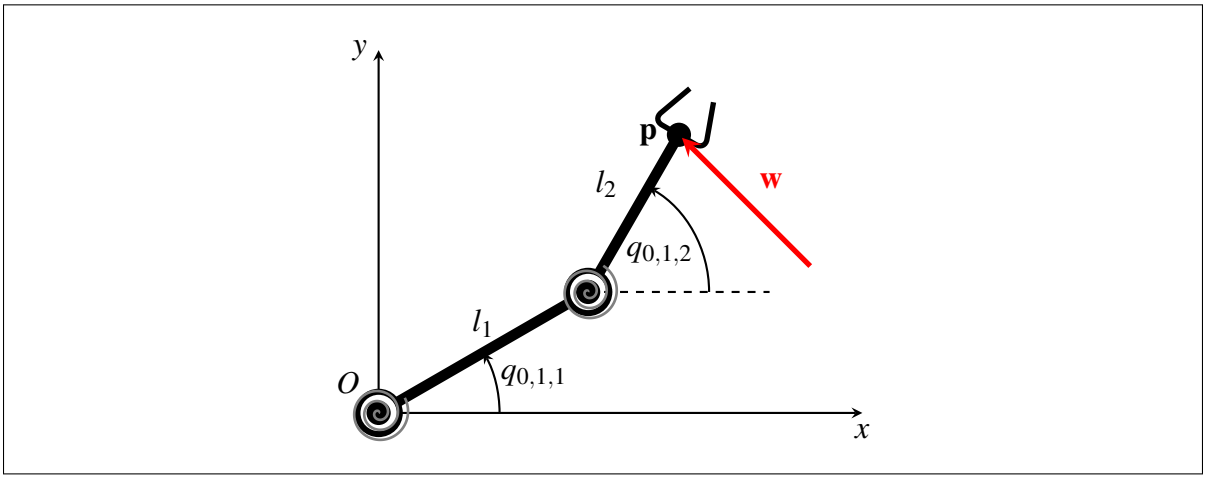

Figure 2.3 Two-link planar compliant serial mechanism

We will now perform a simple comparative analysis to verify the equivalence between the global and the local structural error indices. Figure 2.3 shows the simple planar mechanism we chose to use for this demonstration. Following the definitions described above, we assign coordinate frames, lengths of rigid links, and joint variables, as shown in Figure 2.3. The GISE and LISE are then formulated and computed for different values of $q_{0,1,2}$. A comprehensive comparison between the two yields the results of Figure 2.4. It is clear from Figure 2.4 that the indices curves are quite similar, although they are on different scales. Therefore, since the two indices result in a similar curve, it is better to use the local index, which is easily calculated, rather than the complex global one.

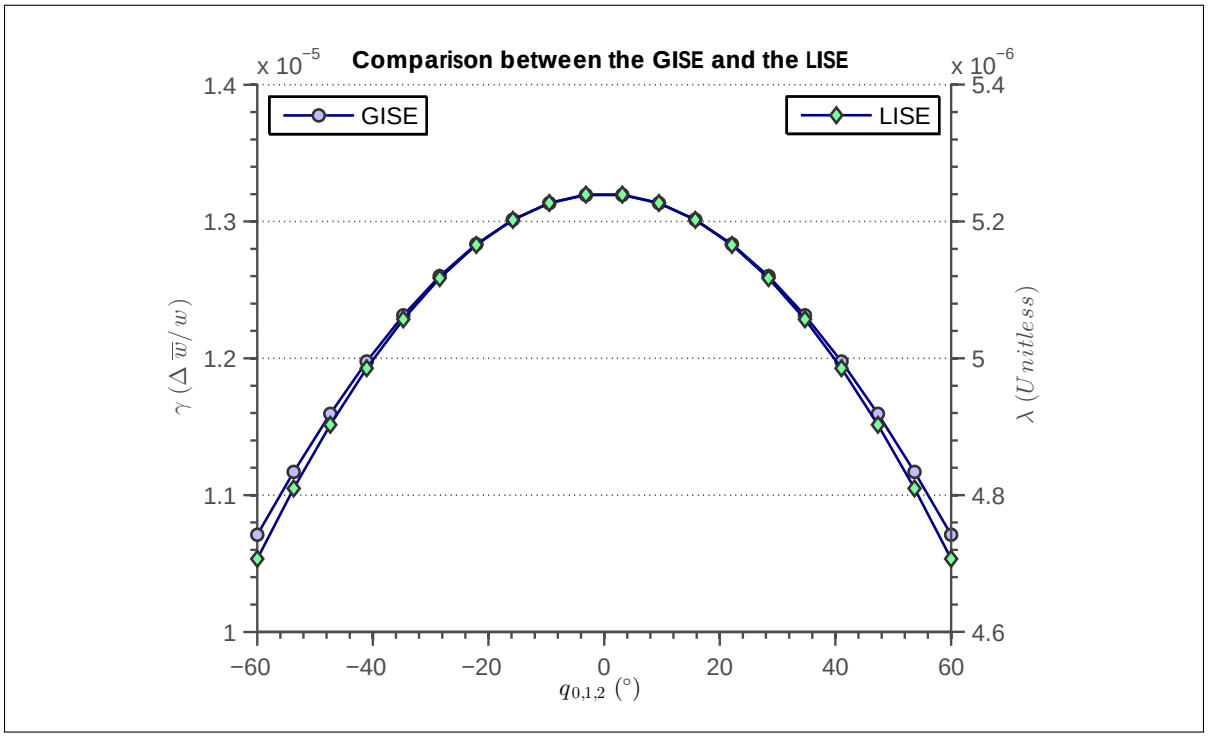

Figure 2.4 Comparison between the global and local indices of structural error

2.2.2 Measurement error amplification index

As the displacement-sensor signal has a low amplitude, and is often analog, it is easily affected by errors. These errors can be classified into three main categories: 1) the noise from the high-

frequency electromagnetic waves of electrical motors; 2) thermal drift; and 3) the errors caused by signal discretization. Let $\delta\overline{\mathbf{q}}$ be the error in $\overline{\mathbf{q}}$, and $\delta\overline{\mathbf{w}}$ be the error in $\overline{\mathbf{w}}$.

Our goal here is to quantify, with a single number, the amplification of the measurement error as it is transformed from the joint's displacement to wrench components. For this purpose, the linearized input-output relationship between $\acute{\mathbf{w}}$ and $\overline{\mathbf{q}}$ given in Equation (2.13) may be used, which yields

$$\delta\acute{\mathbf{w}} = \overline{\mathbf{H}}_0\mathbf{K}_q\delta\overline{\mathbf{q}}. \tag{2.26}$$

The *Euclidean norm* of $\delta\acute{\mathbf{w}}$, denoted $\|\delta\acute{\mathbf{w}}\|$, is bounded as

$$\|\delta\acute{\mathbf{w}}\| \leq \|\overline{\mathbf{H}}_0\mathbf{K}_q\|\|\delta\overline{\mathbf{q}}\|, \tag{2.27}$$

where $\|\overline{\mathbf{H}}_0\mathbf{K}_q\|$ is the matrix norm of its argument.

Again, from Equation (2.13), we isolate $\overline{\mathbf{q}} - \overline{\mathbf{q}}_0$, which gives

$$\overline{\mathbf{q}} - \overline{\mathbf{q}}_0 = \left(\overline{\mathbf{H}}_0\mathbf{K}_q\right)^{-1}(\acute{\mathbf{w}} - \overline{\mathbf{w}}_0). \tag{2.28}$$

From Equation (2.28), $\|\overline{\mathbf{q}} - \overline{\mathbf{q}}_0\|$ is bounded as

$$\|\overline{\mathbf{q}} - \overline{\mathbf{q}}_0\| \leq \| \left(\overline{\mathbf{H}}_0\mathbf{K}_q\right)^{-1} \|\|\acute{\mathbf{w}} - \overline{\mathbf{w}}_0\|, \tag{2.29}$$

From Equations (2.27) and (2.29), we obtain

$$\frac{\|\delta\overline{\mathbf{w}}\|}{\|\acute{\mathbf{w}} - \overline{\mathbf{w}}_0\|} \leq \left\|\overline{\mathbf{H}}_0\mathbf{K}_q\right\| \cdot \left\| \left(\overline{\mathbf{H}}_0\mathbf{K}_q\right)^{-1} \right\| \frac{\|\delta\overline{\mathbf{q}}\|}{\|\overline{\mathbf{q}} - \overline{\mathbf{q}}_0\|}$$

Finally, the maximum ratio of the relative error in $\overline{\mathbf{w}}$, divided by ratio of the relative error in $\hat{\mathbf{q}}$, may be rewritten as

$$\frac{\|\delta\overline{\mathbf{w}}\|}{\|\hat{\mathbf{w}}-\overline{\mathbf{w}}_0\|} \leq \kappa \frac{\|\delta\overline{\mathbf{q}}\|}{\|\overline{\mathbf{q}}-\overline{\mathbf{q}}_0\|}, \tag{2.30}$$

where κ is the product of the norms,

$$\kappa = \left\|\overline{\mathbf{H}}_0\mathbf{K}_q\right\| \left\|\left(\overline{\mathbf{H}}_0\mathbf{K}_q\right)^{-1}\right\| = \frac{\sigma_{\max}(\overline{\mathbf{H}}_0\mathbf{K}_q)}{\sigma_{\min}(\overline{\mathbf{H}}_0\mathbf{K}_q)}. \tag{2.31}$$

According to Equation (2.30), the noise $\delta\overline{\mathbf{q}}$ can affect $\overline{\mathbf{w}}$ through the matrix $\overline{\mathbf{H}}_0\mathbf{K}_q$. The condition number κ measures the upper bound of the relative-error amplification. From this observation, one may consider the condition number as an objective function to be minimized. In order to keep the corresponding index between zero and one, we instead choose the objective

$$1-\frac{1}{\kappa}, \tag{2.32}$$

which is to be minimized. We refer to this index as the Measurement Error Amplification Index (MEAI). The MEAI corresponds to the variation in the relative-error amplification, and may be expressed as

$$1-\frac{1}{\kappa} = \frac{\sigma_{\max}-\sigma_{\min}}{\sigma_{\max}}. \tag{2.33}$$

2.3 Multi-objective optimization

Not being completely satisfied with our formulation of the performance indices, let us propose a systematic optimization method which aims to guarantee the best possible design for a multi-axis force-torque sensor. Since we have established in this study that both the LISE and the MEAI are the main performance indicators of the sensor design, it is essential to consider both indices simultaneously in order to overcome the problems of mono-objective optimization. The following section shows how our proposed multi-objective optimization method may be used

to find the optimal design parameters for a compliant mechanism-based multi-axis force-torque sensor.

2.3.1 Formulation of the Optimization Problem

Typically in multi-objective problems, any advance made towards one objective will inevitably be offset by a decrease in the functioning of another objective. There are several techniques available for solving multi-objective optimization problems, but we have chosen to use the concept of global weighted sum, also called Pareto optimality (Censor, 1977). This method requires the user to assign weights to each objective based on their relative importance, with the resulting solutions representing a compromise between the objectives. The *Pareto optimization* method consists of determining all effective solutions, which, when plotted on a graph using a standard iterative algorithm, will lie along what is called the Pareto front. This property makes the Pareto optimization method the easiest to analyze, because of the clear visualization of the feasible and non-feasible solutions.

Let us first turn our attention towards the combination of the LISE and the MEAI using Pareto optimization. We consider the indices in Equations (2.25) and (2.32) as objective functions, each weighted by a coefficient α. Therefore, the optimization problem is concerned with the minimization of the new objective function $f(\mathbf{x}, \alpha)$ that can be subject to a number of constraints and bounds. The problem may be expressed as follows:

$$\min_{\mathbf{x}\in\mathbb{R}} \quad f(\mathbf{x}, \alpha) = \alpha\lambda + (1-\alpha)(1-\frac{1}{\kappa}) \tag{2.34a}$$

$$g(\mathbf{x}) = 0 \tag{2.34b}$$

$$g(\mathbf{x}) \leq 0 \tag{2.34c}$$

$$\mathbf{x}_{min} \leq \mathbf{x} \leq \mathbf{x}_{max} \tag{2.34d}$$

Solving the problem (2.34) for several values of α (knowing that α varies between zero and one) allows us to compare solutions based on different initial scenarios. In fact, the minimum values of LISE and MEAI occur when $\alpha = 1$ and $\alpha = 0$, respectively. All values in-between represent a trade-off between the objectives, so it is up to the designer to select the solution that will best fit within the constraints imposed by the technical specifications. Given that the choice of the vector of the design parameters $\mathbf{x}$ is arbitrary, nothing guarantees that the allowed range of measured joint displacements will match the range of applied wrenches. Thus, the constraints in Equations (2.34b) to (2.34d) can be used to scale the input and output of Equation (2.11). In Matlab®, we solved the constrained nonlinear optimization problem using the *fmincon* command. This command prompts the sequential quadratic programming routine of Matlab® which is used to implement the Pareto optimization procedure.

2.4 Case study: optimization procedure applied to a serial two-link mechanism

To illustrate the core ideas of this chapter, this section will show how the optimization procedure may be applied to the structural dimensioning of a compliant-serial mechanism. Here we present our evaluation of the performance of a two-link planar mechanism with two pivot joints. As this is the simplest type of multi-joint serial mechanism, obviously it will not be used as a compliant mechanism at the core of a real multi-axis force-torque sensor. Nevertheless, this example serves to provide a simplified illustration of the proposed design method.

2.4.1 Mechanism description and kinematics

The proposed serial mechanism, with two degrees of freedom, is shown in Figure 2.3, where the point of force application is denoted $\mathbf{p}(x,\ y)$. Likewise, the position of the joints is indicated by $\mathbf{q} = [q_{0,1,1},\ q_{0,1,2}]^T$. We consider the joint stiffness matrix $\mathbf{K}_q$ to be a diagonal matrix. In this example, the vector of maximum applied wrench is $\mathbf{w}_{\max} = [5,\ 5]$ N, the vector of minimum applied wrench is $\mathbf{w}_{\min} = [-5,\ -5]$ N, and the range of joint displacements extends from -0.3 rad to +0.3 rad (i.e., $\Delta\hat{q} = 0.6$ rad).

We must place limits on the design parameters to avoid impractical solutions. These boundaries, and other details of the optimization problem, are presented in Table 2.1. Our objective is to find the set of design parameters $\mathbf{x} = [q_{0,1,1},\ q_{0,1,2},\ l_1,\ l_2,\ k_{1,1},\ k_{1,2}]^T$ that minimize the objective function given in Equation (2.34a).

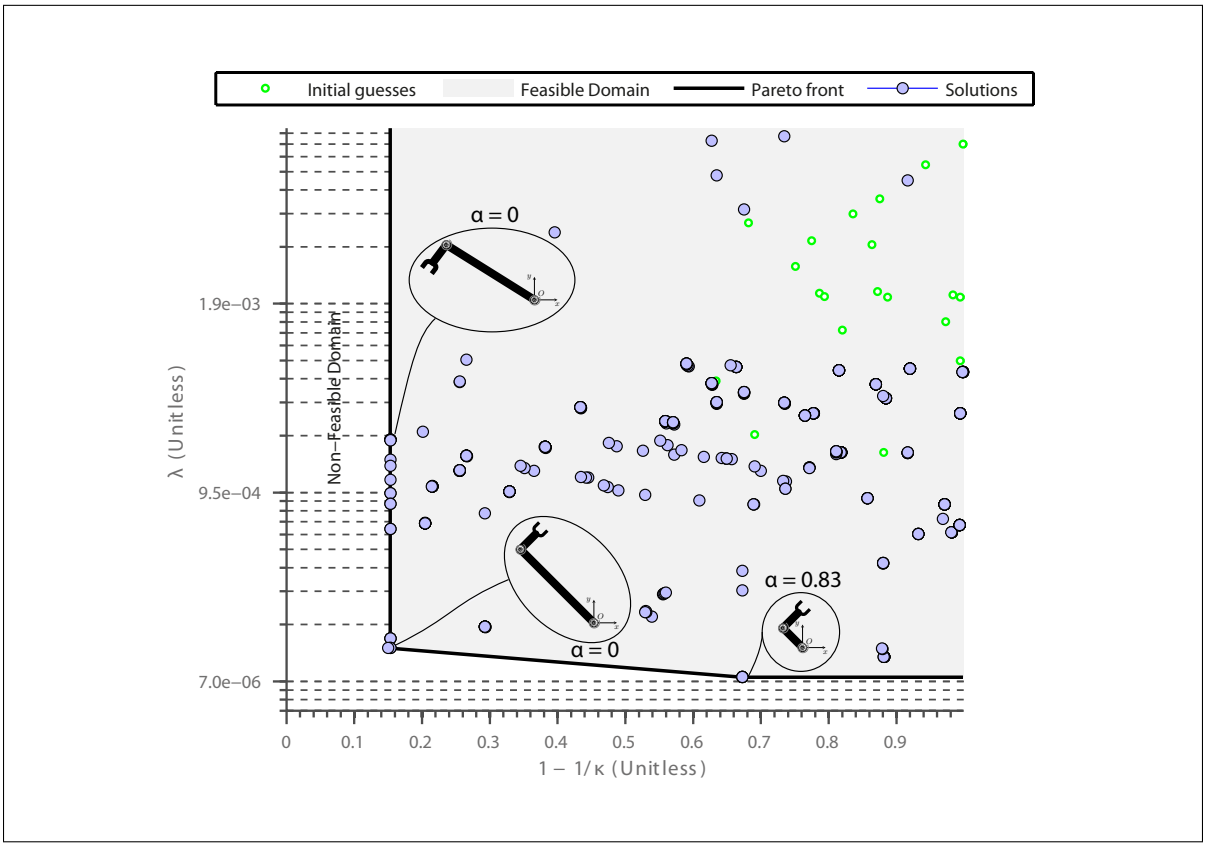

Figure 2.5 Results of Pareto optimization for the two-link planar mechanism

2.4.2 Optimization results for the serial two-link mechanism

The indices presented in Equations (2.25) and (2.32) can be formulated using the Jacobian matrix involved in the kinematic equations of the two-link serial mechanism (McCarthy, 1990). The resulting formulas are then used to solve the optimization problem (2.34). Figure 2.5 shows the Pareto front obtained from a logarithmically-spaced sequence of α and several randomly generated initial guesses. We observe from Figure 2.5 that by properly modulating the

input design parameters, both the LISE and MEAI have improved, as $1-1/\kappa$ ranges from 0.15 to 1 and λ ranges from $1.05\cdot10^{-5}$ to $7.6\cdot10^{-3}$. Due to the large number of possible solutions, we focus on the three most promising designs. These are shown in Figure 2.5 and compared in Table 2.1. The first and second scenarios result in solutions where only $1-1/\kappa$ is minimized (i.e., $\alpha=0$). We found that the minimum of the MEAI exists at design solutions where the ratio $l_1:l_2$ is highest, and $q_{0,1,2}$ is equal to $\pm90^\circ$. The third scenario represents an intermediate Pareto optimal solution, since both indices have improved relative to the indices generated by the initial guesses. In this case, the minimum of the LISE and the MEAI occurs at design solutions where the ratio $l_1:l_2$ is lowest. One may also observe from Table 2.1 that the only components that vary with optimization are $q_{0,1,2}$–i.e., the joint stiffnesses and the link lengths–whereas $q_{0,1,1}$ remains constant. This observation is consistent with the theory of serial mechanisms (Yoshikawa, 1985), since the first joint variable affects neither the Jacobian matrix of the mechanism, nor the indices derived from this matrix.

Table 2.1 Optimization results for the two-link planar mechanism

$\mathbf{x}$	$q_{0,1,1}$	$q_{0,1,2}$	l_1	l_2	$k_{1,1}$	$k_{1,2}$	$1-\frac{1}{\kappa}$	λ
	rad	rad	mm	mm	Nm/rad	Nm/rad	NA	NA
$\mathbf{x}_{min}$	0	-1.57	10	10	1	1	NA	NA
$\mathbf{x}_{max}$	3.14	1.57	60	60	687	687	NA	NA
$\mathbf{x}_0$	Initial parameter settings, selected by estimation							
	2.59	0.12	44.8	17.3	305	74.2	0.99	$4.9\cdot10^{-4}$
	2.37	-0.7	35.3	34.6	112	82.72	0.88	$1.6\cdot10^{-4}$
	2.37	-0.7	35.3	34.6	112	82.72	0.88	$1.6\cdot10^{-4}$
$\alpha=0$	2.59	1.57	60	10	112	684	0.15	$18.9\cdot10^{-5}$
$\alpha=0$	2.37	-1.57	60	10	31.6	192	0.15	$1.4\cdot10^{-5}$
$\alpha=0.83$	2.37	-1.57	12.3	10	112	82.7	0.67	$10.5\cdot10^{-6}$

2.5 Case study: application to the 2-PRR planar force sensor

This section first presents a 2-PRR compliant parallel mechanism-based force sensor, including the mechanism principle and kinematics, in order to show the versatility of the proposed design

method. It will then display the contour plots of the proposed performance indices. Finally, the results for the optimized 2-PRR compliant mechanism are depicted and discussed.

2.5.1 Sensor description and kinematics

As a practical example, consider the design of a planar multi-axis force sensor for measurement of the force $\mathbf{w} \in \mathbb{R}^2$, as illustrated in Figure 2.6. The compliant mechanism of this force sensor will allow for planar displacements at the position of joint q_3, represented by $\mathbf{p} \equiv [x,\ y]^T$. Displacements will only take place on the $x-y$ plane, as the joint is too stiff to allow displacements in other directions. Therefore, the compliant mechanism can simply be modeled as the lumped-elastic parallel mechanism of Figure 2.6.

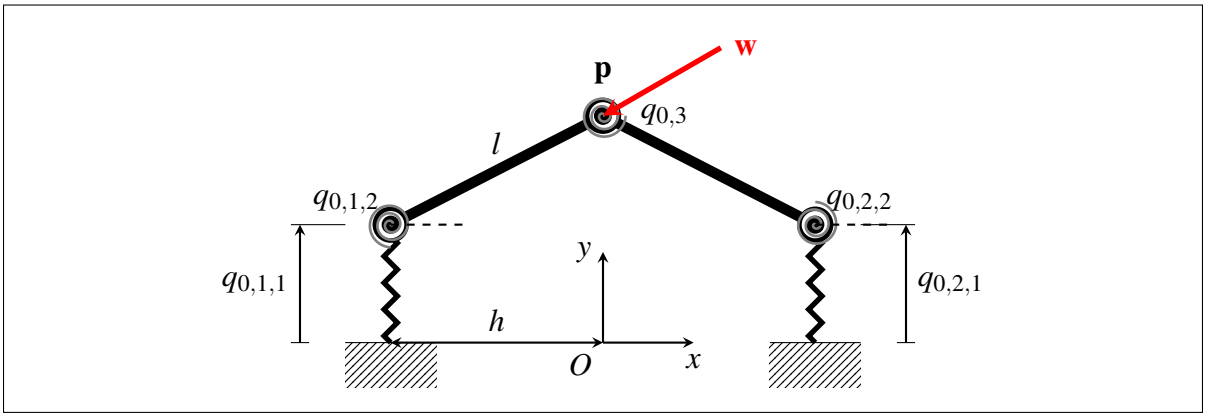

Figure 2.6 A 2-PRR planar biaxial force sensor mechanism

According to this model, the point of application of the force is connected to the frame by two *PRR*-type legs. Each pivot joint is coupled with a torsion spring, and each prismatic joint with a linear spring. We assume the architecture of the mechanism to be symmetrical. Let us define the vectors $\mathbf{q}_i \equiv [q_{i,1},\ q_{i,2}]^T$, $i = 1,\ 2$, representing the joint displacements; the vector $\hat{\mathbf{q}} \equiv [q_{1,1},\ q_{2,1}]^T$, representing the measured joint variables; the vector $\check{\mathbf{q}} \equiv [q_{1,2},\ q_{2,2}]^T$, representing the unmeasured joint variables; and the vector $\mathbf{q}_0 \equiv [q_{0,1,1}\ \cdots\ q_{0,2,2}]^T$, representing the free lengths of the corresponding springs.

It is more complex to compute the stiffness matrix $\mathbf{K}_q$, due to the presence of a fifth spring located between the two bars connected at $\mathbf{p}$. This spring is of stiffness k_3 and free-length $q_{0,3}$, and its elongation is given by $q_3 - q_{0,3}$, where $q_{0,3}$ is the angle between the two bars. As this angle depends upon $q_{0,1,2}$ and $q_{0,2,2}$, it was excluded from the vectors $\mathbf{q}$ and $\mathbf{q}_0$. Thus, the contribution of the spring k_3 to the matrix of stiffness is $\mathbf{k} = [k_{1,1},\ k_{1,2}+k_3,\ k_{2,1},\ k_{2,2}+k_3]^T$, where $\mathbf{K}_q \equiv \mathrm{diag}(\mathbf{k})$.

The inverse kinematic problem of this mechanism consists in expressing the free lengths of the measured joint displacements $\hat{\mathbf{q}}_0 = [q_{0,1,1},\ q_{0,2,1}]^T$ as functions of the position $\mathbf{p} = [x,\ y]^T$ of application of the force $\mathbf{w}$. We refer the reader to Merlet (1997) for the complete derivation. As the purpose of this chapter is not to discuss the full details of the kinematics, we present only the solution to the inverse kinematic problem,

$$\begin{aligned} q_{0,1,1} &= y \pm \sqrt{(l^2 - (x+h)^2)}, \\ q_{0,2,1} &= y \pm \sqrt{(l^2 - (x-h)^2)}, \end{aligned} \tag{2.35}$$

where h is the distance between the center of the base frame and the axis passing through the fixed linear joint. The symbol $\pm$ in the system of Equation (2.35) indicates the four possible sets of solutions to this problem. For the purpose of this example, we retain only the solutions that correspond to the negative branches of Equation (2.35), i.e., those postures where $q_{0,1,1} \leq y$ and $q_{0,2,1} \leq y$.

2.5.2 Performance indices of the 2-PRR planar force sensor

One way to easily infer the critical behavior of the indices at specific geometries is to trace the contours of the proposed performance indices over a two-dimensional design space. Figure 2.6 shows that nine variables can be admitted as design parameters: $q_{0,1,1}$, $q_{0,2,1}$, l, h, $k_{1,1}$, $k_{1,2}$, $k_{2,1}$, $k_{2,2}$, and k_3. These variables may each have a significant impact on the force-displacement relation of Equation (2.11). Computing and tracing the relationships between the three indices and all nine design parameters is tedious and impractical. Therefore, we initially restrict our-

selves to the consideration of just two of them at a time. As an example, let us determine the values of $q_{0,1,1}$ and $q_{0,2,1}$ that will result in the best possible design.

We assume that the measured joint variables $q_{0,1,1}$ and $q_{0,2,1}$ vary from 30 mm to 60 mm, and that the mechanism has a symmetric stiffness matrix, i.e., $k_{1,1} = k_{2,1}$ and $k_{1,2} = k_{2,2}$. The remaining parameters are set to: $l = 40$ mm, $h = 25$ mm, $k_{1,1} = k_{2,1} = 9.66 \cdot 10^3$ N/m for the linear joints, and $k_{1,2} = k_{2,2} = 33.7$ Nm/rad for the angular joints. As stated in Section 2.2, the designer knows in advance that the variation in the position of the vector $\hat{\mathbf{q}}$ with respect to $\hat{\mathbf{q}}_0$ is equal to the maximum deformations allowed at the compliant measured joints. Therefore, the vector $\Delta\hat{\mathbf{q}} = \hat{\mathbf{q}} - \hat{\mathbf{q}}_0$ is equal to the range of the sensor that is placed on the relevant joint. For example, if the joint's range of motion, $q_{1,1}$, extends from -0.3 mm to +0.3 mm, then $\Delta\hat{q}$ = 0.6 mm. In addition, the vectors of the minimum and maximum applied wrenches are, respectively, $\mathbf{w}_{\min} = [-5 \ -5]$ N and $\mathbf{w}_{\max} = [5 \ \ 5]$ N.

Having defined the parameters, we will now compute the index γ from Equation (2.15). This is calculated three times along 50-by-50 grids, according to three separate assumptions regarding the ranges of joint displacements: $\Delta\hat{q}$ = 0.3 mm, $\Delta\hat{q}$ = 0.6 mm, and $\Delta\hat{q}$ = 0.9 mm. Figure 2.7 depicts the resulting contour plots of each γ index, showing how the index relates to the level of $\Delta\hat{\mathbf{q}}$. As can be seen, the index γ with the lowest value corresponds to the lowest value of $\Delta\hat{\mathbf{q}}$, i.e., to the design in which the measured joints exhibits the least displacement magnitude. This result is to be expected, as the theory discussed earlier states that a smaller range of the joint displacements values results in lower values of the GISE.

The next step is to generate three separate performance indices and transform them into Cartesian space for simple visualization. We used the method described in the previous paragraph to calculate the values of three separate indices in the joint space. From Equations (2.15), (2.25), and (2.32), we can compute γ, λ, and $1 - 1/\kappa$ for the 2-PRR mechanism according to the design parameters specified above. These were then transformed into Cartesian space using inverse kinematics, to obtain the contour plots of the GISE, the LISE, and the MEAI.

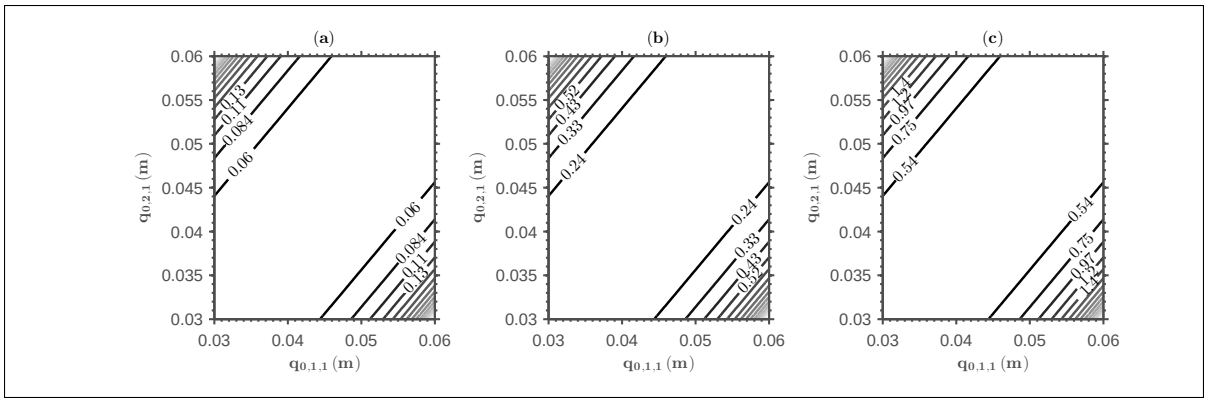

Figure 2.7 Comparison of the contour plots of the GISE for the 2-PRR mechanism: (a) $d\hat{\mathbf{q}} = 0.3$ mm, (b) $d\hat{\mathbf{q}} = 0.6$ mm, and (c) $d\hat{\mathbf{q}} = 0.9$ mm

Based on the simulation results, we can now compare the three indices to determine which design performs best. From Figure 2.8(a) and Figure 2.8(b), one may observe that the contour lines of γ are quite similar to those of λ. Therefore, the use of one of these contours instead of the other to select the values of x and y does not affect the final design, except that the values of λ are proportionally higher than those of γ. Note that these values could just as easily have been lower, since both the GISE and the LISE are dimensionless (without a unit of measurement). In regards to Figure 2.8(c), one may observe that the contour lines of $1 - 1/\kappa$ are also similar to those of the GISE and the LISE. Nevertheless, the LISE cannot be replaced by the MEAI since the latter does not take into account the properties of the springs attached to the unmeasured joint of the compliant mechanism. The next section of this chapter will present a follow-up to this analysis. We will describe how the optimization procedure shown in Section 2.3 can be used to further improve the performance indices when optimizing several parameters at once.

2.5.3 Optimization results for the 2-PRR planar force sensor

In this section, we examine how the performance of the 2-PRR compliant mechanism can be improved when the rest of the design parameters are included as part of the optimization process. For this purpose, the design parameters are optimized to improve both the LISE and the MEAI according to the problem of Equation (2.34). As previously mentioned, the parameters

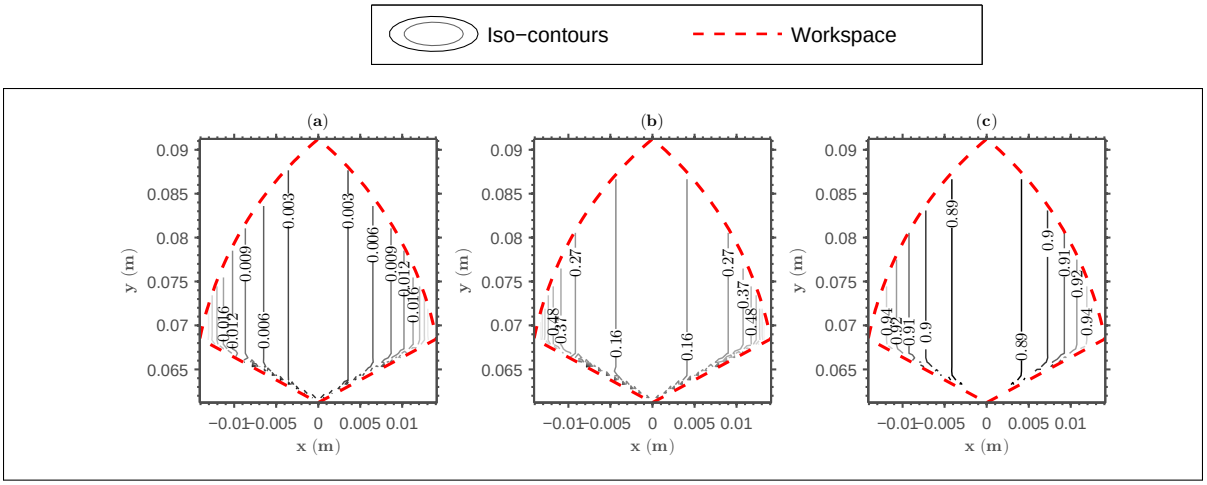

Figure 2.8 Contour plots in Cartesian space of the performance indices for the 2-PRR mechanism: (a) GISE, (b) LISE, and (c) MEAI

are grouped in the vector $\mathbf{x} = [q_{0,1,1},\ q_{0,2,1},\ l,\ h,\ k_{1,1},\ k_{1,2},\ k_3]$, and we assume $k_{1,1} = k_{2,1}$ and $k_{1,2} = k_{2,2}$. Also, as in section 2.5.2, the vectors of minimum and maximum applied wrenches are, respectively, $\mathbf{w}_{\min} = [-5\ \ -5]$ N and $\mathbf{w}_{\max} = [5\ \ 5]$ N, and the range of measured joint displacements is $\Delta\hat{q} = 0.6$ mm. Again, we must place limits on the design parameters to avoid impractical solutions. These boundaries, and other details of the optimization problem, are presented in Table 2.2.

Table 2.2 Results of the optimization process for the 2-PRR planar mechanism

$\mathbf{x}$	$q_{0,1,1}$	$q_{0,2,1}$	l	h	$k_{1,1}$	$k_{1,2}$	k_3	$1-1/\kappa$	λ
	mm	mm	mm	mm	N/m	Nm/rad	Nm/rad	NA	NA
$\mathbf{x}_{min}$	35	35	40	25	1.66	1	1	NA	NA
$\mathbf{x}_{max}$	50	50	60	39	$9.6\cdot10^3$	687	687	NA	NA
$\mathbf{x}_0$	Initial parameter settings, selected by estimation								
	39	45	51.3	27	$2.08\cdot10^3$	1.48	1.12	0.22	$6.2\cdot10^{-3}$
	35	38	52.1	37.2	$6.18\cdot10^3$	12.37	4.35	0.55	$25.8\cdot10^{-3}$
	40.3	41.7	47.3	26.5	$3.19\cdot10^3$	1.24	4.12	0.43	$11.6\cdot10^{-3}$
$\alpha = 0.60$	35	35	60	30.6	$2.08\cdot10^3$	1.36	1.28	$1.81\cdot10^{-6}$	$5.3\cdot10^{-3}$
$\alpha = 0.37$	35	35	60	26.1	$6.18\cdot10^3$	6.63	1.00	$1.33\cdot10^{-7}$	$1.72\cdot10^{-2}$
$\alpha = 0$	35	35	60	32.9	$3.19\cdot10^3$	1.08	2.89	$2.21\cdot10^{-7}$	$8.02\cdot10^{-3}$

Because we wish to minimize both the LISE and the MEAI, the optimization problem is multi-objective. We thus expect to obtain several optima corresponding to as many values of α in

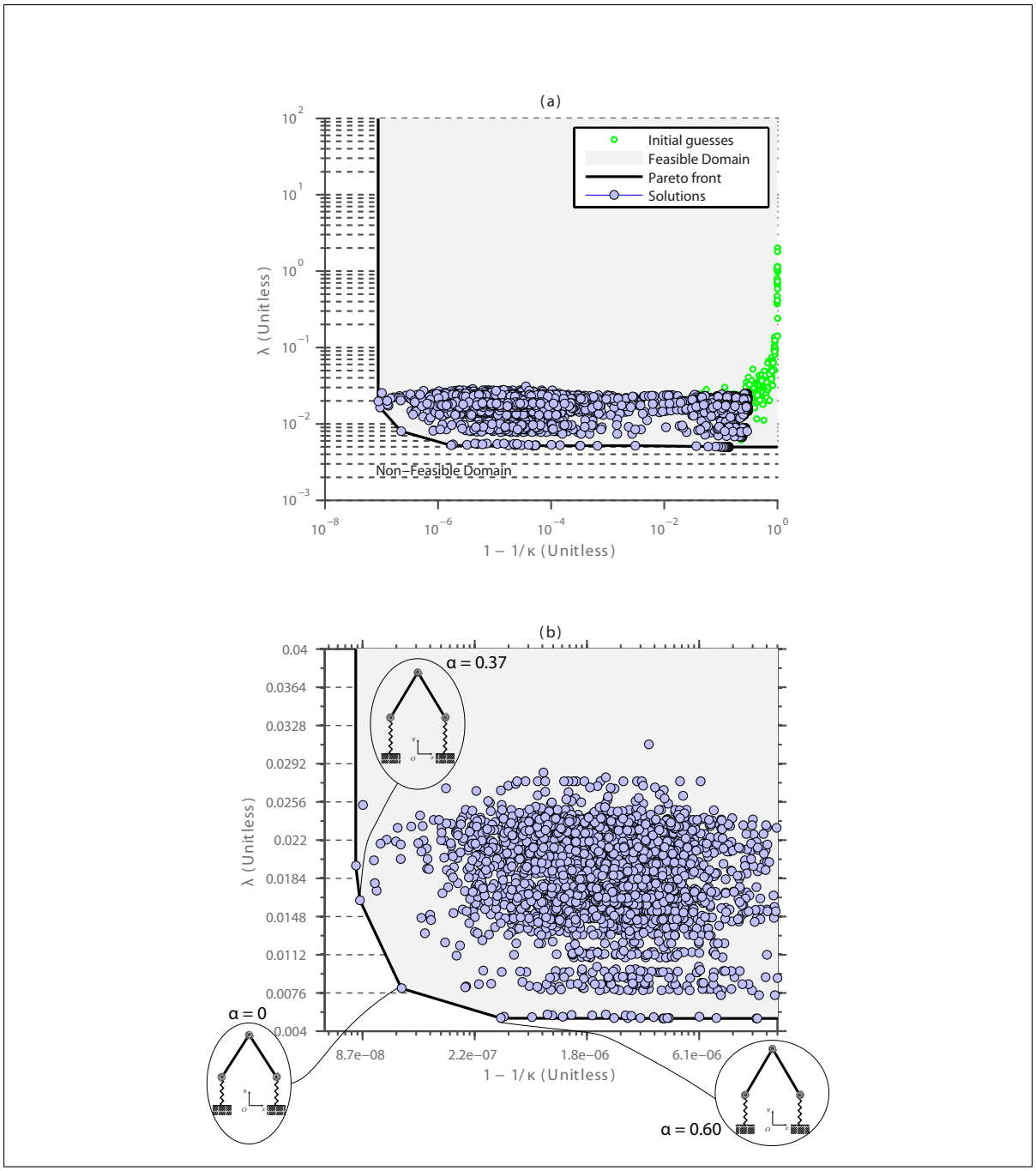

Figure 2.9 Pareto optimization for the 2-PRR planar mechanism: (a) overview of the initial guesses and possible solutions in the feasible and non-feasible domains, (b) close-up view of the concentration of solutions at the Pareto front

problem (2.34). Figure 2.9(a) presents the solutions obtained from a logarithmically-spaced sequence of α and 50 randomly generated initial guesses. The boundary of the 8750 ensuing solutions approximates the Pareto front. We believe that these solutions cover the seven-dimensional design space sufficiently well for our purpose. Note that this figure shows a high concentration of randomly generated initial guesses in the northeast area of the graph. This result can clearly be seen in Figure 2.9(b). The fact that the cloud of initial guesses resulted in a cloud of optimized solutions in the southwest area of the graph shows that we were able to generate many improved solutions within our design constraints. Ultimately, λ reaches a minimum value of $5.2 \cdot 10^{-3}$, and $1 - 1/\kappa$ reaches a minimum value of $8.7 \cdot 10^{-8}$. The latter value corresponds to the condition number of one (an isotropic design), although as of yet we have not found one design that obtains precisely these two minima at the same time.

Each solution on the Pareto front represents the parameters that optimize a certain weighted sum of different functions for the design of the compliant mechanism. Examples of possible design solutions are given in Table 2.2, along with their corresponding performance indices λ and $1 - 1/\kappa$. The different solutions found on the Pareto front actually result in the same values for some of the corresponding design parameters. For instance, all the solutions shown on the Pareto front require the same design parameters: the geometry of the mechanism must be symmetric, i.e., $q_{0,1,1} = q_{0,2,1}$, and the ratio between the parameters l and h, if found, is approximately 1:2. However, for our multi-axis force sensor, each solution is the result of a trade-off between the sensor sensitivity to noise from the displacement sensors, and its sensitivity to non-linearities resulting from changes in geometry. Therefore, the decision to optimize one of these functions (at the expense of the other) ultimately rests with the designer.

2.6 Conclusion

In this chapter, we have proposed and validated a novel method of designing the compliant mechanism that forms the core of multi-axis force-torque sensors. More specifically, we have used the kinetostatic relationship between applied wrench and measured joint displacements to formulate several indices. These indices are used in the multi-objective optimization process,

based on Pareto-optimization, to find the best design. Assuming that the compliant mechanism can be modelled as a lumped compliance rigid-link mechanism, these performance indices can be applied to any sensor mechanism, allowing us to quantify the structural error using the GISE or LISE, and to quantify the measurement error amplification using the MEAI. The most important aspects of the performance indices are summarized as follows:

a. The indices take several variables into account, allowing the designer to obtain a sensor that meets the specifications he or she desires.

b. However, since the indices are based on the wrench-displacement relationship, it is relatively complex to compute the indices for any mechanism with six degrees of freedom.

c. Finally, the indices apply to any compliant mechanism, kinematically redundant or not.

In order to illustrate the applicability of the proposed design method, we applied it to a 2-link compliant-serial mechanism and a 2-PRR compliant-parallel mechanism. The results show that the optimization process does improve the indices, and in theory, the design. However, to fully validate the indices, we must manufacture the mechanisms, test them, and determine whether they are indeed optimal designs.

CHAPTER 3

MECHANICAL ANALYSIS OF THE MULTI-AXIS FORCE-TORQUE SENSOR DESIGN

3.1 Introduction

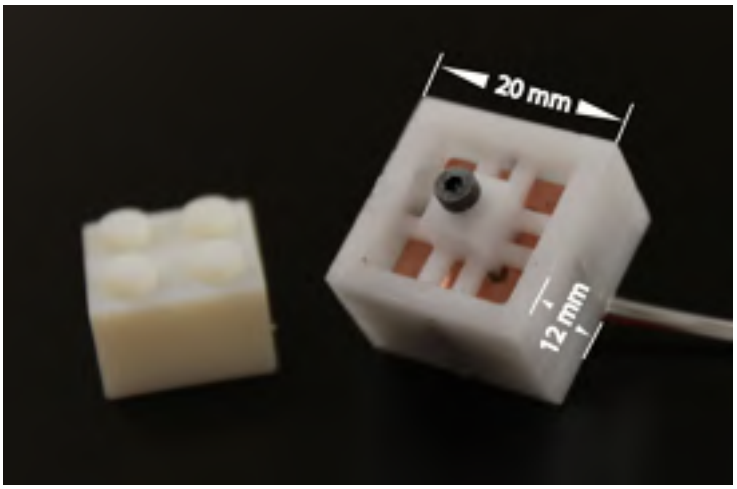

Figure 3.1 Photograph of the triaxial force sensor prototype showing its precise dimension

In the literature (Diddens *et al.*, 1995; Chapuis *et al.*, 2004; Beyeler *et al.*, 2009a; Ranganath *et al.*, 2004b), most of the multi-axis force-torque sensors have the same operating principle. A wrench vector applied on the sensor will lead to a structural deformation of its compliant parts. The resulting deflection is measured at a given point and converted into an analog or digital signal using a given technology of displacement sensing. The geometry of the structure and the displacement sensor technology are crucial characteristics of the sensor, and they must be included in the mechanical design process. Indeed, a variety of multi-axis force-torque sensors have been designed by different authors (Uchiyama and Svinin, 1995; Jin *et al.*, 2003; Ranganath *et al.*, 2004a) using several design methods. In 2012, Puangmali *et al.* (2012) published the design of a miniature 3-axis force sensor by combining a monolithic structure and opti-

cal fiber technology. From a mechanical point of view, their sensing principle is quite similar to that proposed in this study. Although each of these multi-axis force-torque sensors design methods has its own advantages, all suffer from at least one of the drawbacks highlighted in Chapter 1.

To address these issues, this chapter presents a new mechanical design method that uses analytical tools in order to model and optimize the compliant structure, taking into account constraints such as the force measurement ranges, the maximum displacements at the capacitive sensors and the dimensional constraints on the sensor geometry. We also presents the design of a novel triaxial force sensor. In addition to being inexpensive to produce, the sensor presents good performances. This is mainly due to the proposed mechanical design method, which uses analytical tools in order to find the optimum structure dimensions from the specifications of the application (force range, size, stiffness). The proposed multi-axis force sensor, which is shown in Figure 3.1, uses four capacitive displacement sensors coupled with an inexpensive capacitance-to-digital converter (CDC) to sense the displacement of the optimized compliant structure. This method of measuring the displacement directly returns a digital output signal, and is very robust to the typical surrounding noise of a robotic environment. Moreover, in order to increase its sensitivity, our sensor uses a special nano filled silicone with a high dielectric constant, which maximizes the capacitance variation under a given load.

The chapter is organized as follows: Sections 3.2 and 3.3 respectively present the mathematical analysis of the problem and the Optimization procedure. Section 3.4 presents the working principle and the optimization of the mechanical structure. Then, the capacitive displacement acquisition circuit and its optimization are described in Section 3.5. Section 3.6 deals with the fabrication of the sensor. In Section 3.7, the characterization of the sensor is carried out by some experimental tests.

3.2 Mathematical analysis

The first step towards the design of a multi-axis force-torque sensor is its mathematical modeling. Here, we opt for a symbolic mathematical model of the compliant structure. To understand how this six-degree-of-freedom kinetostatic model is developed, let us first consider a simple one-degree-of-freedom model.

3.2.1 Wrench-displacement relationship

In order to clarify the dependence between the wrench-displacement relationship and the geometry of the sensor structure, we begin with the analysis of a cantilever beam subjected at its free end to the shear force f, as shown in Figure 3.2. Here and in the rest of the chapter, we assume that the material which constitutes the multi-axis force-torque sensor is homogeneous, isotropic, and elastic. Thus, small deformations lead to a proportional relation between the free-end displacement δx and the force f. The relationship may be expressed as

$$f = k\delta x. \tag{3.1}$$

Using Hooke's law, the stiffness of a straight, uniform beam may be expressed as

$$k = \frac{3EI}{l^3}. \tag{3.2}$$

where E is Young's modulus, $I = \frac{wh^3}{12}$ is the moment of inertia, l is the beam length, w and h are respectively the width and height of the beam. From Equations (3.1) and (3.2), we highlight the importance of the cantilever beam geometry to define the relationship between the input (force) and the output (displacement) of the cantilever. In the case of the mechanical structure of a multi-axis force-torque sensor, developing a model of the stiffness is much more complex. This is what is outlined in the following section.

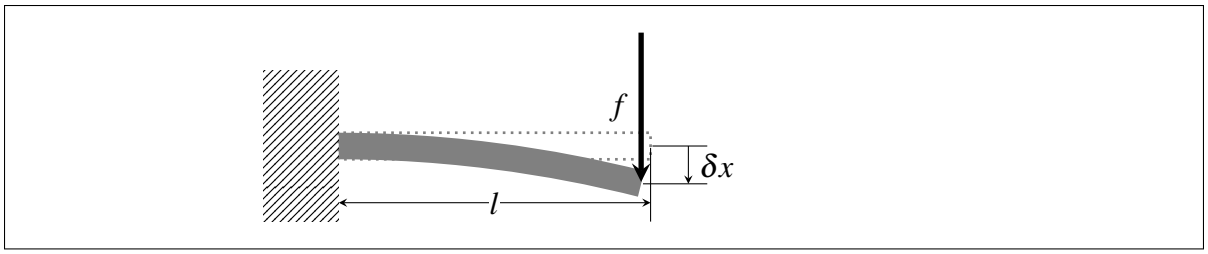

Figure 3.2 Cantilever beam diagram

3.2.2 Elastostatic model

We wish to obtain a relationship between the inputs and outputs of the multi-axis force-torque sensor, the former being the applied wrench **w**, the latter being the displacements **x** of the suspended rigid mass. This is under the hypothesis that the material is perfectly elastic, and that the applied wrench varies at frequencies well below the lowest natural frequency of the structure, i.e., that the system can be assumed *quasistatic*.

Nowadays, the more popular approach to computing the wrench-displacement relationship is the finite element method. Although useful to model the elastostatic properties of complex architectures, this approach is numerically costly. For this reason, it does not seem better suited for structural optimization, where the result quality depends on the number of design solutions modeled and tested.

Instead, we propose a symbolic model of the wrench-displacement relationship. The small displacements found in multi-axis force-torque sensors and the fact that their compliant elements can generally be assimilated to Euler-Bernoulli beams make them good candidates for symbolic analysis. A symbolic model allows a deeper understanding of the relationships between the design parameters. In particular, it sheds light on the interplay between design parameters and cross-axis sensitivities. Finally, the computational cost of numerical methods like the finite element method being generally greater, having a simple symbolical model speeds up computations, and allows the optimization of the structure over numerous design parameters.

The elastostatic model we use is drawn from the *lumped* elastodynamic model proposed in (Cardou *et al.*, 2008). "Lumped" refers to the assumption that the compliant elements act as massless ideal springs, whereas the other bodies are treated as rigid masses. Naturally, the elastostatic model is obtained by discarding the dynamic terms of the elastodynamic model. This leaves us with the linear relationship between the applied wrench $\mathbf{w}$ and the mass displacements in space $\mathbf{x}$

$$\mathbf{w} = \mathbf{K}\mathbf{x}, \tag{3.3}$$

where $\mathbf{K} \in \mathbb{R}^{6\times 6}$ is the classical stiffness matrix.

The symbolic derivation of $\mathbf{K}$ is a basic concept, which revolves around the application of Castigliano's theorem to an expression of the potential energy based on screws. Because of space constraints, let us refer the reader to Cardou *et al.* (2008) for a complete account. Here, we simply state the resulting expression for the simpler case where there is only one rigid mass, its displacements being expressed in the fixed frame:

$$\mathbf{K} = \sum_{i=1}^{m} \left(\int_0^{l_i} \mathbf{S}_i(s_i)\mathbf{H}_i(s_i)\mathbf{S}_i(s_i)^T ds_i \right)^{-1}. \tag{3.4}$$

In this equation, l_i is the length of the i^{th} beam and s_i is a curvilinear coordinate along its neutral axis, as shown in Figure 3.3. m is the number of beams acting in parallel to suspend the rigid mass. $\mathbf{S}_i$ is the twist-transfer matrix associated with screw $\mathbf{s}_i$, i.e., the matrix taking the wrench $\mathbf{u}_i$ applied on the i^{th} beam cross-section from frame $\mathscr{S}_i$ to frame $\mathscr{F}$. Symbolically, it is expressed as

$$\mathbf{S}_i = \begin{bmatrix} e^{\text{cpm}(\tau_i)} & \mathbf{0}_{3\times 3} \\ \text{cpm}(\sigma_i)e^{\text{cpm}(\tau_i)} & e^{\text{cpm}(\tau_i)} \end{bmatrix}, \text{ where } \mathbf{s}_i \equiv \begin{bmatrix} \tau_i \\ \sigma_i \end{bmatrix}, \tag{3.5}$$

$\tau_i \in \mathbb{R}^3$ is the array of the products of natural invariants of the rotation taking frame $\mathscr{F}$ onto $\mathscr{S}_i$, σ_i is the vector from O to S_i, and $\text{cpm}(\,\cdot\,)$ is the cross-product matrix[1]. Notice that $\mathbf{S}_i$ is a function of s_i through τ_i and σ_i, i.e., it varies according to the location where the cross-section of beam i is taken. Finally, $\mathbf{H}_i$ contains the properties of this cross-section, and is defined

[1] $\text{cpm}(\mathbf{a})$ is defined as $\partial(\mathbf{a}\times\mathbf{x})/\partial\mathbf{x}$, for any $\mathbf{a},\mathbf{x} \in \mathbb{R}^3$.

according to the strain energy formulas for beams:

$$\mathbf{H}_i(s_i) \equiv \text{diag}\left(\frac{1}{G_i J_i}, \frac{1}{E_i I_{Y,i}}, \frac{1}{E_i I_{Z,i}}, \frac{1}{E_i A_i}, \frac{\alpha_{Y,i}}{G_i A_i}, \frac{\alpha_{Z,i}}{G_i A_i}\right), \tag{3.6}$$

where E and G are the Young and the shear moduli, respectively; $I_{Y,i}$, $I_{Z,i}$ and J_i are the $Y_{\mathscr{S},i}$-axis moment of inertia, the $Z_{\mathscr{S},i}$-axis moment of inertia, and the torsional modulus of the beam cross section, respectively[2]; A_i is the area of the cross-section; and $\alpha_{Y,i}$ and $\alpha_{Z,i}$ are the shearing effect coefficients for the $Y_{\mathscr{S},i}$ and $Z_{\mathscr{S},i}$ directions, respectively. Notice that all these parameters could be functions of the curvilinear coordinate s_i, should the beam cross-section vary along its length.

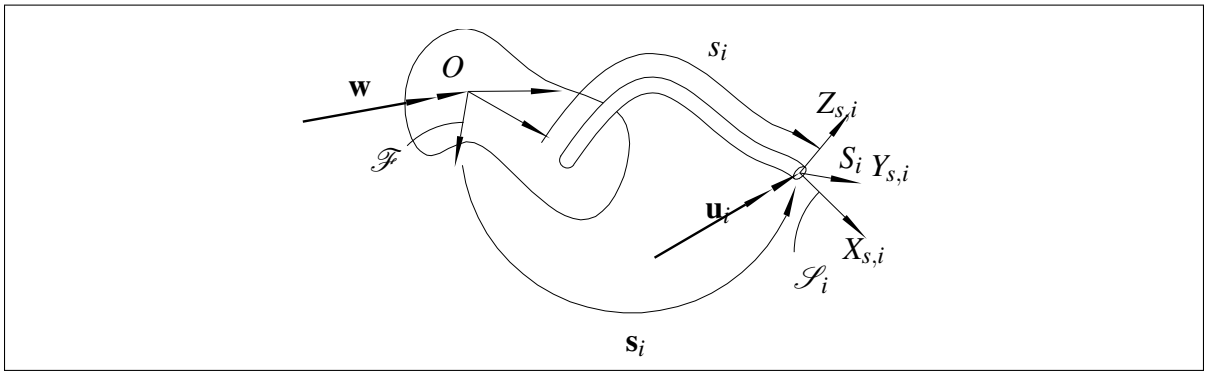

Figure 3.3 The suspended mass and its i^{th} compliant link

3.3 Optimization procedure

The improvement of a multi-axis force-torque sensor architecture from a topology intuition would usefully supplement the qualitative analysis. That is why we consider adequate to implement a systematic optimization procedure, including with regard to practical considerations, such as the displacement-sensor specifications, manufacturing tolerances, and other parameters. In fact, this set of equality and inequality restrictions form a basis for addressing the selection of the design parameters from a given performance index.

[2] $I_{Y,i}$, $I_{Z,i}$ and J are defined with respect to the centroid of the cross-section.

The optimization results depend on both the accuracy of the mathematical model and the efficiency of the optimization algorithm. Thus, the symbolic model we obtained from the Euler-Bernoulli beam theory allows the efficient computation of the stiffness matrix $\mathbf{K}$ from the decision variables. In turn, this stiffness matrix can be used to link a wrench applied on the suspended mass to the corresponding measurements picked up at the displacement sensors. The relationship is linear, and can thus be represented by the matrix $\mathbf{X} \in \mathbb{R}^{m\times 6}$, where m is the number of displacement sensors measuring the suspended mass motion. In fact, each column of the matrix represents the displacement of the tracked points of the suspended mass under a wrench applied in one of the principal directions. We thus refer to $\mathbf{X}$ as the "*characteristic displacement matrix*". Let us first detail how $\mathbf{X}$ is computed, and then explain how its condition number correctly represents the quality of the behavior of the multi-axis force-torque sensor.

Let us consider that the structure has n degrees of freedom, where n is the number of generalized forces it is to measure, i.e., force and torque components. We also assume that the number of displacement sensors measuring the proof mass motion is m, which corresponds to the number of rows of $\mathbf{X}$. Let the i^{th} preselected point be equipped with a displacement sensor, and the j^{th} single axis force vector applied at a reference point of the suspended rigid mass. From Equation (3.3), the six-dimension vector $\mathbf{x}$ gives the point displacement and orientation of the rigid mass in the fixed reference frame $\mathscr{F}$. We then establish a transformation matrix $\mathbf{T}_i$ between the fixed reference frame and the auxiliary reference frame $\mathscr{M}_i$ attached to the i^{th} displacement sensor. From these definitions and Equation (3.3), the point displacement $\mathbf{x}_i$ seen by the corresponding displacement sensor under the action of wrench $\mathbf{w}$ becomes

$$\mathbf{x}_i = \mathbf{T}_i \mathbf{K}^{-1} \mathbf{w}, \tag{3.7}$$

where

$$\mathbf{T}_i = \begin{bmatrix} e^{\mathrm{cpm}(-\theta_i)}\mathrm{cpm}(\gamma_i) & e^{\mathrm{cpm}(-\theta_i)} \end{bmatrix}, \tag{3.8}$$

$\theta_i \in \mathbb{R}^3$ is the array of the products of natural invariants of the rotation taking frame $\mathscr{F}$ onto $\mathscr{M}_i$, and γ_i is the vector from the origin of $\mathscr{F}$ to that of $\mathscr{M}_i$. We then assume that each dis-

placement sensor is uniaxial, with its sensitive direction given in frame $\mathscr{M}_i$ by unit vector $\mathbf{e}_i$. The displacement measurement from the i^{th} sensor due to the j^{th} principal wrench can thus be expressed as

$$x_{i,j} = \mathbf{e}_i^T \mathbf{T}_i \mathbf{K}^{-1} \mathbf{w}_j. \tag{3.9}$$

With $x_{i,j}$ being now available, the characteristic displacement matrix $\mathbf{X}$ is obtained as

$$\mathbf{X} = \mathbf{E}^T \mathbf{K}^{-1} \mathbf{W}, \tag{3.10}$$

where $\mathbf{E} \equiv [\mathbf{T}_1^T \mathbf{e}_1 \ \cdots \ \mathbf{T}_1^m \mathbf{e}_m]$ and $\mathbf{W} \equiv [\mathbf{w}_1 \ \cdots \ \mathbf{w}_n]$ is the matrix of principal wrenches to be applied on the suspended mass. These principal wrenches generally correspond to the extreme values of the forces and moments that the multi-axis force-torque sensor is to measure.

The condition number represents the relative gain in all sensitive directions in response to external loads. We want to make this gain as even as possible in all directions, which calls for minimising the condition number. The objective function is therefore written as

$$\kappa = \|\mathbf{X}\| \|\mathbf{X}^{-1}\| = \frac{\sigma_{\max}(\mathbf{X})}{\sigma_{\min}(\mathbf{X})}, \tag{3.11}$$

where κ is the product of the matrix 2-norms. In order to evaluate the index between 0 and 1, we prefer to choose the objective

$$1 - \frac{1}{\kappa}, \tag{3.12}$$

which is to be minimised. Notice that this index corresponds to the relative gain variation, as it may be expressed as

$$1 - \frac{1}{\kappa} = \frac{\sigma_{\max} - \sigma_{\min}}{\sigma_{\max}}. \tag{3.13}$$

We use a standard iterative algorithm to optimize the dimensions of the compliant structure forming the multi-axis force-torque sensor. The analysis of the performance variations of an initial design allows iterative improvements. Having outlined the structural Optimization procedure, let us apply it to the design of a multi-axis force sensor in the following section.

3.4 Sensor Design

Figure 3.1 shows a prototype of the triaxial force sensor. The first step towards the design of this sensor consists in developing its associated symbolic mathematical model. Then, the resulting model is used to determine the optimum shape of the mechanical structure. The optimum structure is then validated numerically, using both the finite element method, and an experiment.

3.4.1 Mechanical Description

The novel structure of the proposed triaxial force sensor is a monolithic mechanical design. As shown in the schematic diagram of Figure 3.4, the mechanical structure we called "*OctaBeams*" consists of three main parts:

- A suspended rigid mass, working as a movable part and performing as the interface to the applied force.
- Eight square-sectioned horizontal beams arranged symmetrically, working as elastic springs to transduce the applied wrench into a displacement.
- A rigid base linked to the movable part through the compliant beams, and working as a sensor holder.

The eight beams are arranged such that they allow the movable part to resist twisting about the z-axis, which makes the compliant mechanism insensitive to moments about its axis of symmetry. The suspended mass is also stiff to translations in the x and y directions. Thus, the corresponding displacements are small compared to the z-displacement resulting from the rotation about the y and x axes. Consequently, the displacement of the central rigid body is measured only in the z-direction using four displacement sensors symmetrically located below the movable part. To make things clearer, the measuring principle is shown in Figure 3.5.

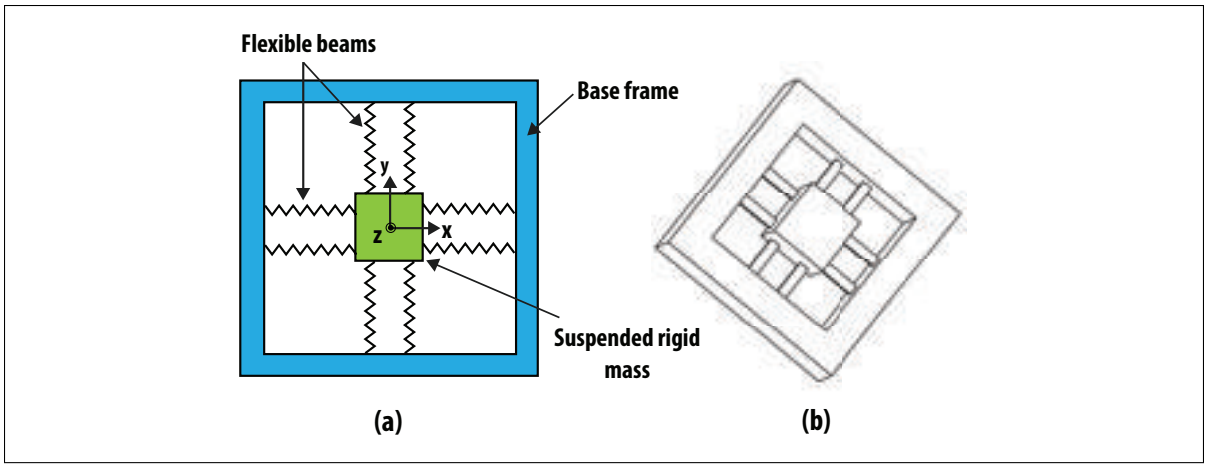

Figure 3.4 OctaBeams structure: (a) schematic view, (b) 3D isometric view

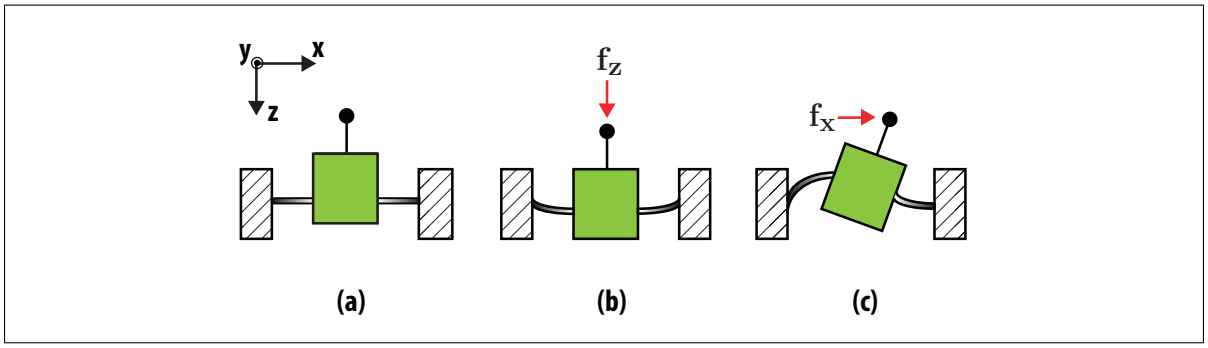

Figure 3.5 Working principle of OctaBeams structure: (a) under no applied force, (b) a normal force, and (c) a shear force

We have proved that the cross-axis sensitivity of the multi-axis force-torque sensor mainly depends on the deformation of the compliant structure. In fact, the input-output relationship allows to match the applied wrench with sensor displacements to reach a prescribed cross-axis sensitivity. This relationship can be modeled accurately, which allows the comprehensive and fast optimum design of the structure, over numerous design parameters. To be fully effective, this design method should take into account not only the mechanism geometry, but also the application-specific ranges of applied forces, the displacement ranges picked up by the capacitive sensors, and the material properties. Only then the displacement sensors can be used to

their full capacity and accuracy, and provide force estimates that are as accurate as possible. This design approach is outlined in the following subsection.

3.4.2 Modeling and optimization

First, the model presented in this section aims at determining the theoretical relationship between the wrench $\mathbf{W}$ applied to the moving mass and the corresponding measurements $\mathbf{X}$ picked up at the displacement sensors. The symbolic relationship is partially derived from Euler-Bernoulli beam theory:

$$\mathbf{X} = \mathbf{E}^T \mathbf{K}^{-1} \mathbf{W}, \tag{3.14}$$

where $\mathbf{E}^T \in \mathbb{R}^{4\times 6}$ transforms the rigid-mass displacements into displacements along the sensitive directions of each capacitive sensor, and $\mathbf{K} \in \mathbb{R}^{6\times 6}$ is the classical Cartesian stiffness matrix. As the calculation of these two matrices is too long to be included here, let us refer the reader to Cardou *et al.* (2008) for a complete account. Then, the *characteristic displacement matrix* $\mathbf{X} \in \mathbb{R}^{m\times 3}$ is simply computed, where $m = 4$ is the number of displacement sensors measuring the suspended-mass motion. Each column of this matrix represents the combination of displacement-sensor measurements corresponding to one of the three principal forces. In turn, the principal forces $\mathbf{W} \in \mathbb{R}^{6\times 3}$ are three forces directed along the x, y and z directions, with their magnitudes corresponding to the extreme values of the forces that the sensor is to measure.

The distance to isotropy can be computed using the performance index defined above, which was defined as a ratio of the matrix 2-norms of $\mathbf{X}$ evaluated between 0 and 1, namely,

$$1 - \frac{1}{\kappa} = \frac{\sigma_{\max} - \sigma_{\min}}{\sigma_{\max}}. \tag{3.15}$$

where κ, $\sigma_{\min}$, and $\sigma_{\max}$ are respectively the condition number and the minimum and maximum singular values of $\mathbf{X}$. Minimizing the performance index as a function of the dimensions of the

compliant mechanism forming the multi-axis force sensor results in an optimum shape, i.e., a structure with a good sensitivity in all directions, in response to external loads. However, as pointed out above, the design space can be limited by other application-specific design constraints, which we detail below.

The multi-axis force sensor application consists in measuring normal and shear stresses into an electromechanical active prosthetic socket for above-knee amputees. Since the amputation never occurs at the same place, conventional sockets are typically customized for each amputee. This uniqueness explain why there are almost no data available regarding the relationship between certain types of socket and the types of fatigue injury occurring at the interface. This reconfigurable and instrumented socket will be used in a clinical environment to evaluate the stress associated with various socket designs.

For this application the desired properties characterizing the multi-axis force sensor are as follows:

- The multi-axis force sensor fits in a cube of $20 \times 20 \times 14$ mm;
- The maximum applied forces are $f_x = 60$ N, $f_y = 60$ N and $f_z = 100$ N;
- The displacements along the z direction under the maximum applied forces range from 150 μm to 200 μm;
- The smallest milling tool diameter is 1/16";
- Delrin® is the material composing the structure;
- Four displacement sensors are positioned at the edges of the square with 6.2 mm edge length, centered at the origin and fixed to the bottom face of the movable part.

Having outlined the requirements of the sensor application, let us apply the design procedure to optimize the OctaBeams structure forming the sensor. The optimization problem can be expressed as follows: find the set of design parameters–thickness h of the beams, width w of

the beams, length l of the beams–that minimize the objective function given in Equation (3.15) and satisfy the desired characteristics of the sensor. Using the Matlab® optimization toolbox[3], the optimum design is obtained. The design parameter values are summarized in Table 3.1.

Table 3.1 Results of structural optimization

Parameter	Thickness h	Width w	Length l
Units	mm	mm	mm
Value	1.51	1.51	4.4

In order to validate the results of this optimum design process, which was based on a symbolic model of the multi-axis force sensor, a CAD model of the sensor structure is developed and a finite element analysis is performed (see Figure 3.6). When subjecting the structure to normal or shear forces, we obtained similar rigid-mass displacements with both the FEA and the symbolic model. Furthermore, a real prototype was built and tested. The displacements along the z-axis were measured using a high precision force-displacement gauge by applying nominal forces (the maximum applied axial forces) to the interface in the principal directions. To increase the measurement reliability, each force was tested twice with a short break between the experiments. A major problem with this experimental method is that the displacement along the z-axis is difficult to measure for the lateral forces. Following this, the results were compared in Table 3.2 against those provided by the symbolic model and those obtained from the CAD model. All results correspond to roughly similar values of displacements. This confirms the reliability of the theoretical model. Note that the performance index reaches a value of 0.27, corresponding to a condition number of 1.36. In other words, this means that the sensitivity of the sensor is relatively uniform across its different sensing directions.

[3]We resorted to constrained nonlinear optimization through the *fmincon* command, which in turn called the sequential quadratic programming routine of Matlab®.

Figure 3.6 Results of finite element analysis for: (a) normal force, (b) shear force

Table 3.2 Comparison between the displacements obtained from the symbolic model, the finite element model, and the real structure

Displacement in the z direction	fx	fy	fz	$1-\frac{1}{\kappa}$
symbolic model (mm)	0.150	0.150	0.191	0.27
finite element model (mm)	0.158	0.159	0.214	0.35
measured (mm)	NA	NA	0.213	NA

3.5 Displacement sensor based on capacitive sensing

Now that we have designed a compliant structure that will follow the desired behaviour, we must couple it to a proper displacement sensing technology.

3.5.1 Displacement sensing principle

In recent years, there has been considerable interest in exploiting the capacitance change for measuring different physical properties (Ulmen and Cutkosky, 2010; Gu *et al.*, 2004; Young *et al.*, 2004). The increasing availability of inexpensive and precise CDC converters can partially explain this popularity. However, capacitive sensing has also some advantages that make it a good candidate for being used in multi-axis force-torque sensors: *i)* with appropriate shielding, the sensor is insensitive to surrounding noise, *ii)* it can be made very compact, as a smaller

distance between two conductive plates increases the sensitivity, *iii)* it can be designed for non-contact measurements of displacement, and thus does not alter the structure stiffness and *iv)* the output is repeatable and follows an almost linear relation with displacement.

Given that we desire three-dimensional force sensing, a minimum of three displacement sensors is required. Besides, sensor redundancy is usually a simple solution to improve the performance of multi-axis force sensors. Therefore, four electrodes are used to measure the capacitance change associated with a distance change between two conductive plates. This configuration of the sensing element provides a biaxial symmetry which coincides with the x and y axes of the sensor. Thus, a proper fusion of these redundant information on the calibration provides a reliable estimate of the force due to the minimization of coupling errors. Furthermore, the capacitance variation Δc between the conductive plates of area A caused by a small variation of distance Δd can be roughly approximated by

$$\Delta c = \frac{\varepsilon_0 \varepsilon_r A}{\Delta d}, \tag{3.16}$$

where ε_0 and ε_r are respectively the electric and the dielectric constants. The displacement measurement concept is drawn from this last equation. As shown in Figure 3.7(a), our displacement sensing device consists of two rectangular conductive plates separated by a gap of air and silicone material. Preventing the dielectric from touching the top plate allows for a better sensor resolution without affecting the mechanical properties of the structure. The silicone substrate is not attached to the suspended mass, but rather to the PCB as it is manipulated more easily before assembly. The bottom plate is fixed to the sensor frame and composed of four electrodes, while the single top electrode is attached to the movable part. As shown in Figure 3.7(c), when a normal force is applied on the interface (the z direction of our sensor), the force compresses the parallel plates, resulting in increased capacitance variation of all sensors. In response to a shear force (the x or y directions on our sensor), the top plate rotates (as shown in Figure 3.7(d)) and the capacitance increases on two sensors and decreases of the two others. Moreover, the capacitance change remains insensitive to translation displacements of the top

plate since the area A taken into account into Equation (3.16) is always the smallest one, here the area of the electrodes.

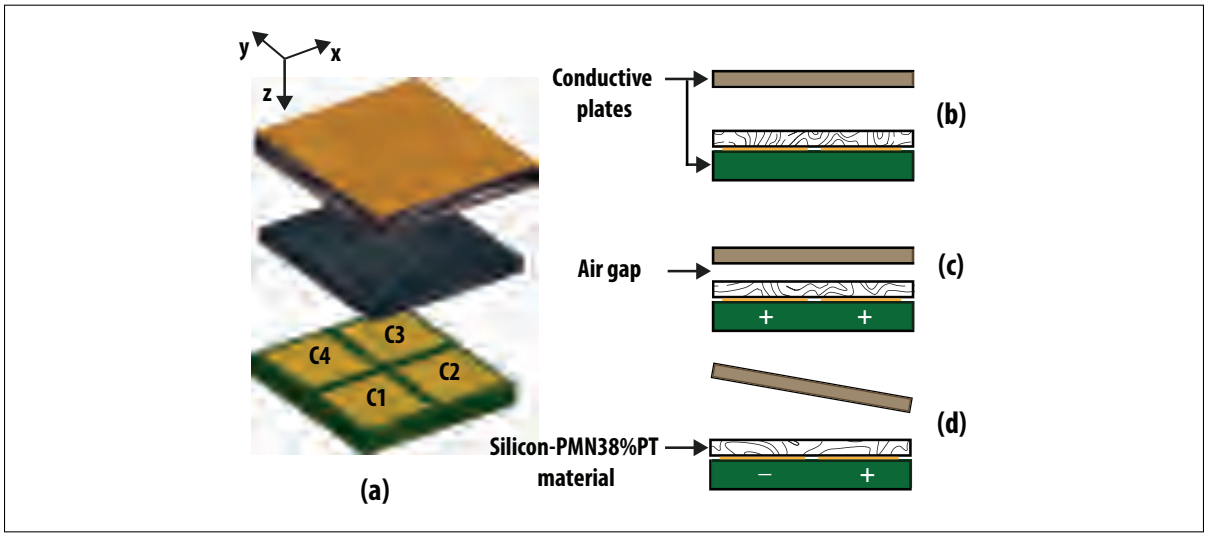

Figure 3.7 Capacitive measuring principle: (a) general view, (b) under no applied force, (c) normal force, and (d) shear force

3.5.2 Characterization of the dielectric

We know that capacitance is higher in capacitors made from dielectric materials with high permittivities, large plate areas, and small distances between the conductive plates. Since the size of the sensing device and the gap between the two plates are constrained by the overall desired sensor characteristics, the variables A and d of Equation (3.16), cannot be used to improve the sensitivity of the sensor to a given displacement. However, increasing the relative permittivity between our two conductive plates could greatly improve the response and thus give a better sensor resolution. In order to change this property we have created a soft dielectric filled with nanoparticles of a ferroelectric ceramic with a very high dielectric constant.

In order to see how the relative permittivity of our silicone (EcoFlex® 0030, Shore hardness 00-30) composite increases as the volume fraction of the nanoparticles increases, some experiments were performed. The first step consisted in mixing in a planetary mixer (Thinky

ARE-310) the silicone with the nanoparticles of lead magnesium niobate-lead titanate (PMN-PT), a ferroelectric ceramic with a dielectric constant soaring at $e_r = 12500$ (see Figure 3.8(a)). The doped silicone was then casted in a rectangular mold (Figure 3.8(b)). Subsequently, the doped silicone was degassed before the curing step (Figure 3.8(c)). Finally, the cured layer was unmolded (Figure 3.8(d)). Figure 3.9 shows the obtained soft dielectric.

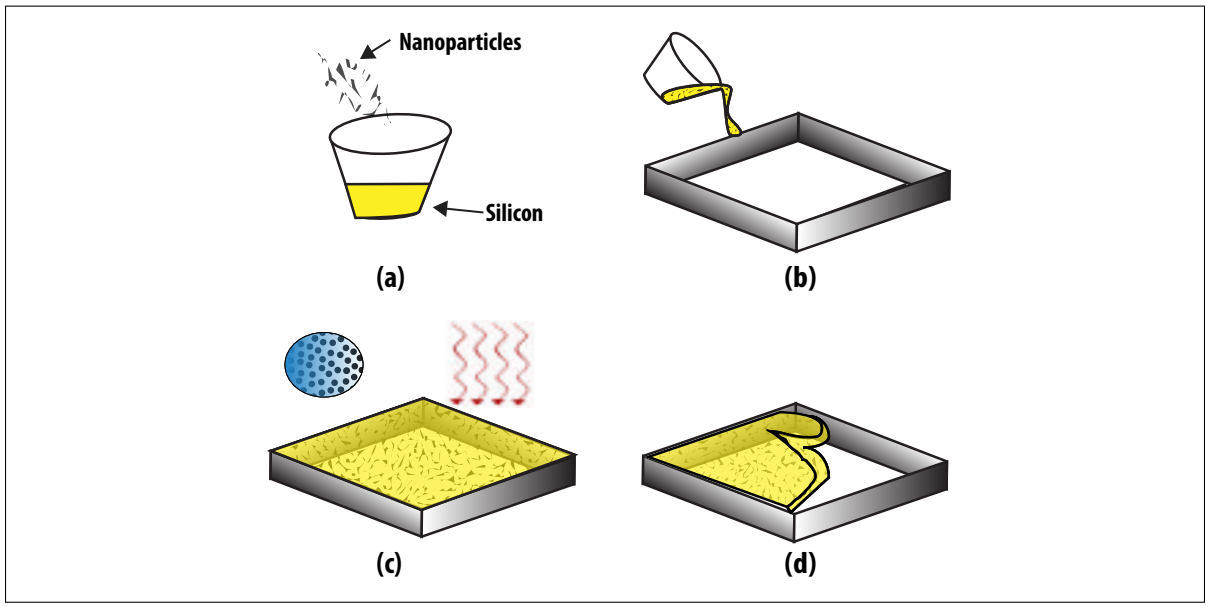

Figure 3.8 Dielectric casting procedure: (a) preparation of the composite, (b) casting, (c) vacuum degassing and curing (60 C° for 45 min), and (d) unmolding

The capacitance was measured using the capacitor measuring concept, where the rectangular shaped dielectric is positioned between two copper plates on a given area (same as the dielectric). An LCR-meter (B&K Precision 878B) was used to measure the resulting capacitance at 1 kHz. The dielectric constant can be easily estimated from Equation (3.16). Figure 3.10 shows the resulting curves of the relation between the volume fraction of particles contained in the silicone and the dielectric constant ε_r. Considering the very high permittivity of the ceramic particles used, the dielectric constant values obtained for our composites may seem very low. However, the resulting dielectric constant of a composite is not a simple function of the volume proportion between the polymer matrix and the filler. According to Cherney (2005); Carpi

Figure 3.9 Photograph of the dielectric

et al. (2011), this is because a single crystal of the ceramic particles does not have the same permittivity along all three axes. For example, a single crystal of PMN-PT has a permittivity of 12500, 100, and 100 along the a, b, and c axes. Since these particles are randomly aligned in the polymer matrix the resulting permittivity is low. Nevertheless, we can observe on this curve that the relative permittivity increase almost linearly as a function of the filler amount. Our final dielectric is composed of 26% by volume of PMN-PT as the silicone becomes friable above this fraction.

3.6 Sensor fabrication

The sensor components are designed such that they can be manufactured and assembled easily and at a low cost. The manufacturing time is approximately 180 min and the overall cost of this sensor is below $100. The manufacturing of the sensor prototype is performed in three steps. First, the mechanical parts are machined individually using a high precision three-axis CNC milling machine (MODELA MDX-40A, Roland) to achieve the desired dimensions. These parts include a top conductive plate made of copper sheet; a base and a compliant structure both made of Delrin® ; and a lid made of acrylic, all shown in Figure 3.11(a). While the CNC machining option is more expensive than other fabrication processes, it generally allows more

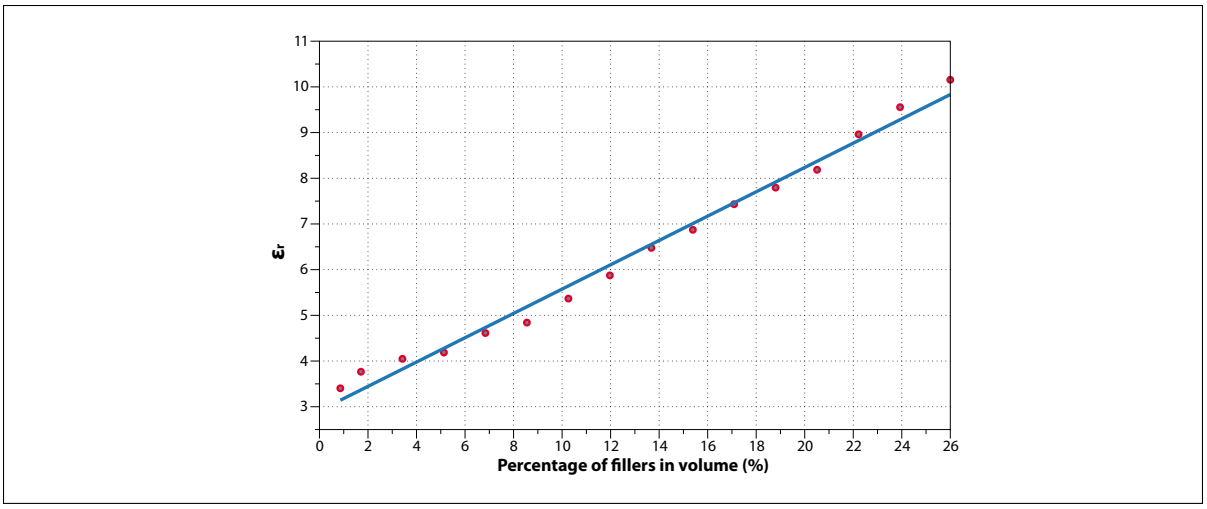

Figure 3.10 The relation between the percentage of nanoparticles contained in silicone and its dielectric constant

precise features. For example, Figure 3.11(b) shows a picture of the minimum feature size, which is the width of the beam in the structure. This picture was captured under a microscope using an image processing software. The machining error was measured to be less than 0.13%.

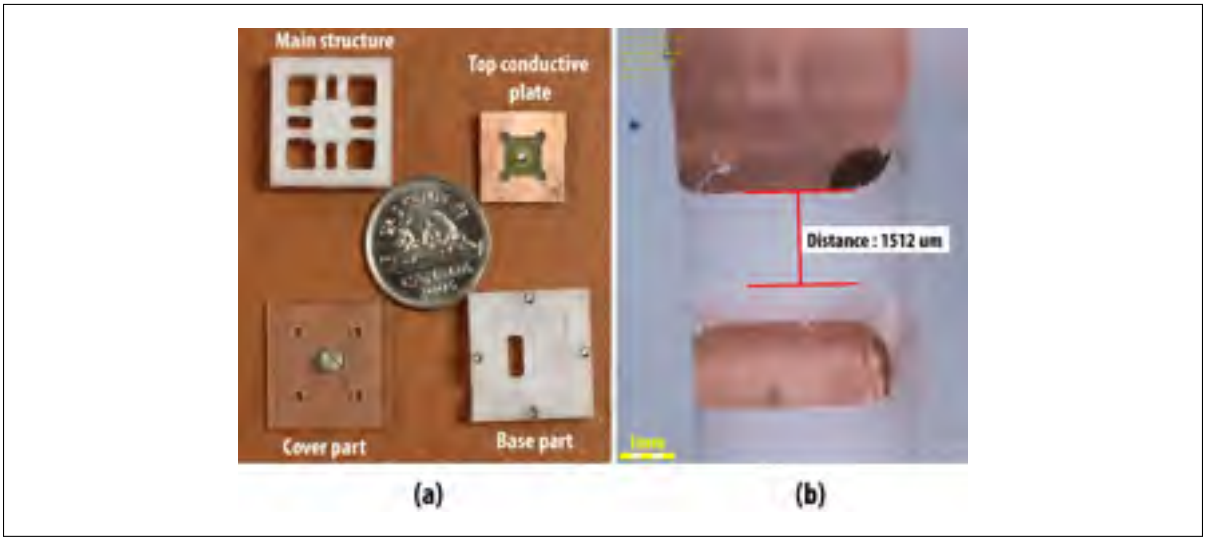

Figure 3.11 Triaxial force sensor parts: (a) mechanical parts before assembly, (b) beam feature after milling

Once the mechanical parts are manufactured, the sensing device was integrated into a custom conditioning circuit before final assembly. Indeed, the electrodes, indicated in Figure 3.12(a), are connected to a capacitive to digital converter, the Analog Devices AD7147, in order to have a digital signal count proportional to the capacitance variation. Compared to the other multi-axis force-torque sensors, the proposed sensing element takes advantage of commercial CDC chipsets, which are commonly used in applications such as touchscreen monitors and smart-phones. This simply ensures a cost-effective manufacturing and assembly solution. However, it should be noted that other solutions can be adopted for the same type of sensor such as the Cypress PSoC and other custom capacitance measurement techniques. In addition, the ASIC was then integrated to a PCB with four electrodes disposed on the top layer, as shown in Figure 3.12(b), which reduces the cost and increases reliability.

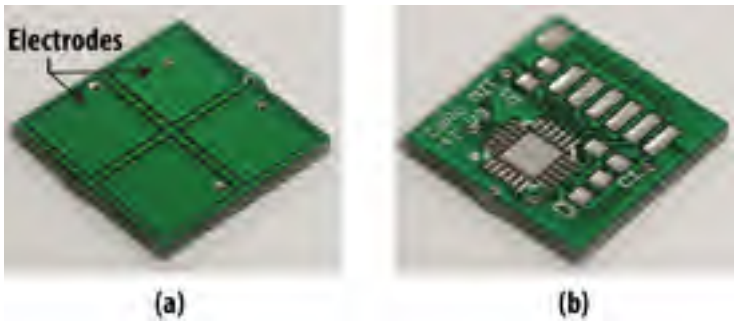

Figure 3.12 Embodiment of the sensing device in a PCB of four electrodes: (a) top layer, (b) bottom layer

Finally, we built a 3D model of the triaxial force sensor assembly. The manufactured parts, including the sensing device, are assembled as illustrated in Figure 3.13(a). The attachment of the sensing device can be summarized in two stages. First, the top conductive plate is glued onto the bottom face of the suspended mass. In the second stage, the PCB is simply fixed to the base. The packaged version of the sensor appears in Figure 3.13(b). The dimensions of the triaxial force sensor are 20 mm $\times$ 20 mm $\times$ 14 mm, after all the sensor parts were assembled.

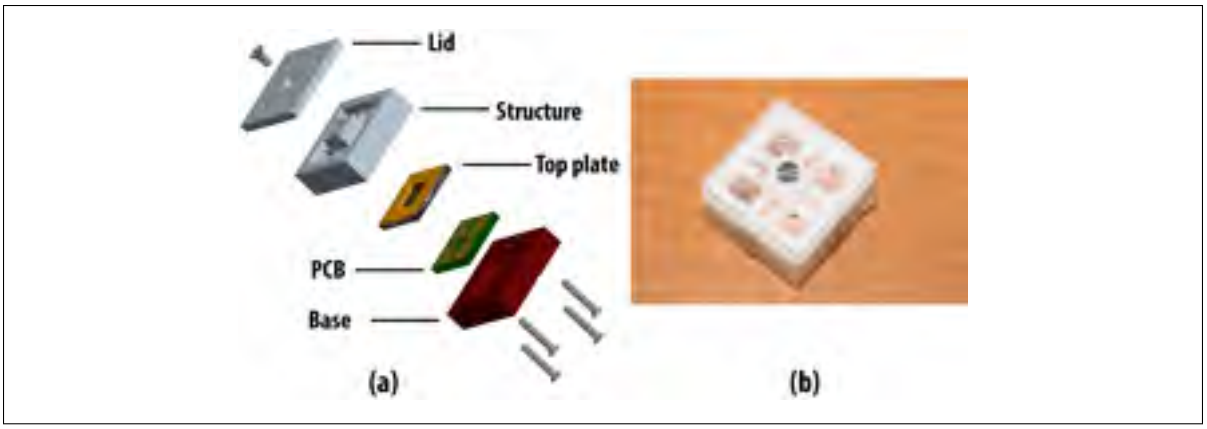

Figure 3.13 Prototype of the triaxial force sensor: (a) CAD-generated exploded view, (b) packaged sensor

3.7 Experimentation

In order to characterize the manufactured sensor, we used the experimental setup shown in Figure 3.14(a). This setup is composed of a force gauge (Mark® M4-10 which has a measurement range of 50 N and a resolution of 0.02 N); a triaxial force sensor; an SPI-RS232 card, and a PC with the Matlab® package installed. Computing the applied force from the displacement-sensor measurements using the electromechanical model would inevitably lead important errors. Hence, it is necessary to obtain an a-posteriori model of the sensor via a static calibration. This procedure consists in applying varying forces in the x, y, and z directions. The capacitance variation of each sensor is processed and converted by the ASIC into a digital signal. The sampled signals are then recorded using an 16-bit microcontroller (PIC16F887, Microchip's PIC® architecture) at 100 Hz. This lower sampling frequency is due to the conversion rate of the AD7147. Using a USB serial interface, the microcontroller sends signals of all four sensors to a PC with the Matlab® Guide program to read the data in real time. Figure 3.14(b) shows a schematic of the data-acquisition system.

Although the sensor has been designed to sense normal forces up to 100 N, here, we limited the calibration range to only 30 N because of the limited range of the force-gauge. By using the experimental set-up and the calibration procedure described above, the output values from each

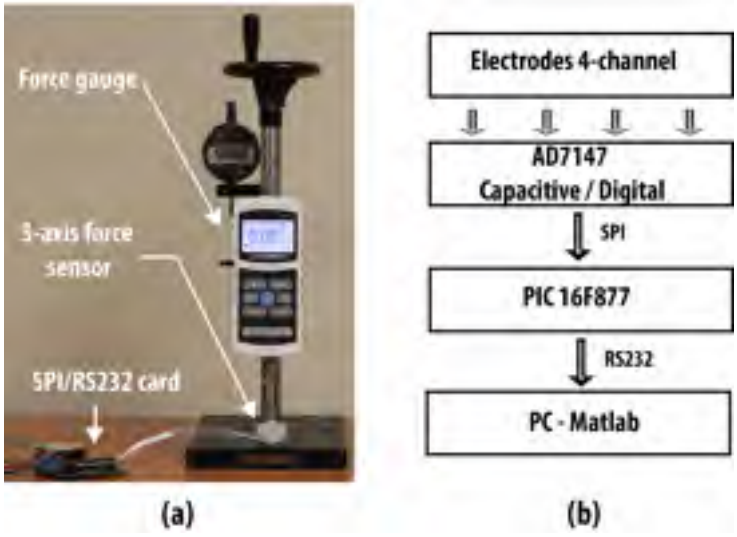

Figure 3.14 The calibration system for triaxial force sensor: (a) calibration set-up, (b) schematic diagram to read the signals

sensor were acquired. To increase the reliability of measures, for each applied force we used a mean value of the outputs. Because of space constraints, only two sample calibration graphs are shown in Figure 3.15, those of the applied forces f_x and f_z against the measured capacitance counts. We can infer from the ratio between the output signals that the cross-axis sensitivity of the sensor reaches approximately a value of 0.29, which means that the sensor behaves as required in the design specifications and as predicted by the symbolic model. One may also observe that the four output signals are significantly coupled. With proper calibration, however, it is possible to obtain a calibration law from which to reconstruct the three force components applied to the sensor. In order to obtain this calibration law, we fitted the relationship between the four output signals and the applied forces f_x, f_y and f_z with a multivariate second-order polynomial of the form

$$f = a_1 + \sum_{i=1}^{4}(a_{i+1} \cdot c_i) + \sum_{i=1}^{4}(\sum_{j=i}^{4}(a_{\sum_{k=1}^{i}(5-k)+j+1} \cdot c_i \cdot c_j)) \tag{3.17}$$

In order to preserve the slightly nonlinear trend of the relationship, we opted for a second-order polynomial instead of a linear fitting. The coefficients a_i of the calibration law were computed using the standard linear least-squares method. Since the objective of this study is to evaluate the performance of the triaxial force sensor, some experiments were performed using the calibration results. These experiments consisted in evaluating the static characteristics of the prototype such as its accuracy, the magnitude of interference errors, its resolution, and the signal drift. However, the following study does not take into account all performance specifications such as repeatability and dynamic analysis.

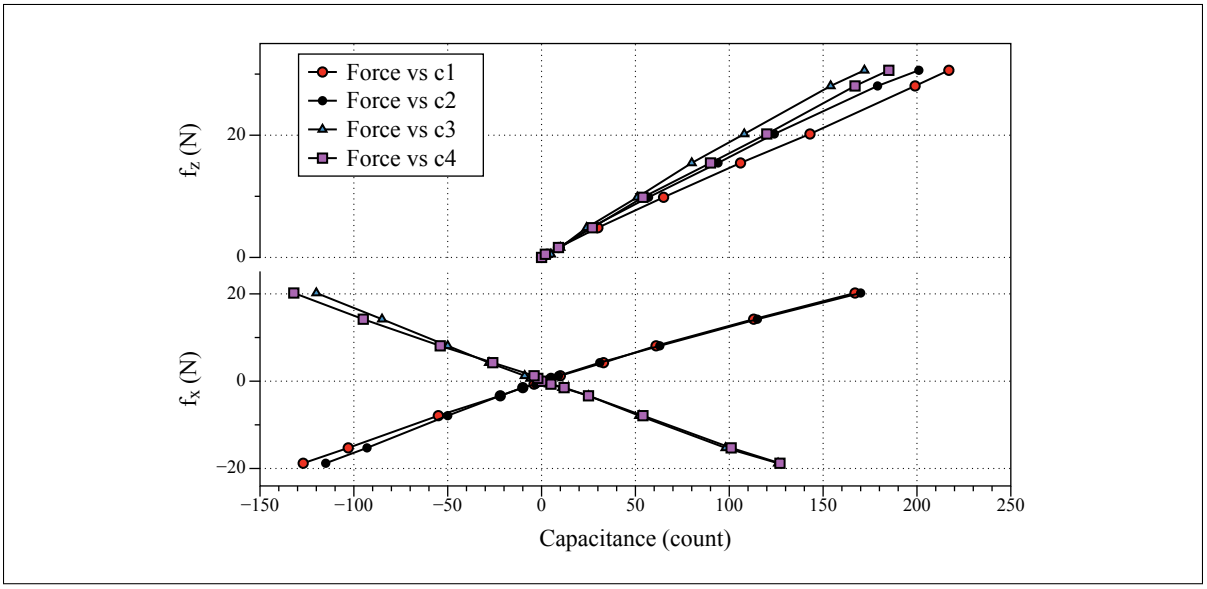

Figure 3.15 Calibration results of the triaxial force sensor

3.7.1 Analysis of accuracy

First, the calibration errors of this sensor were evaluated based on the calibration law obtained from the static calibration procedure. Here, we simply show in Figure 3.16, the difference between the measurement and the calibration law in the x-direction of force. The maximum absolute error in the principal directions was less than 0.62 N, or approximately 1.58% of the calibration range of the sensor. We conjecture that this error comes from the chosen calibration

law. Indeed, the capacitive sensors are not perfectly linear, as capacitance is inversely proportional to the distance between the two electrodes. This inverse law may cause the nonlinearity in the sensor response, which can be observed in Figure 3.16. Our nonlinear calibration law is able to capture this nonlinearity closely, but not perfectly.

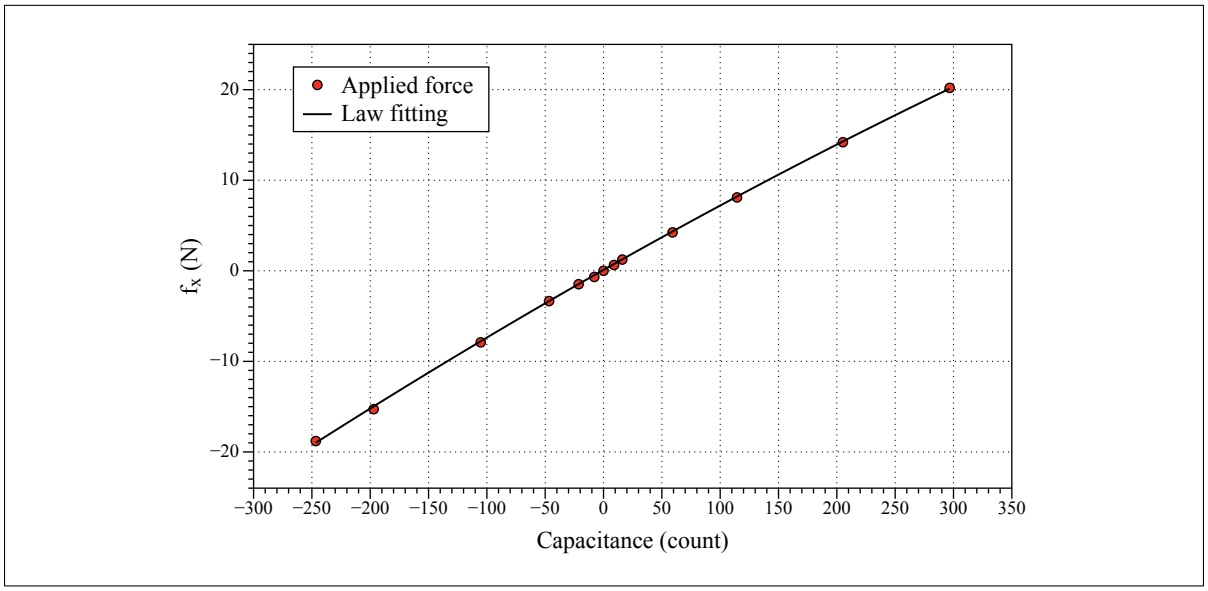

Figure 3.16 Graph of f_x data fitting

3.7.2 Analysis of coupling errors

Some tests on coupling effects have been performed. The test consists in computing the cross-axis sensitivity for the non-loaded directions when the maximum force is applied in one direction only. This experiment was repeated for all three sensitive directions. Table 3 summarizes the interference errors from the calibration laws for each principal direction. When the sensor was tested in x-direction, the cross-axis sensitivity for y and z directions were calculated respectively as 0.11% and 0.23%. The interference error in the y-direction is below 0.31%, while that of the z-direction is below 0.23%. The interference error between axes results from a combination of mounting errors, mechanical inaccuracies, and circuit crosstalk.

Table 3.3 Results of interference errors

Force	Max. load (N)	Interference errors (%)		
		x	y	z
f_x	20.20		0.11	0.23
f_y	19.60	0.31		0.07
f_z	30.62	0.23	0.11	

3.7.3 Analysis of resolution

In this experiment, a low-magnitude force of different directions was applied to the force sensor by loading a lightweight object. Here, only the resolution for the z direction is shown in Figure 3.17, as the purpose of the study is not to present a complete metrological characterization of the force sensor. Referring to Figure 3.17, although the level of noise can limit the resolution of the sensor, we can see that a force of 0.051 N can still be detected with some filtering. With regards to the obtained results, we can point out that the resolution is approximately the same in the different axes. This good resolution is due to our multi-layered dielectric composed of air and doped silicone. That is to say that the dielectric does not contribute to the stiffness of the compliant mechanism, which brings up the sensitivity and improves the sensor resolution.

3.7.4 Analysis of drift and hysteresis

In this last experiment, the hysteresis characteristic was evaluated using the load/unload method. The sensor was gradually loaded in the z-direction with forces ranging from 0 to 30 N. Then, the forces were gradually released. The measured forces were collected at each cycle. The result of this experiment for the z-axis appears in Figure 3.18. It shows that the sensor signal was repeatable with noticeable hysteresis. The hysteresis level rises with an increased applied force. The hysteresis is mainly due to the creep effect of the mechanical structure, which does not obey Hooke's law perfectly. A structure made from aluminum alloy could be associated with a low creep effect. Despite this, the level of hysteresis is considerably reduced by the

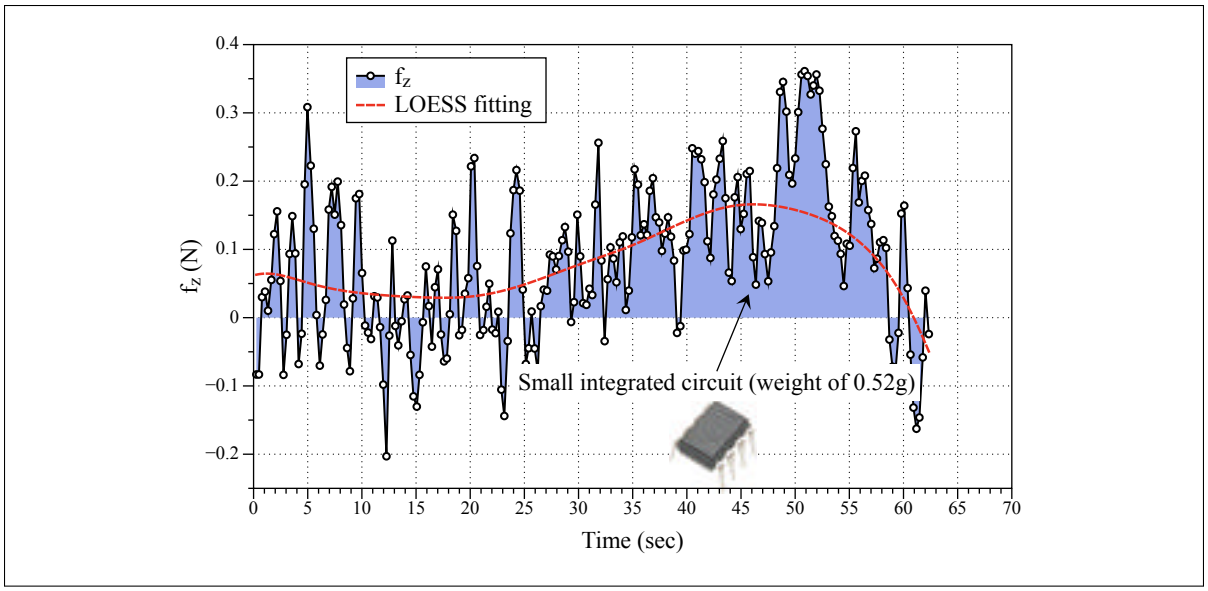

Figure 3.17 Measured force for a lightweight object

capacitive non-contact measurement method, which increases the precision and repeatability of the sensor.

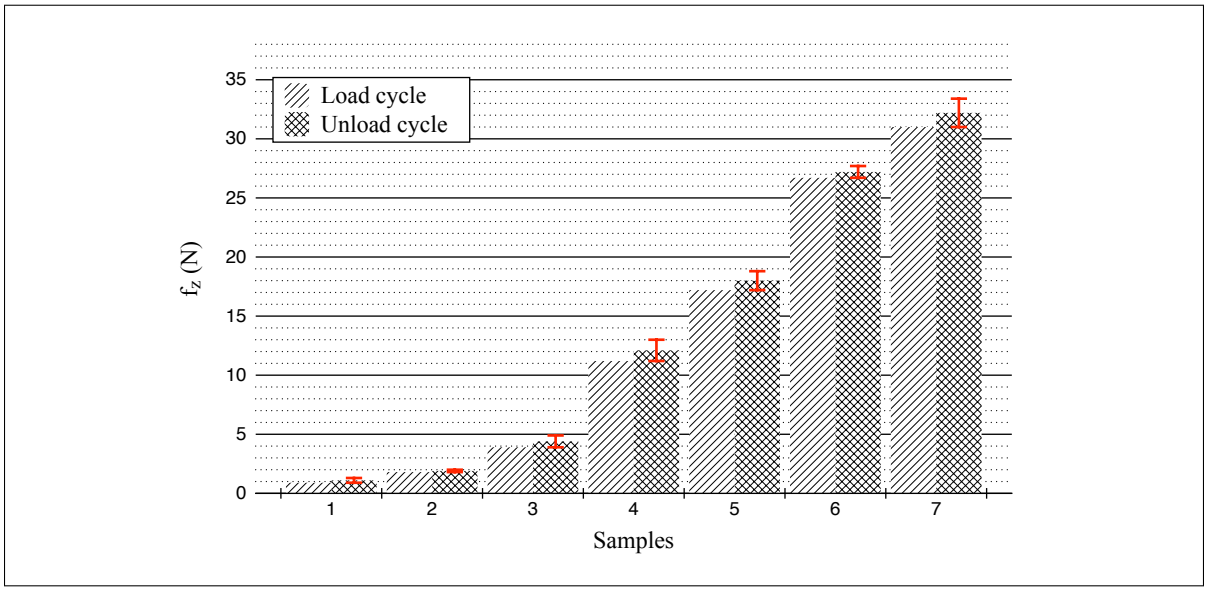

Figure 3.18 The hysteresis level in force estimates

The force signals can also be affected by the capacitive drift phenomenon, caused by temperature changes in the environment of the sensor. Many other internal or external factors may have an influence on signal drift, such as the stability of the sensing fixture. Here, the drift was quantified by recording force estimates for 10 min, as shown in Figure 3.19. We can see a slight deviation of the force signals, particularly in the z-direction. Also, it appears that the drift in the other sensitive axes is low, which is due to the biaxial symmetry of the sensing element. Nevertheless, in the future version of the sensor, the drift due to temperature will be compensated by adding a capacitance temperature sensor. Consequently, temperature fluctuations will be detected, canceling any random deviation of the signal, and avoiding recurrent recalibrations of the sensor.

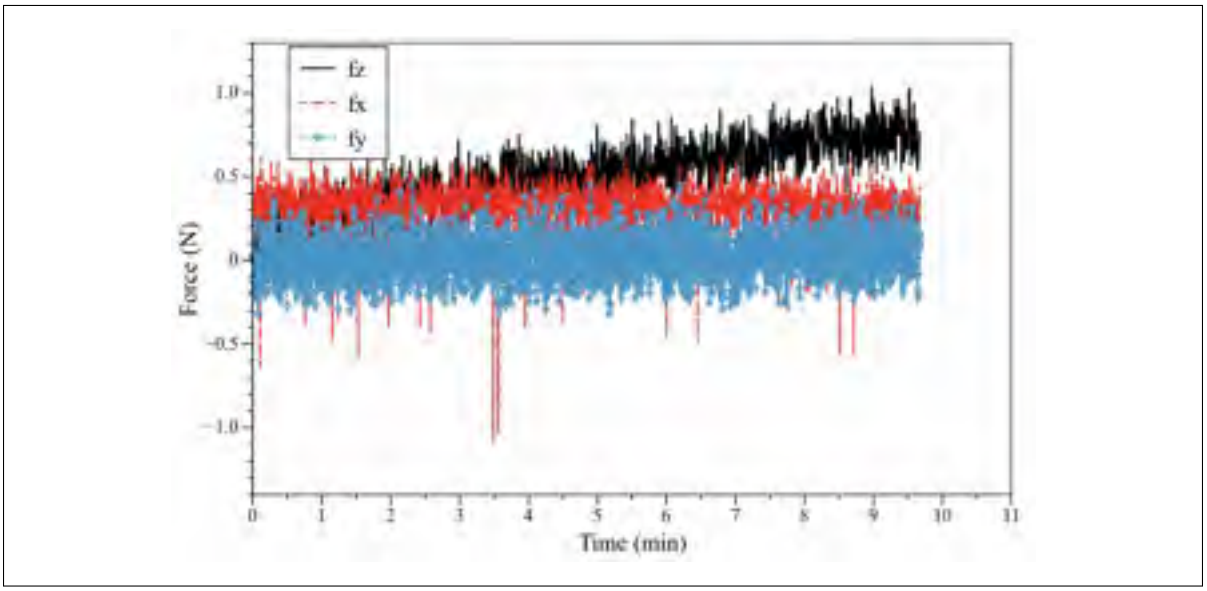

Figure 3.19 Force estimates during the ten minutes following power up

3.8 Conclusion

A new method for the mechanical design of the compliant structures of force-torque sensors was presented and validated in this paper. Using the symbolic relations between wrenches and displacements combined with the specifications of the application, a systematic design method

is formulated. This method can also be used for the design of accelerometer compliant structures and of compliant manipulators, provided that they undergo small displacements. Under the assumption that the compliant elements can be modeled as Euler-Bernoulli beams, the approach applies to any compliant structure, and allows a symbolic formulation of the wrench-displacement relationship. Since fabrication limitations are defined before the optimisation procedure, the force-torque sensor can easily be manufactured. Finally, when the displacement sensor is contactless, this optimisation method does not require any prior information on its properties.

This chapter has also described the design, modeling, fabrication, and characterization of a novel three-axial force sensor. The sensor presented here has four main advantages. First, the sensor is compact, which eases its integration into larger designs. Second, the calibration results show that the sensor has a good overall accuracy and low coupling errors. Third, the characterization of the sensor shows that the sensor can measure forces within a large range with acceptable cross-axis sensitivity and resolution. Finally, the experimental tests clearly illustrate that the capacitive displacement technology used in the sensor lead to good robustness against drift and hysteresis phenomena.

CHAPTER 4

A NEW TRANSDUCTION TECHNIQUE BASED ON STRESS IMAGING ANALYSIS

4.1 Introduction

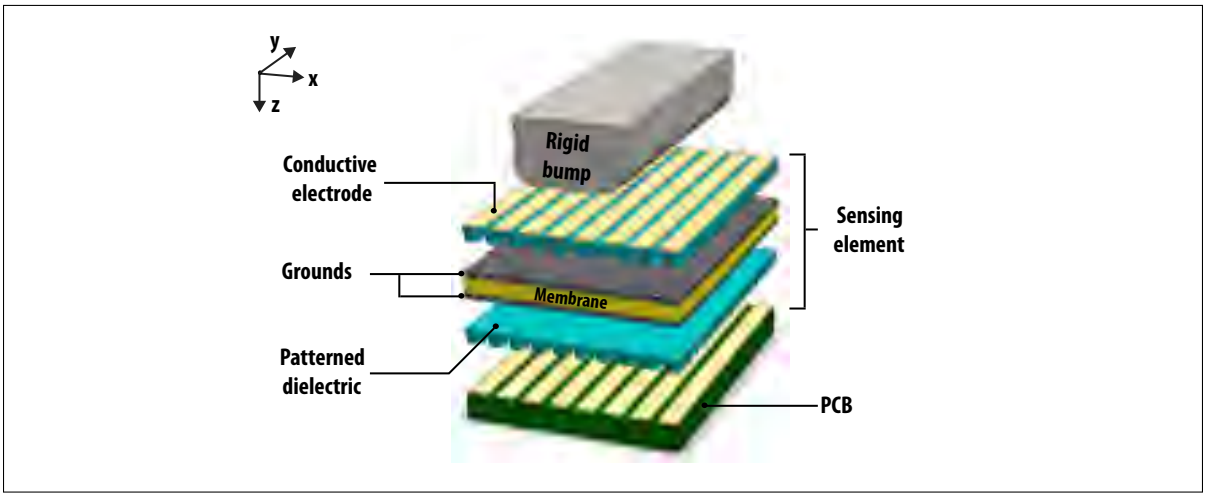

Figure 4.1 Layered structure of our triaxial sensing element

Past researchers have generally examined the mechanical aspects of sensor design, rather than the efficiency of the sensing element itself, and so attempts to improve the performance of such sensors have mainly focused on structural optimization. Indeed, the deformation of the compliant body has already been analyzed numerous times for the measurement of a six-component force. Uchiama *et al.* (1991) showed that using a systematic design procedure to minimize the conditioning of the strain compliance matrix does improve the performance of the sensor. In addition, Bicchi (1992) studied the effects of the condition number on the sensor accuracy. Finally, Ranganath *et al.* (2004b) have designed and analyzed a Stewart-platform based multi-axis force-torque sensor in a near-singular configuration. A list of related research can be found in Chapter 1.

However, the dominance of the mechanism-based approach has recently given way to efforts to improve the design of the sensing elements. We have previously developed a small triax-

ial force sensor that is based on a simple and efficient capacitive sensing system (see Chapter 3). Our sensor, which demonstrated accurate (absolute error is less then 1.58 of the calibration range of the sensor) shear and normal force detection, used a monolithic sensing element instead of the uni-axial sensing elements that are typically scattered throughout the core of the sensor. Several studies have also investigated alternatives to piezo-resistive technology (Brookhuis *et al.*, 2013; Takahashi *et al.*, 2003), but much work remains to be done in the quest for an optimally compact, cost-effective, and accurate force-sensing technology.

The majority of commercially-available sensing elements are uni-axial, requiring multiple sensing elements in order to reconstruct all the applied forces. The multitude of sensing elements introduces a great deal of complexity to the sensor fabrication. This is because the sensing elements are each designed to measure the stress from one specific direction, so they must each be placed in the sensor in a specific location, with perfect accuracy, during assembly. The need for multiple sensing elements also increases the size and weight of the multi-axis force-torque sensor, and possibly its fragility as well.

We believe this problem can best be resolved by combining multiple uni-axial sensing elements to create one multi-axial sensing element. Rather than using the analog signals acquired from several uni-axial sensing elements to directly calculate the force components, we will reconstruct the force by combining the stress images that are detected by our unified sensing element. This process requires us to develop a sensing element for multi-axial stress extraction that can easily be embedded in the structure of the multi-axis force-torque sensor.

To date, only a few multi-axis force-torque sensors have been produced that are based on multi-axial sensing elements. The earliest approach to their design used a capacitance-based sensing array (Liu *et al.*, 2008) to infer normal and shear stress. This involved embedding planar circuits of aligned electrodes into different polymer materials. A capacitive sensing array has the advantage of being planar in form, meaning its structure is relatively simple. However, the array must be produced using microfabrication techniques that require specialized equipment. More recently, Yussof *et al.* (2010) have developed a triaxial tactile sensor using a charge-coupled

device (CCD) camera. Image processing techniques are used to calculate normal and shear stress, respectively, from the integrated grayscale values (of normal stress) and the movement of the centroid (of shear stress). This non-contact measurement solution is promising for applications requiring large deformation, but it also requires bulky and expensive signal-processing equipment.

One of the major problems with the existing multi-axial sensing elements is their inability to distinguish between shear stress and torque. Most shear stress-sensing elements generate a torque in order to compress the deformable sensing layer. The underlying principle of operation of these sensing elements thus means that a torque stress is detected as pure shear. We address this problem by developing a completely new sensing element that will extract all the components of a stress that is applied at a given location. To determine each individual force component, the stress components on the sensing element are measured using electrode arrays that cover both sides of a flexible membrane. The presence of these two layers of sensitive electrode arrays significantly reduces the coupling errors, making this design especially suitable for six-component sensing elements.

Unlike previous efforts, our sensing method is capable of measuring information as stress distribution. This allows us to reduce the size of the network of sensing elements, and consequently lowers the total dimensions and cost of the multi-axis force-torque sensor. There are also several advantages to our method of using stress-imaging analysis to reconstruct the applied force. The rectangular structure of our design makes it easy to manufacture, as opposed to more complex designs such as cylindrical sensing elements. It is also robust and compact, making it more cost-effective. This is achieved without any tradeoffs regarding sensitivity, as the sensitive layers have a high capacitance. Finally, this method can be easily applied to a variety of systems, including artificial skin and robotic grips.

4.2 Basic idea

Our design is inspired by the tale of the princess and the pea, in which the heroine must prove that she is a true princess by noticing that a pea has been placed under the pile of mattresses on which she sleeps. Figure 4.2 shows that when the pea is under all the mattresses, the incident stress is diffused by the mattresses onto the reverse surface, allowing the princess to sense the pea even from her position at the top of the mattress pile. Since stresses are induced in all the layers, it follows that both the level and distribution of these stresses are influenced by the mechanical properties of the mattresses. In other words, the princess feels a higher stress diffusion with a lower intensity when she is on top of all the mattresses. By comparison, if only one mattress separated the princess from the pea, she would feel that the stress is more concentrated with a higher intensity.

Our sensing element is composed of a multi-layered polymeric structure made from silicone and conductive electrodes. Figure 4.3 depicts a schematic of the preliminary conceptual design of our multi-axial sensing element. The design is based on a composite structure of sensitive and passive layers. The basic structure is similar to that of most tactile sensors (Dahiya and Valle, 2013), but tactile sensors typically measure the stress distribution in one plane only, whereas the sensor presented here includes an additional sensing plane so as to capture stress distribution over two levels. This is why our device features a silicone layer, which is covered by a 2D array of capacitors on both sides.

Similarly, when a mechanical interface comes into contact with the top layer of the sensing element, the result is that the incident stress is diffused by the structure (see Figure 4.3). Since the outer sensitive layers have a lower stiffness than the inner passive layer, the collapse of the outer layers causes variations in the gaps of multiple closely-spaced electrodes, resulting in a local increase of capacitance. The change in capacitance is distributed in a bell-like shape and can be regarded as discrete two-dimensional stress images. The stress images are then analyzed using image processing algorithms, allowing us to reconstruct the applied force.

Figure 4.2 The princess and the pea. Note how the pea induces stress on the mattresses that becomes less concentrated as more mattresses are added

Figure 4.3(a)-(c) illustrates the principle for sensing normal, shear and torque stresses. When a normal force is applied to the sensing surface, it compresses both of the sensitive layers, resulting in both layers having increased capacitance with perfectly symmetrical distribution. When shear force is applied, it causes the orientation of the diffused stress to vary, resulting in skewed distributions. Thus the centroid of the bottom stress image is relatively non-centralized. The horizontal movements of the centroid are proportional to the lateral components of the applied wrench. With torque, some regions of the sensitive layers are compressed, while others expand, in accordance with the rotation angles of the object in contact with the surface. The

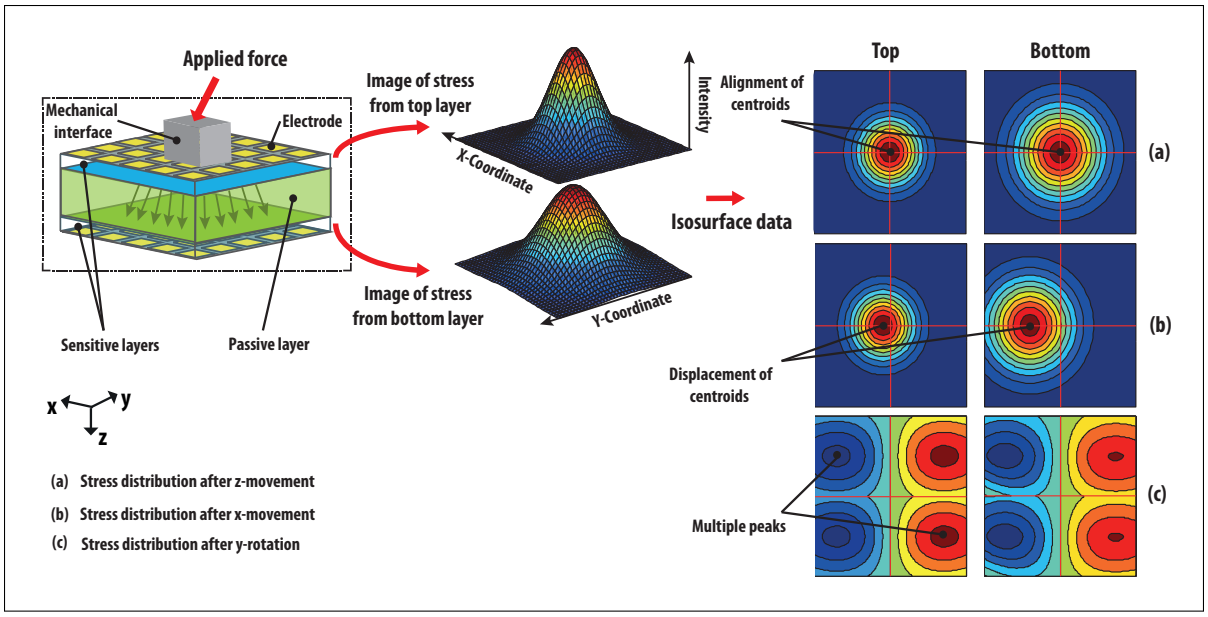

Figure 4.3 Principle of operation of the sensing element

resulting capacitance has a quadrimodal distribution. The components of the torque can thus be detected by analyzing the local capacitance changes of the four peaks.

4.3 Design

In this section, we discuss how our sensing method can be applied to the design of a triaxial sensing element, and further explain the concept for detecting normal stress, shear stress and torque. We also use the finite element method to validate our assumptions of the sensing principle.

4.3.1 Design description

Fig 4.1 shows the construction of the proposed triaxial sensing element. Its key components are:

- A rigid bump that acts as a mechanical interface between the applied force and the sensing element.

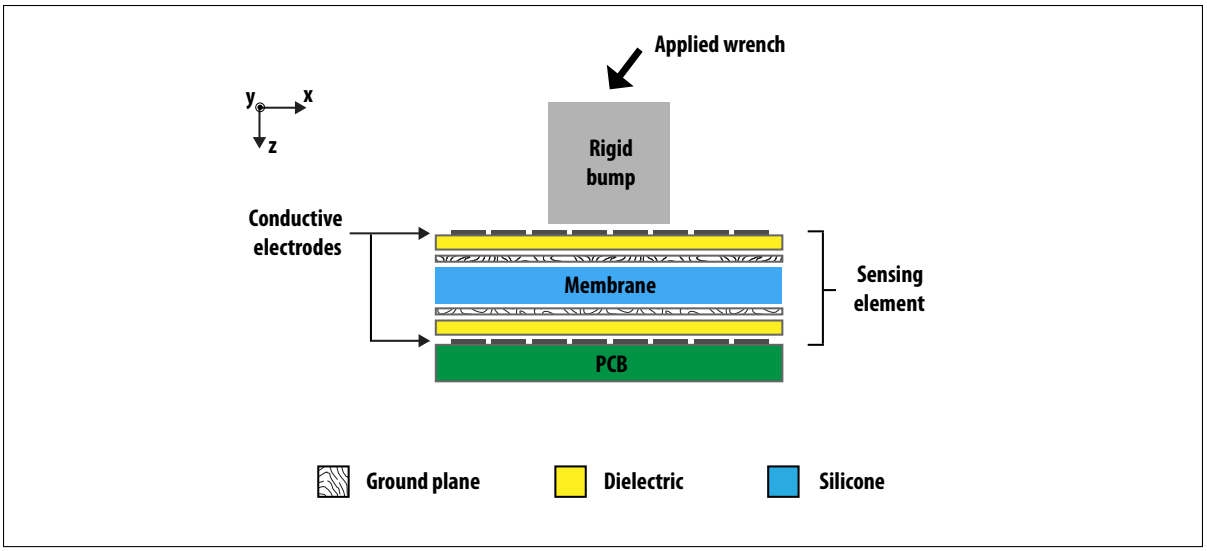

Figure 4.4 Schematic design of the triaxial sensing element

- A sensing element that converts its reaction to the stress (applied to it by the bump) into a measurable electric signal via capacitive transduction.
- An electronic circuit that is linked to the sensing element in order to measure the collected data and transmit it to the computer.

Fig 4.4 shows a cross-sectional view of the configuration of the triaxial sensing element. The sensing element has two stress-sensitive layers that are separated by a passive layer of silicone material. The sensitive layers are composed of multiple electrodes that are arranged to form sixteen separate sensors (also called capacitors). Eight of the sensors are adhered to the top side of the passive silicone layer, hereafter referred to as S-Top, while the eight others are adhered to the bottom side of the passive silicone layer, hereafter referred to as S-Bottom. Each of these sensors measures displacement in one direction only. For ease of fabrication, the sensors are distributed uni-axially, and aligned parallel to the center of the silicone layer. This allows the sensors to provide information regarding the distribution of stress on both sides of the silicone layer in the x direction. The stress distribution images are then used to infer the forces along the x and z directions, and the moment about the y axis.

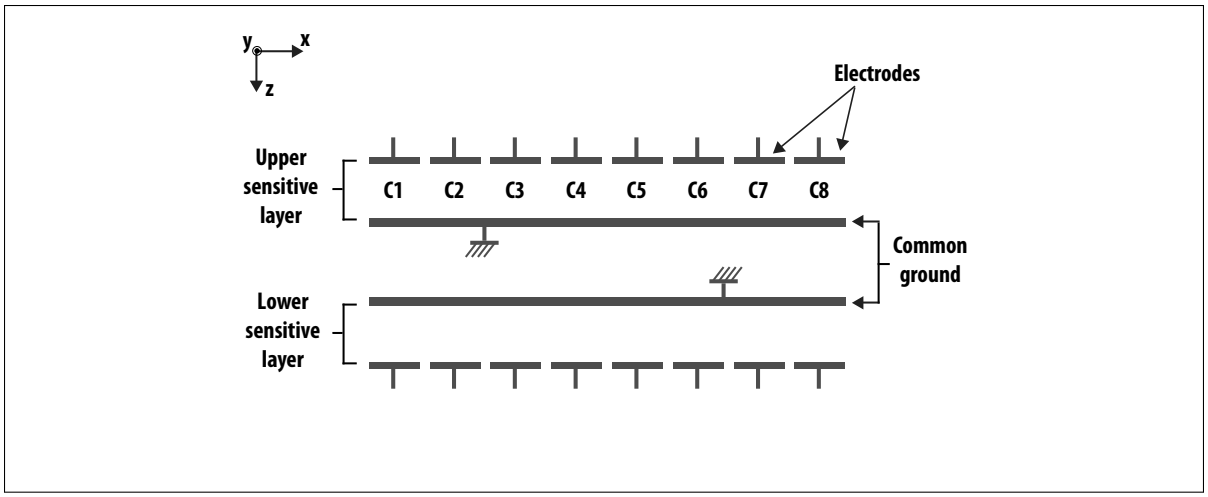

Figure 4.5 Network of the capacitive sensors

For each of the sensitive layers, eight electrodes are attached to one side, and one large electrode, which acts as the common ground, covers the other side completely. This design is shown in Figure 4.5. S-Top's electrodes were fabricated individually, whereas the electrodes of S-Bottom were integrated within one layer of PCB so they could all be attached at once. This was done to simplify the capacitive read-out.

As the eight electrodes of S-Top and both of the ground electrodes are all composed of conductive fabric (80 μm thick), we expect them to be highly flexible and to provide maximum sensitivity to local stress. The eight electrodes are separated from the ground electrodes by a dielectric that acts as an array of springs. The compressible dielectric increases the general capacitance levels under stress variations, and also provides an accurate portrayal of the stress distributions.

4.3.2 Mechanical characterization

The next step is to extract the magnitude and direction of the three-dimensional external wrench (the planar force-moment system) to which the bump is exposed. The sensing element detects changes in stress for any applied force. The sensitive layers, which are depicted as yellow

layers in Figure 4.6, each bear the induced stresses and capture a uni-dimensional stress image. Together, the two stress images are sufficient to determine three force-moment components.

Several assumptions were made about the design:

- We assume that the sensing element remains in constant contact with the rigid bump. Although this may be done through a number of methods, the technique we have chosen is to apply a prestress, so that sliding friction is prevented by sufficiently prestressing the sensing element in the initial condition.
- We treat the multi-layered structure of the sensing element as a monolithic elastic body, which simplifies the electromechanical model of the sensor.
- We regard the relationship between stress intensity and applied force as linear, and the deformation of the sensing element as reversible.

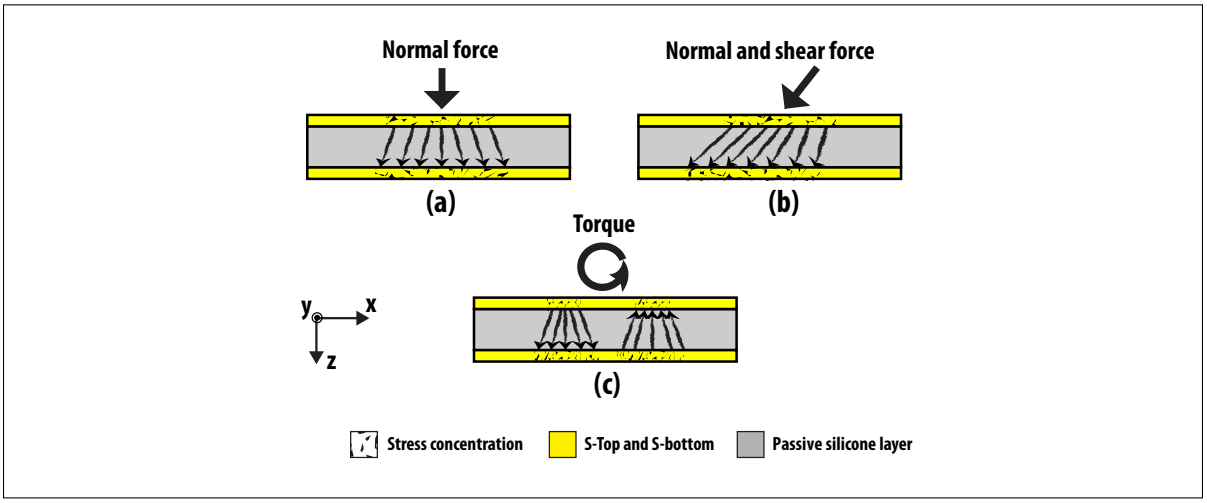

Figure 4.6 Principle of measurement by the triaxial sensing element

The combined action of the normal and shear force is shown in Figure 4.6(b) and Figure 4.7. Here, the internal deformation caused by the contact between the bump and the sensing element is the result of the stress components in both the z and x directions. Because the sensors

are deformed only in z, the deflection caused by shear stress cannot be measured directly. Nevertheless, the shear force influences the location of the centroid of the distribution of stress on the bottom surface of the passive layer. Note that the term centroid refers to the maximum value of a one-dimensional region, here characterized by the stress distribution.

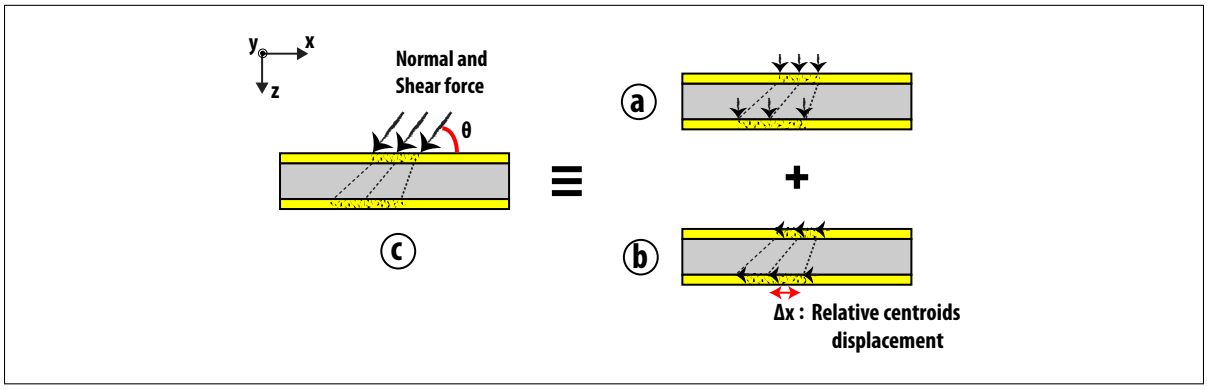

Figure 4.7 Sensing the combined normal and shear stress. (a) Combined; (b) normal stress alone; and (c) shear stress alone

Developing an analytical model for the sensing element is highly complex, as the model is nonlinear and subject to various constraints. However, finite element analysis can be used to validate our ideas. To this end, we must examine the relationship between the misalignment of the locations of the centroids, and the direction of loading on the sensing element. The z-displacements data are computed instead of the stress values data, so as to prevent the skewing of the simulation results due to local increases of stress. Here, the centroid is defined as the projection of the maximum value of the z-displacement vector onto the x-coordinates.

The mechanical behavior of the silicone layer is represented by a computer-aided design (CAD) model of a flexible membrane, which is based on the geometry of the sensing element. The membrane in our device is made of silicone rubber, which is a hyperelastic material. Since it is time-consuming to simulate the behavior of nonlinear materials, we consider the material to be linear and isotropic. We set Young's modulus to 2900 MPa and Poisson's ratio to 0.3. Based on the mesh model, we used finite element software (SolidWorks) to evaluate both the stress

distribution, and the displacements (with respect to the applied force) along the z-direction of both sides of the membrane. A major source of uncertainty in this simulation is that the mechanical properties of the dielectric and the fabric of the electrodes were not included in the model, so the simulation results include errors that do not occur when using the real device. In conducting the simulation study, we were not attempting to model the prototype as faithfully as possible; we simply aimed to validate the working principle of the sensing element.

In this simulation, a constant force of 2 N was applied at different angles ($\theta = 90°$ and $\theta = 45°$) to the top side of the membrane, with partial constraint on the bottom side as well. Clearly this simulation is not comprehensive, but it is sufficient for examining the impact of shear force. The color gradient in Figure 4.8(a)-(b) displays the stress intensity under the applied forces, and Figures 4.9 and 4.10 present the corresponding displacement measurements along the z-direction for both of the cases that we simulated.

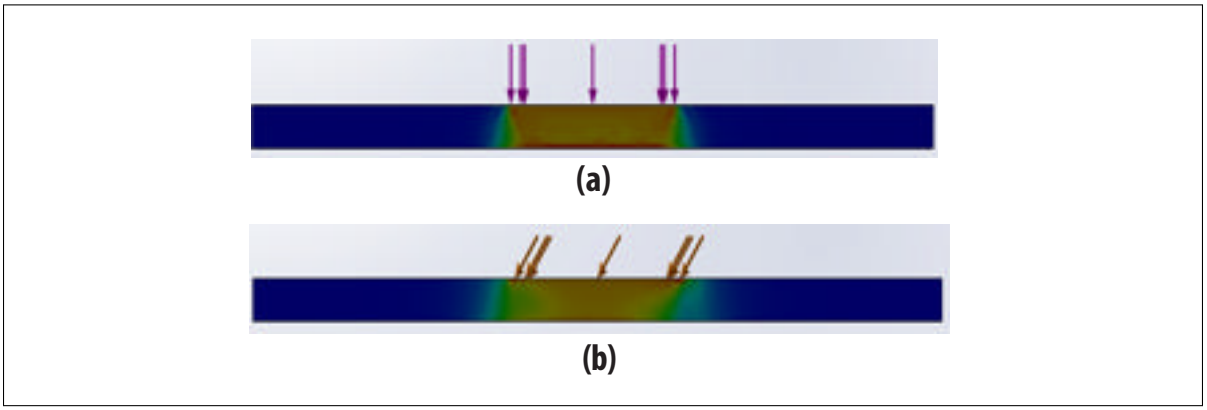

Figure 4.8 Stress intensity resulting from a force applied at two different angles. (a) $\theta = 90°$; (b) $\theta = 45°$

Figure 4.9 displays the simulation for the response of the device to normal force. The simulation shows that the membrane deforms as expected for normal force, and the results are reasonably similar to our initial assumptions. Indeed, as can be seen from Figure 4.9, the centroids of the two sides of the membrane are aligned for the normal force. This means that $\Delta x \approx 0$, as Δx represents the relative change in centroid locations. The orthogonal force is

concentrated on the center of the membrane, resulting in a centered unimodal distribution of the compressive stress (see Figure 4.8(a)).

This simulation allows us to predict several aspects of the behavior of the actual device: the dielectric gap will be reduced in proportion to the applied force, the capacitance of all the sensors will increase, and the capacitances will increase at unequal rates due to the geometry of the bump. Moreover, the simulation indicates that the deformation will induce symmetric stress distributions (stress images) on both sides of the passive layer, which will continue to be aligned with the centroids. According to these data, we can determine the normal force by measuring the magnitude of capacitance at either S-Top or S-Bottom.

Figure 4.10 shows the simulation for the response of the device to the combination of normal and shear force, which for our sensor denotes forces applied in the z and x directions. The application of both normal and shear force causes the bottom centroid to undergo a displacement along the horizontal plane. This displacement confirms our assumption that shear stress causes asymmetric changes in stress intensity (see Figure 4.8(b)). Consequently, the centroids are misaligned, such that $\Delta x \neq 0$. This in-plane displacement of the locations of the centroids is measured by comparing the stress images that have been captured from each side of the passive layer.

We hypothesize that the effect of the pure shear upon the magnitude of the stress in the sensitive layers will be negligible; we believe the pure shear will only influence the stress distribution over the location of the centroids, whereas the magnitude of the stress in the sensitive layers will depend solely on the normal force.

In response to a torque, the force will rotate the bump, increase the variation in capacitance of half of the sensors at S-Top and S-Bottom, and decrease the variation in capacitance of the four remaining sensors on each side. Figure 4.6(c) illustrates this effect. The angle of rotation, and the applied moment, M_y, are calculated by measuring the difference in capacitance between the two stress peaks. The capacitance values therefore allow us to reconstruct the applied force using the stress images.

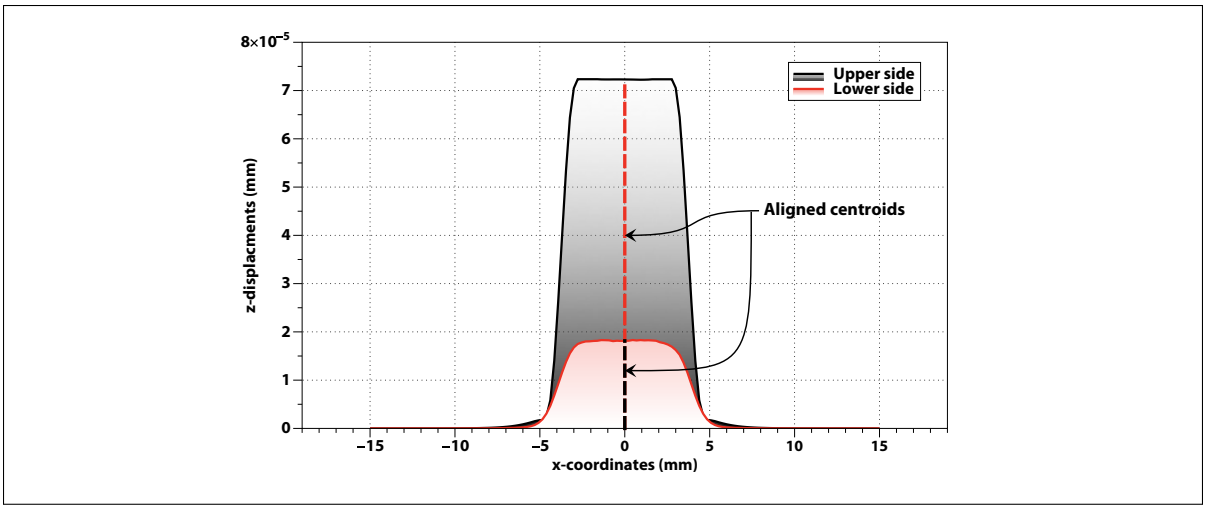

Figure 4.9 Displacement measurements resulting from an applied force ($\theta = 90°$)

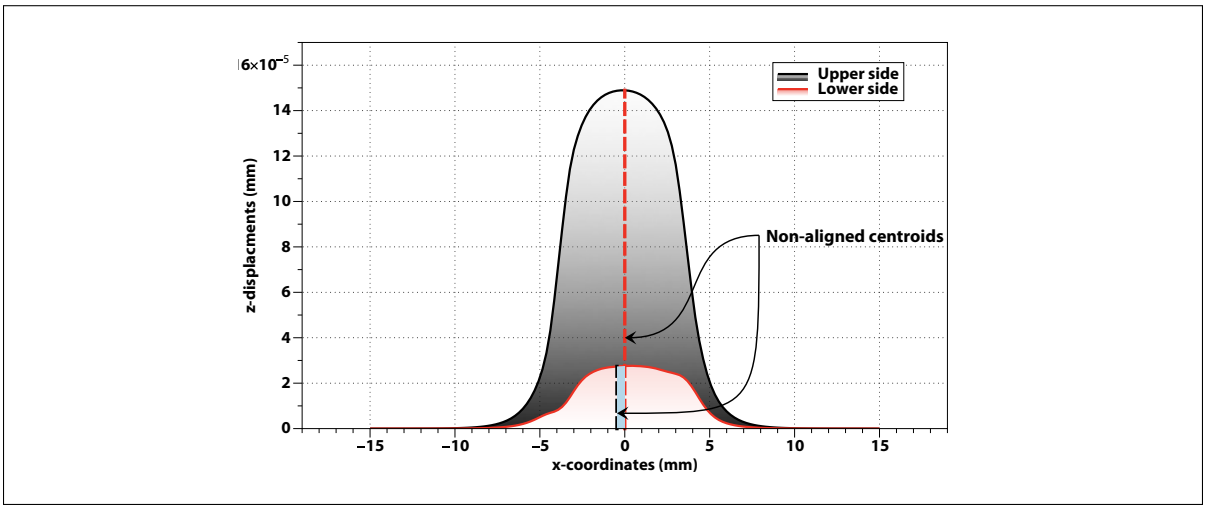

Figure 4.10 Displacement measurements resulting from an applied force ($\theta = 45°$)

4.4 Fabrication

This section is subdivided into two parts, the first of which presents the method of fabricating the sensing element. Following this, in the second part we describe the software system of the sensing element, and show how the output data are processed.

4.4.1 Hardware design

We manufactured a prototype of the sensing element for use as a proof of concept. The main components of the sensing element were fabricated using layered fabrication techniques and elastomeric materials. Layered fabrication allows the design to be customized, and does not require much assembly. However, the use of this technique alone does not guarantee that the sensing element will still be reliable after several cycles of stress transfer. We addressed this by using a silicone composite (EcoFlex, Shore hardness 00-30, from Smooth-On, Inc.) as the structural material for the different layers. This material is inexpensive and widely available. The silicone composite also possesses several characteristics that make it excellent for use in polymer-based capacitive sensing applications: 1) it features remarkable mechanical properties, as it may be deformed without plastic deformation over a large-scale stress range; 2) the deformation of the silicone composite is repeatable and follows a near-linear relationship; and 3) it has negligible creep and hysteresis.

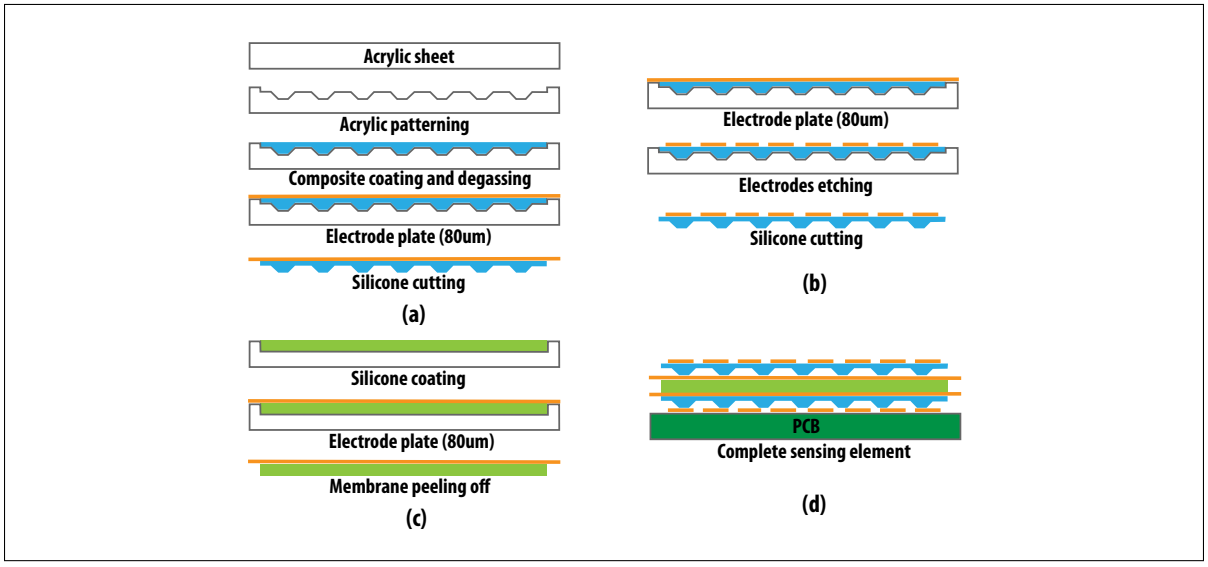

Figure 4.11 Process of fabricating the sensing element (simplified for ease of visualization)

Figure 4.11(a)-(d) illustrates the process of fabricating the three layers, which were processed separately before being bonded together with silicone glue. We will begin by describing the fabrication of the lower sensitive layer (i.e., the one that was adhered to the bottom of the passive layer).

The first step was to construct a mold for the microstructured dielectric. We used a CO2 laser-cutter (Epilog Helix 24 Laser) to etch our mold design into an acrylic sheet. There is some evidence that the shape of the pattern may affect the deformation of the sensing element, so the mold was etched as shown in Figure 4.12 to form a design that allows for local deformation. Following this step, nanoparticles of lead magnesium niobate-lead titanate (PMN-PT) were gently mixed with a silicone composite in a planetary mixer (Thinky ARE-310) at room temperature.

The PMN-PT nanoparticles are a ferroelectric ceramic with a dielectric constant of e_r = 12500. The relatively high dielectric constant of these nanoparticles thus increases the overall dielectric constant of the sensitive layers. For further details of the proportion of the nanoparticles contained in the silicone, and the dielectric constant in this experiment, please see Chapter 3.

After mixing, the silicone-nanoparticle mixture was poured into the mold and degassed to remove air bubbles. We added the ground electrode by placing a sheet of flexible metal fabric, 80 μm thick, over the surface of the uncured silicone mixture. The mixture was cured by being placed in a convection oven at 60 °C for 45 min, during which time the metal fabric bonded to the silicone mixture. We waited for the entire mold to cool to room temperature before peeling the layer out of the mold. We estimate the thickness of the layer to be 850 μm, a measure that was obtained using image processing software. Note that at this stage the layer is not yet sensitive, as the PCB containing the other eight electrodes was not added until after the other layers were fabricated.

The process of fabricating the upper sensitive layer was the same as what was described above for the lower sensitive layer (Figure 4.11(b)), except that the electrodes were formed by patterning the fabric with a DPSS laser (Samurai UV Laser at 355 nm). Low-power UV lasers take

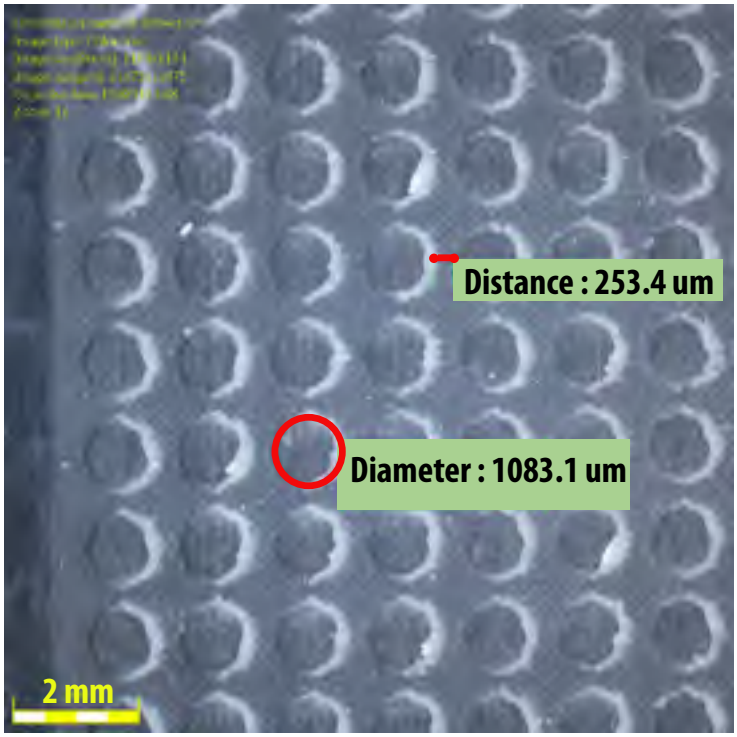

Figure 4.12 Mold made from acrylic sheet

advantage of the cold marking process, which ensures high-quality engraving. The electrodes are 29 mm long and 1.5 mm wide, with 500 µm pitch.

The mold for the passive middle layer was fabricated using another acrylic sheet etched with the CO2 laser (Figure 4.11(c)). After the silicone composite was poured into the mold, the ground electrode of the upper sensitive layer was adhered to the top side of the passive layer using the same curing process that we described for the lower layer. The resulting passive layer, including the ground electrode, is 950 µm thick.

Once all the layers had been fabricated, we painted the layers with curable glue, bonded them together, and added the PCB to the bottom of the lower sensitive layer (Figure 4.11(d)). Figure 4.13 depicts the three layers, before the PCB has been added. The final sensing element shows good flexibility. No photos were taken of the final sensing element because it is difficult to capture a clear close-up image of the deflected sensing element when it includes the PCB.

Figure 4.14 depicts a cross-sectional view of the sensing element's three-layer structure. This image was captured under a microscope using image processing software.

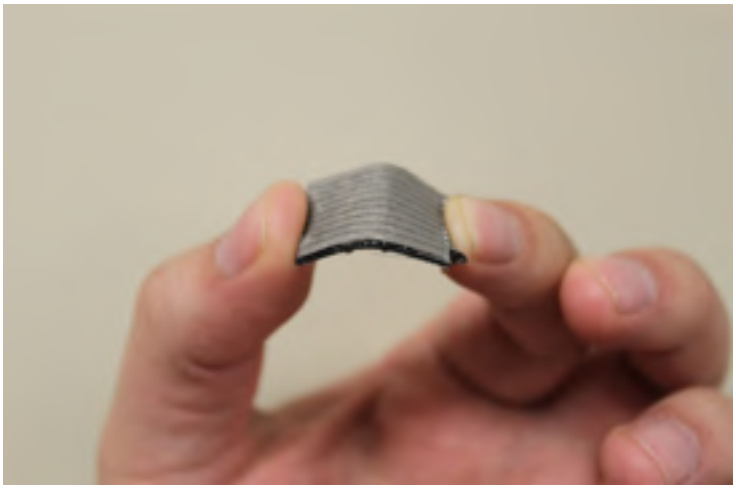

Figure 4.13 Fabricated layers of the sensing element, before the PCB was added

4.4.2 Software design

To acquire data from the arrays of electrodes, an electronic circuit was implemented on the underside of the custom PCB (i.e., the side of the PCB without electrodes). The sixteen identical electrodes and the two ground electrodes were sequentially connected to a capacitance-to-digital converter (CDC) from Cypress Semiconductors. This CDC uses a delta-sigma modulator to provide a digital signal count that is proportional to the capacitance variation, and it has a nominal resolution down to 0.1 pF. We reduced the noise by using a sensor layout that minimizes the distance of tracks from the electrodes to the CDC. In addition, the electrodes were spaced with equal-sized gaps between them, to prevent coupling between the different capacitors. The data from the PCB were transmitted via serial communication to a PC computer, on which the MATLAB GUI was running. Figure 4.15 illustrates a schematic of the readout circuit that was used to capture the stress images.

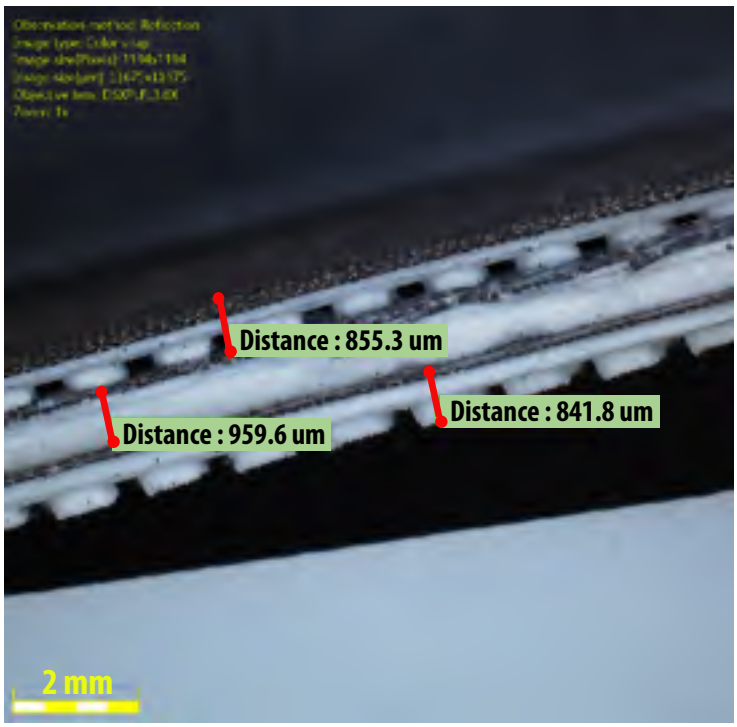

Figure 4.14 Cross-sectional view of the sensing element (not including the PCB)

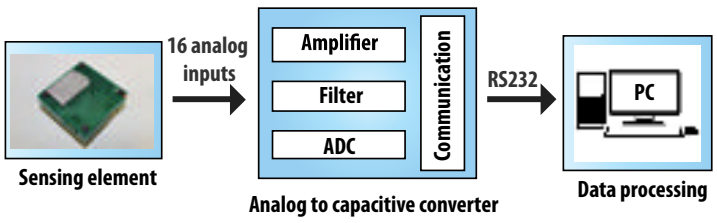

Figure 4.15 Schematic of the readout circuit

4.5 Sensing experiments

A simple experiment was conducted with the sensing element prototype, in order to validate the functionality of the proposed sensing method. In this section we will show how the calibration law, which relates the changes in capacitance to the two-dimensional applied force, was used in our experiment, followed by a discussion of our results.

4.5.1 Measurement setup

Here we describe the setup of the experiment that was used to characterize the manufactured sensing element. The experiment used a custom-made rotation stage that was mounted to a uniaxial force gauge. Figure 4.16 depicts the force gauge, which has a load capacity of 50 N and precision equivalent to 0.02 N. We used the rotation stage to hold the sensing element, and to fix the loading direction within a range of about 45° around the y-axis. However, this range turned out to be irrelevant, as we subsequently found that the sensing element structure can only support loading directions within a range of up to 15° about the y-axis without measurement errors. We used a protractor to measure the angle at which the force was applied. Our knowledge of the force-application angle helped us to decompose the applied force into the two separate components of normal force and shear force.

The sensing element was plugged into the rotation stage and connected to the data acquisition system. The changes in capacitance, resulting from stress applied to the sensing element, could thus be read as digital counts. The signals from the sixteen sensors were recorded by our data acquisition system, which used the MATLAB graphical user interface (GUI) shown in Figure 4.16. The recorded signals about capacitance counts were then processed by interpolating the corresponding signals using MATLAB software. This allowed us to see real-time stress images of S-Top and S-Bottom during the test.

4.5.2 Characterization of the sensing element

Having set up the experiment, we must now characterize the sensing element in order to demonstrate the feasibility of decoupling normal and shear forces. In this chapter, we focused on obtaining normal and shear forces, even though we developed a triaxial sensing element. This is because these are the most difficult forces to obtain, so after they have been found the torque will be obvious. We used a probe tip, fixed to the force gauge at one end, to apply a centered force over the sensing element's surface. As in the simulation, a pre-load was required in order to prevent the contact surface from slipping while shear forces were applied. As the purpose

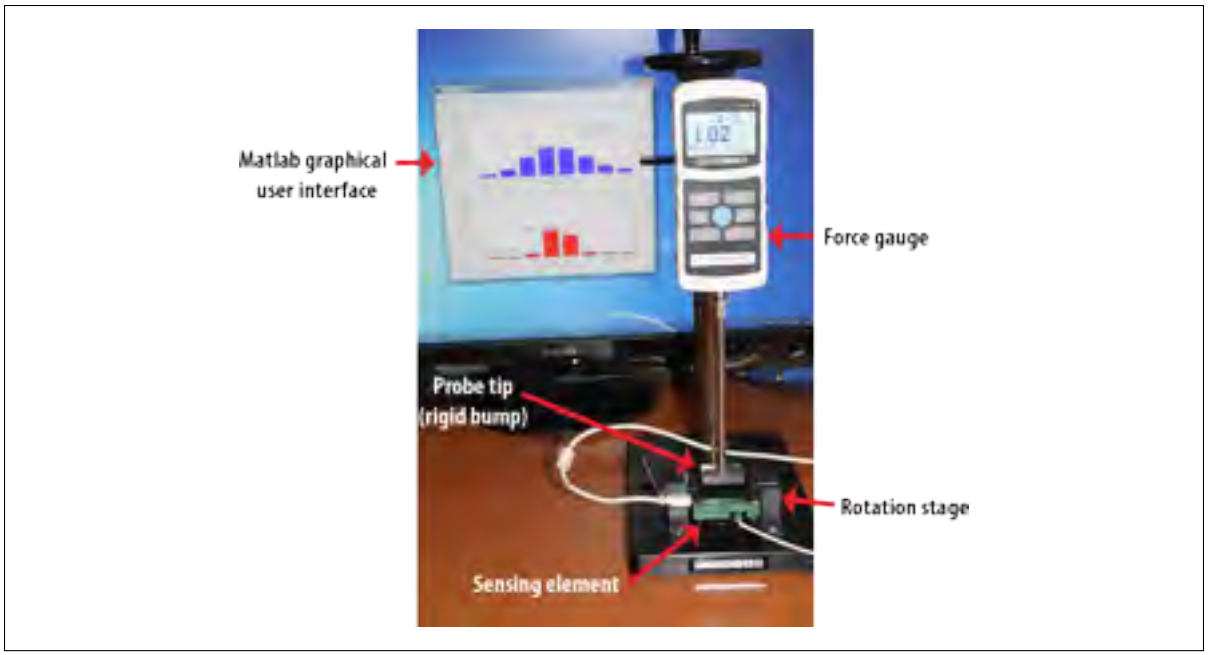

Figure 4.16 Measurement setup

of this study is not to present the full calibration of the sensing element, only one test was conducted, in order to collect data from one normal force response in the $+z$-axis and several shear force responses in the $+x$-axis. First, the sensing element was mounted horizontally for normal force (f_z), i.e., $\theta = 90°$. We restricted the magnitude of the applied force to about 2 N to protect the sensor from damage. Then, we gradually increased the force in the $+x$-axis by rotating the sensing element clockwise along the y-axis until it reached an angle of 82.5°. Sixteen capacitance measurements were acquired for each loading direction. The measured signals are normalized by their initial values because the sensors have different offset values.

4.5.3 Results and discussion

Due to the large amount of data we collected, we focus on the three scenarios that are best suited for validation. These are shown in Figures 4.17 to 4.19. The first case only provided stress images when the sensing element was loaded with a vertical force. We found that both of the sensitive layers compressed evenly, and the capacitance of S-Top and S-Bottom increased

exponentially. The centroids were slightly misaligned, as can be seen from Figure 4.17. Thus, the parameter Δx_{exp} has an initial value of -265 counts, which can be considered as a baseline. This misalignment may be due to the precision, or lack thereof, with which we assembled the sensor. These errors may have stemmed from any aspect of the setup, such as the sensing element, or the measurement equipment. Note that the values of Δx_{exp} correspond to a basis vector (10000 points) used to interpolate the data and their corresponding values specified by the number of sensors.

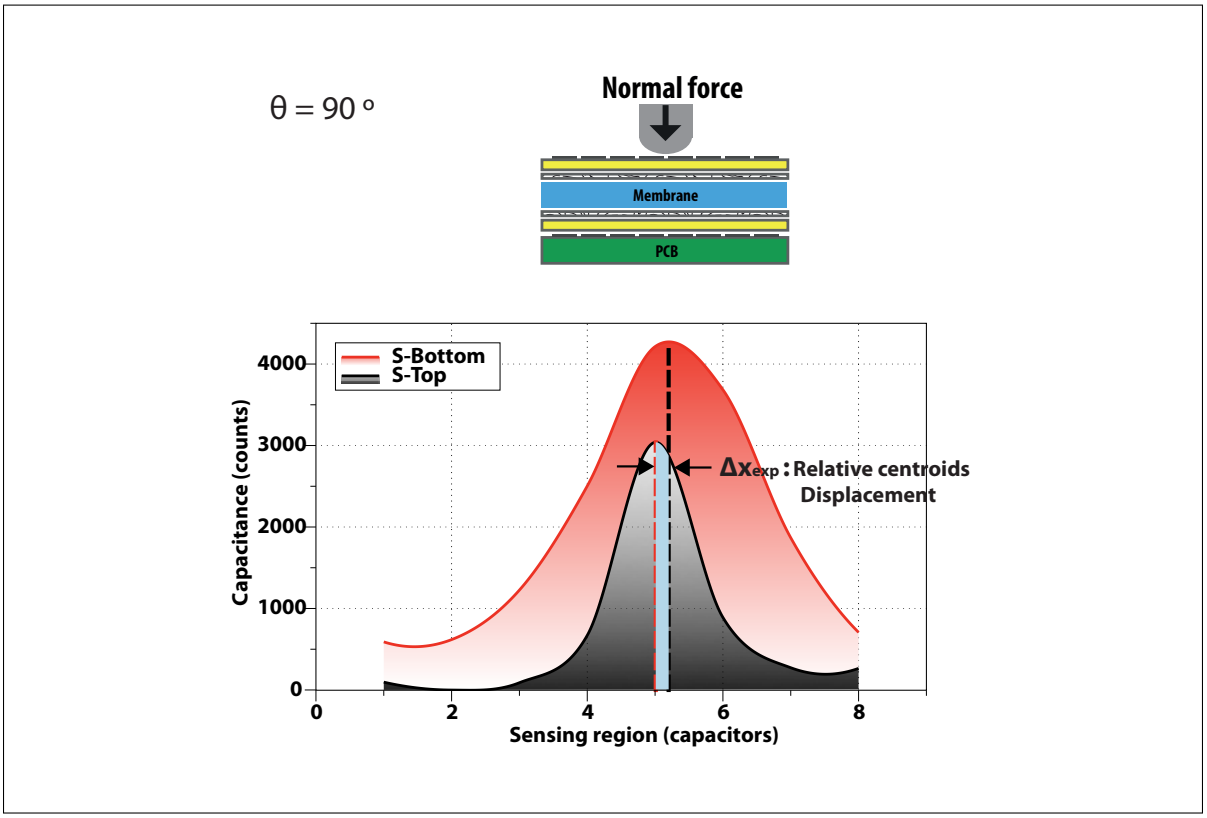

Figure 4.17 Sensing element stress images under a force-application angle of $\theta = 90°$

The second and third scenarios provided stress images when the respective angles of loading were equal to $\theta = 86.5°$ and $\theta = 82.5°$. From Figures 4.18 and 4.19, we can see that the recorded S-Top and S-Bottom images are skewed, due to the application of a shear force (f_x) in addition to a normal force. These figures also show how the relative change in the locations

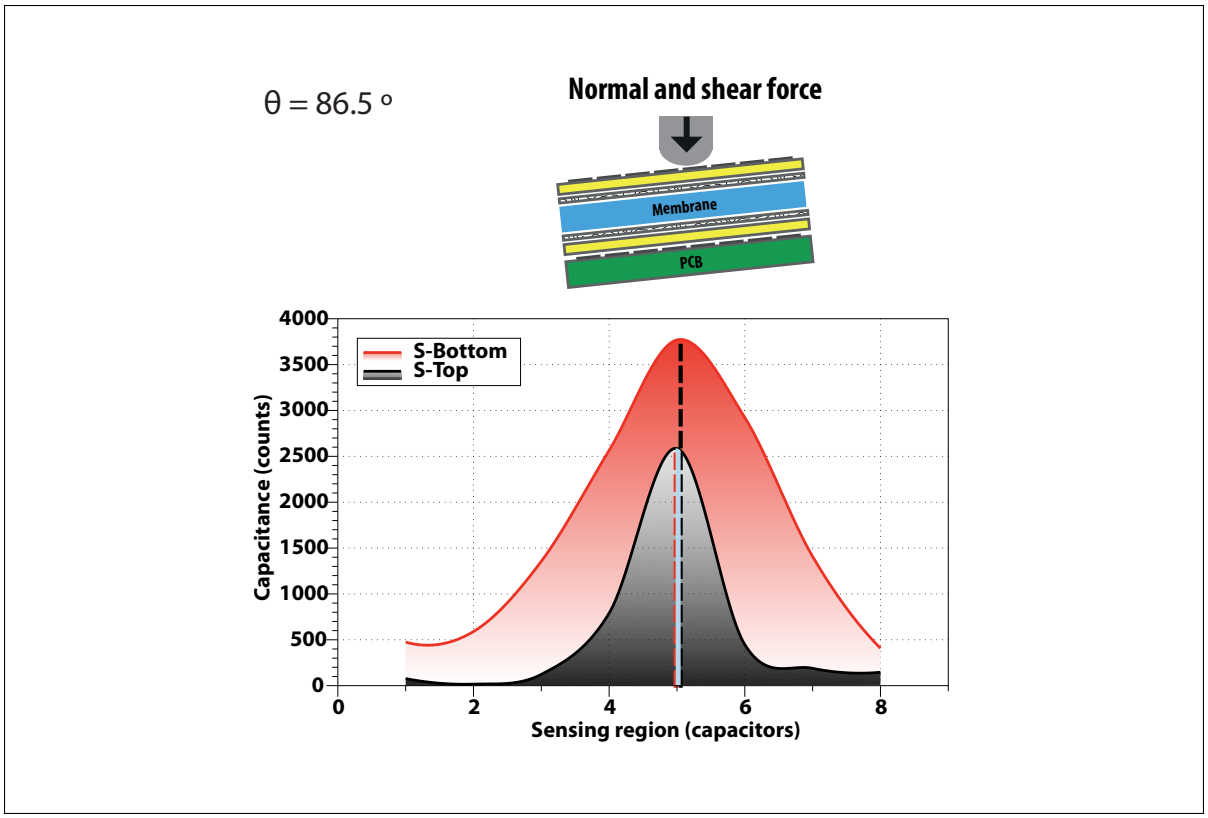

Figure 4.18 Sensing element stress images under a force-application angle of $\theta = 86.5°$

of the centroids, Δx_{exp}, relates to the angle of loading, θ. As can be seen, a higher value of Δx_{exp} corresponds to a lower value of θ. This is most evident in the case in which the shear force exhibits the maximum magnitude. Recall that magnitude of stress (denoted below by τ) depends, through the maximum value of the stress in S-Top's image, upon the normal component of the applied force.

In addition, we tested the performance of decoupling the components of the force that was applied to the sensing element. We fitted the relationship between the parameter τ and the angle of loading θ. We also used the data recorded from the experiment to plot the relationship between the parameter Δx_{exp} and the angle of loading θ. Figure 4.20 displays the results. We opted for third-order polynomials instead of linear fittings, to preserve the slightly nonlinear trends of the relationships. The coefficients of the polynomials were computed using the standard linear least squares method. The parameter τ ranges from 2800 to 4200 counts, while the

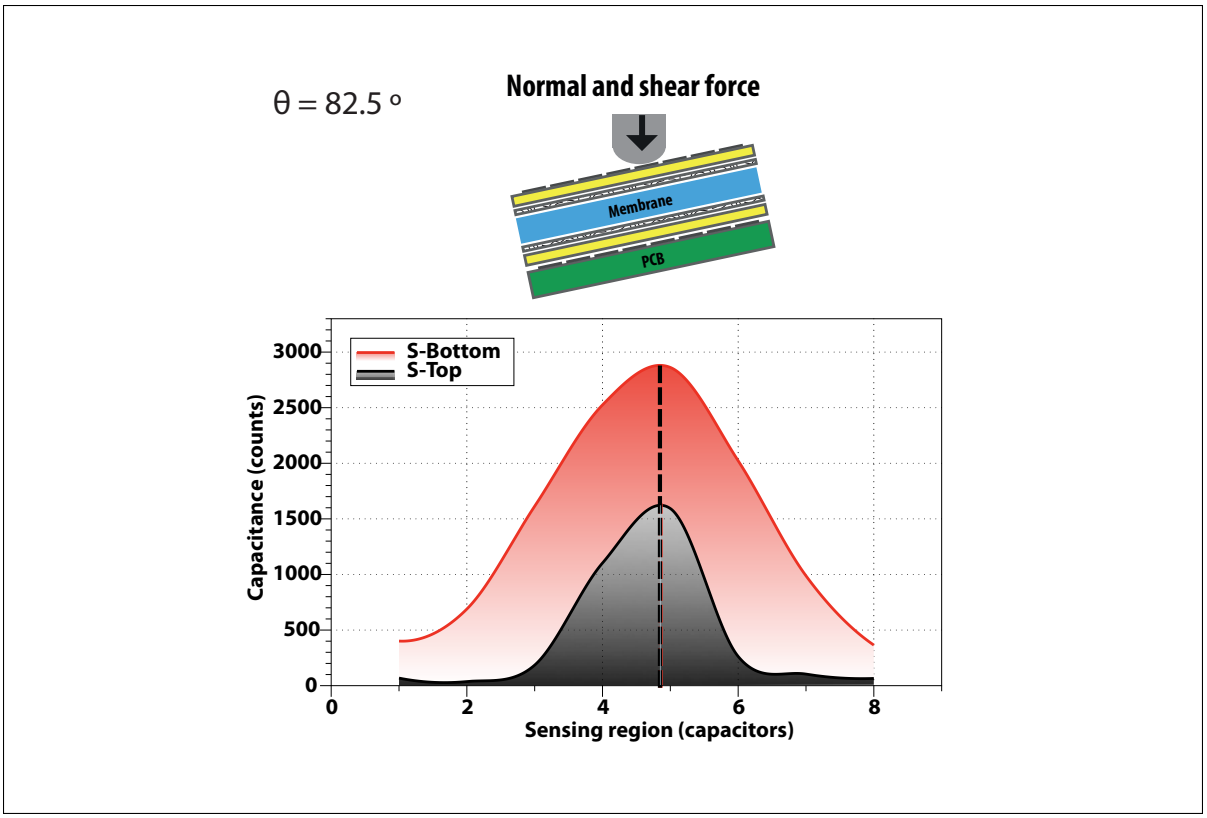

Figure 4.19 Sensing element stress images under a force-application angle of $\theta = 82.5°$

relative displacement of the centroids is between -265 and 13 counts. From these values, we infer that the predictions of the theoretical model are correct: the parameter τ is more sensitive to force in the z-direction, and the parameter Δx_{exp} is more sensitive to force in the x-direction.

With these relationships, and some simple trigonometric equations, we can now reconstruct the two force components. This is possible due to our correct prediction of the inverse relationship between the angle of loading and the shear force: as the value of the angle of loading, θ, gets larger, the value of the applied shear force decreases, and the value of the applied normal force increases. The results of our force reconstruction calculations, shown in Figure 4.21, confirm this relationship and verify our ability to use the sensing element to measure normal and shear force separately.

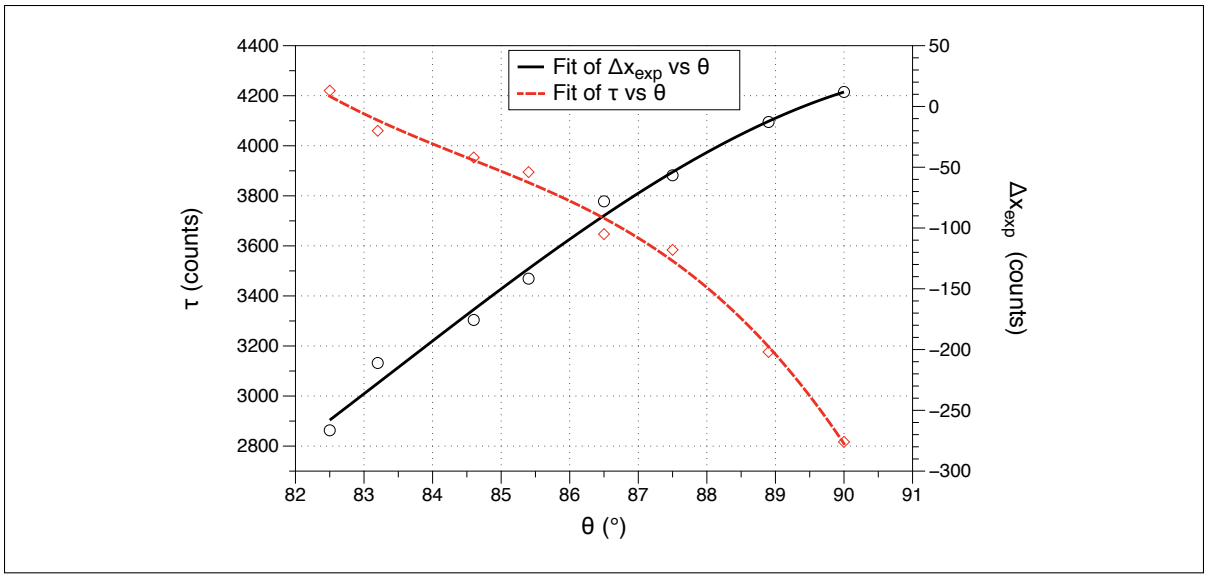

Figure 4.20 Fitting the parameters obtained from the characterization results

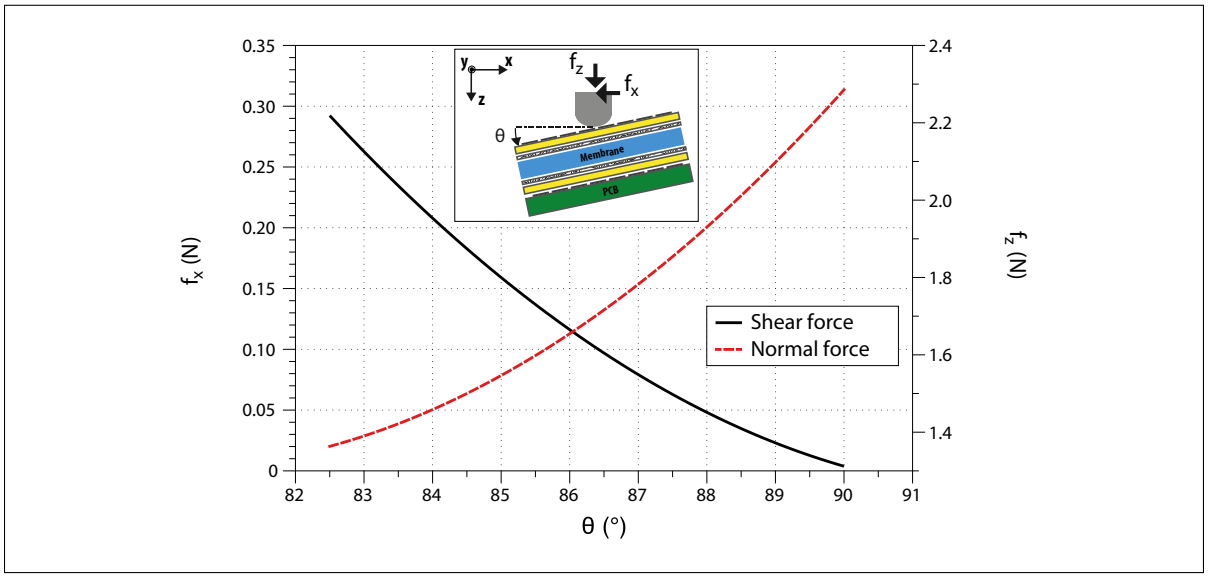

Figure 4.21 Force estimation results

4.6 Conclusion

We have presented a novel method for designing a multi-axial stress-sensing element. Our use of stress diffusion theory allowed us to develop a single sensing element that measures normal

stress, shear stress, and torque. In future research, we hope to apply this method to the design of a six-axis sensing element, in order to develop a six-axis force-torque sensor. As our design is compact and requires minimal assembly, we believe a six-axis sensing element based on our method will be ideal for use in robotic artificial skin. Eventually, our design may help robots to quickly and precisely determine the quality of a static grasp, object slippage, etc.

In this chapter, we verified our design assumptions by fabricating a triaxial sensing element. The sensing element, made of layers of silicone and conductive electrodes, met our objectives regarding compactness and measurement performance. However, we found that it is not very sensitive to higher values of shear force (i.e., it is not sensitive to shear forces applied at angles ranging from 0 to 82.5°). Given that most applications of multi-axis force-torque sensors require the sensor to be capable of detecting a wide range of forces, this is a significant drawback. Before we can achieve our goal of a six-axis force-torque sensor, then, we must first conduct more research to extend the range of our triaxial sensing element.

CONCLUSION

This project is part of the team effort, led by Vincent Duchaine, to enhance the human-robot physical interactivity. In this context, the design of multi-axis force-torque sensors is an important aspect of efficient and safe collaboration. The objective of this thesis is the development of new methods of designing multi-axis force-torque sensors. These methods must enable systematic design of any multi-axis force-torque sensor by reproducing, as faithfully as possible, the forces applied to it.

The present work was separated into three parts. Chapter 2 introduced a novel method of optimizing the compliant mechanism that forms the core of multi-axis force-torque sensors. We used the geometrical relationships of the compliant structure to formulate several indices. These indices are used in the multi-objective optimization process, based on Pareto-optimization, to find the best design geometry.

In Chapter 3, we presented a new design method that is based on the mechanical behavior of the compliant structure. We formulated a systematic design method, by using the symbolic relations between wrenches and displacements, and the specifications of the application. Assuming that the compliant elements can be modeled as Euler-Bernoulli beams, this approach may be applied to any compliant structure, providing a symbolic formulation of the wrench-displacement relationship. Since fabrication limitations are included in the optimization procedure, the multi-axis force-torque sensor can easily be manufactured. Finally, the optimization method takes into account that there is no contact between the sensing element and the compliant structure; so, our optimization method does not require any information on the properties of the sensing element.

Chapter 4 proposed the concept of a new transduction technique that is intended use in future multi-axis force-torque sensors. We also designed a new sensing element, based on the theoretical concept of this transduction technique. In this chapter we described the working principle and the choice of technology of the new sensing element. Finally, we verified our design assumptions by fabricating a triaxial sensing element. This sensing element was made of

layers of silicone and conductive electrodes, and it met our objectives regarding compactness and measurement performance.

Original contributions

The following aspects of this thesis represent its original contributions:

- The geometrical model in the design of the compliant structure is based on performance indices that explicitly relate the performance criteria to the sensor's geometry and its dimensional parameters. Unlike past optimization methods, this one is based on performance indices, which ensures that the designer will be able to obtain a sensor that meets the specifications of the intended application.
- The systematic design method proposed in Chapter 3 considers the mechanical parameters that characterize the sensor design, such as the dimension, material proprieties, machining process, transduction, etc. No other approach has taken all these parameters into consideration at the same time. This approach can be used for the design of compliant structures for accelerometers, and of compliant manipulators.
- With our new transduction technique, it is now possible to design a six-axial sensing element. This is because our two arrays of capacitive electrodes are capable of measuring stress distributions at two levels. The use of one six-axial sensing element, instead of several uni-axial sensing elements, negates the need for a sizeable network of sensing elements, and consequently lowers the total dimensions, and the cost, of the multi-axis force-torque sensor.

Discussion

The triaxial force sensor presented in this work illustrates the applicability of our proposed methods to real design problems. Our current sensor has shown very satisfactory results. This type of solution, which combines an optimized compliant structure with capacitive technology,

seems promising for future development. Our sensor design has already been used by MIT, for integration with an electromechanical active prosthetic socket for above-knee amputees. Robotiq Inc. has also used our systematic design method to develop their own six-axis force-torque sensor (called the FT 150) that is compatible with several industrial robots, and is currently available for purchase.

These results are very encouraging, but nevertheless, we are certain that our design method that can be improved upon in future work. One limitation of our proposed approach is specifically related to the inclusion of the sensing element technology in the optimization procedure. Since the capacitive sensing element was designed separately from the mechanical structure, we optimized each of the factors separately, rather than developing a global optimization method. It is possible that a global optimization procedure, one that accounts for the sensor electronics, geometry and mechanics simultaneously, will perform better than our current sensor.

REFERENCES

Beyeler, F., S. Muntwyler, and B. J. Nelson. 2009a. "Design and calibration of a microfabricated 6-axis force-torque sensor for microrobotic applications". In *Robotics and Automation, 2009. ICRA'09. IEEE International Conference on*. p. 520–525. IEEE.

Beyeler, F., S. Muntwyler, and J. Nelson, Bradley. 2009b. "A Six-axis MEMS Force–torque Sensor with Micro-Newton and Nano-Newtonmeter Resolution". *Journal of Microelectromechanical Systems*, vol. 18, n° 2, p. 433–441.

Bicchi, A. 1992. "A Criterion for Optimal Design of Multi-axis Force Sensors". *Robotics and Autonomous Systems*, vol. 10, n° 4, p. 269-286.

Brookhuis, R. A., R. J. Wiegerink, T. S. J. Lammerink, and G. J. M. Krijnen. Nov 2013. "Three-axial force sensor with capacitive read-out using a differential relaxation oscillator". In *SENSORS, 2013 IEEE*. p. 1-4.

Cardou, P., D. Pasini, and J. Angeles. 2008. "Lumped Elastodynamic Model for MEMS: Formulation and Validation". *IEEE Journal of Microelectromechanical Systems*, vol. 17, n° 4, p. 948–961.

Carpi, F., D. De Rossi, R. Kornbluh, R. E. Pelrine, and P. Sommer-Larsen, 2011. *Dielectric elastomers as electromechanical transducers: Fundamentals, materials, devices, models and applications of an emerging electroactive polymer technology*.

Censor, Y. 1977. "Pareto Optimality in Multiobjective Problems". *Applied Mathematics and Optimization*, vol. 4, p. 41–59.

Chao, L.-P. and K.-T. Chen. 1997. "Shape Optimal Design and Force Sensitivity Evaluation of Six-Axis Force Sensors". *Sensors and Actuators A: Physical*, vol. 63, n° 2, p. 105-112.

Chapuis, D., R. Gassert, L. Sache, E. Burdet, and H. Bleuler. 2004. "Design of a simple MRI/fMRI compatible force/torque sensor". In *Intelligent Robots and Systems, 2004.(IROS 2004). Proceedings. 2004 IEEE/RSJ International Conference on*. p. 2593–2599. IEEE.

Chen, W., J. Jiang, W. Chen, and J. Liu. 2013. "A Novel Flexure-Based Uniaxial Force Sensor With Large Range and High Resolution". *Science China Technological Sciences*, vol. 56, n° 8, p. 1940-1948.

Chen, X. and Y. Li. May 1997. "On the Dynamic Behavior of a Wrist Force Sensor for Robots". In *Instrumentation and Measurement Technology Conference, 1997. IMTC/97. Proceedings. Sensing, Processing, Networking., IEEE*. p. 963-968.

Cherney, E. 2005. "Silicone rubber dielectrics modified by inorganic fillers for outdoor high voltage insulation applications". *Dielectrics and Electrical Insulation, IEEE Transactions on*, vol. 12, n° 6, p. 1108–1115.

Dahiya, R. and M. Valle. 2013. Human tactile sensing. *Robotic Tactile Sensing*, p. 19-41. Springer Netherlands.

Diddens, D., D. Reynaerts, and H. Van Brussel. 1995. "Design of a ring-shaped three-axis micro force/torque sensor". *Sensors and Actuators A: Physical*, vol. 46, n° 1, p. 225–232.

Doebelin, E., 1985. *Measurement Systems Application and Design 5*, volume 5. 434-480 p.

Dwarakanath, T., B. Dasgupta, and T. Mruthyunjaya. 2001. "Design and Development of A Stewart Platform Based Force-Torque Sensor". *Mechatronics*, vol. 11, n° 7, p. 793-809.

Eslami, M., 2005. *Circuit Analysis Fundamentals*. ed. 1st.

Golub, G. and C. Van Loan, 1996. *Matrix Computations*. Baltimore, MD : Johns Hopkins University Press.

Grahn, A. and L. Astle. 1984. "Robotic Ultrasonic Force Sensor Arrays". In *Proceedings of the Robots 8 Conference*. p. 1-18.

Gu, L., Q.-A. Huang, and M. Qin. 2004. "A novel capacitive-type humidity sensor using CMOS fabrication technology". *Sensors and Actuators B: Chemical*, vol. 99, n° 2, p. 491–498.

Hirose, S. and K. Yoneda. 1990. "Developement of Optical 6-axial Force Sensor and Its Signal Calibration Considering Non-linear Interfrence". *internal report, Tokyo Institute of technology*.

Jia, Z.-Y., S. Lin, and W. Liu. 2010. "Performance Index Analysis of A Six-Axis Heavy Force Sensor Based on the Stewart platform". *Proceedings of the Institution of Mechanical Engineers, Part C: Journal of Mechanical Engineering Science*, vol. 224, n° 6, p. 1359-1368.

Jin, Z., F. Gao, and X. Zhang. 2003. "Design and analysis of a novel isotropic six-component force/torque sensor". *Sensors and Actuators. A, Physical*, vol. 109, n° 1-2, p. 17-20.

Kang, C. G. 2001. "Closed-form force sensing of a 6-axis force transducer based on the Stewart platform". *Sensors and Actuators. A, Physical*, p. 31-37.

Kao,I. Chen, S. F. 2000. "Conservative Congruence Transformation for Joint and Cartesian Stiffness Matrices of Robotic Hands and Fingers". *The International Journal of Robotics Research*, vol. 19, n° 9, p. 835-847.

Kim, G.-S. 2004. "Development of a small 6-axis force/moment sensor for robot's fingers". *Measurement Science and Technology*, vol. 15, n° 11, p. 2233.

Kvasnica, M. 1992. "Six-component force-torque sensing by means of one square CCD or PSD element". In *Proc of International Symposium on Measurement and Control in Robotics*. p. 213-219.

Liang, Q., D. Zhang, Y. Wang, and Y. Ge. 2013. "Design and Analysis of a Novel Six-Component F/T Sensor based on CPM for Passive Compliant Assembly". *Measurement Science Review*, vol. 13, p. 253-264.

Liang, Q.-a., Q.-J. Song, D. Zhang, Y.-J. Ge, G.-B. Zhang, H.-B. Cao, and Y. Ge. 2010. "Design of a Novel Six-dimensional Force/Torque Sensor and Its Calibration Based on NN". In *Proceedings of the 6th International Conference on Advanced Intelligent Computing Theories and Applications: Intelligent Computing*. p. 1-8.

Liu, S. A. and H. L. Tzo. 2002. "A Novel Six-Component Force Sensor of Good Measurement Isotropy and Sensitivities". *Sensors and Actuators A: Physical*, vol. 100, n° 2-3, p. 223-230.

Liu, T., Y. Inoue, K. Shibata, Y. Yamasaki, and M. Nakahama. Dec 2004. "A Six-Dimension Parallel Force Sensor for Human Dynamics Analysis". In *Robotics, Automation and Mechatronics, 2004 IEEE Conference on*. p. 208-212.

Liu, T., Y. Inoue, and K. Shibata. Oct 2008. "Design of low-cost tactile force sensor for 3D force scan". In *Sensors, 2008 IEEE*. p. 1513-1516.

McCarthy, J., 1990. *Methodology and tools in telemanipulation systems via internet*, volume 1.

Merlet, J.-P., 1997. *Parallel Robots*.

Nakamura, Y., T. Yoshikawa, and I. Futamata. 1988. "Design and Signal Processing of Six-Axis Force Sensors". In *Proceedings of the 4th International Symposium on Robotics Research*. (Cambridge, MA, USA 1988), p. 75–81. MIT Press.

Norberto Pires, J., J. Ramming, S. Rauch, and R. Araújo. 2002. "Force/torque sensing applied to industrial robotic deburring". *Sensor Review*, vol. 22, n° 3, p. 232-241.

Peirs, J., J. Clijnen, D. Reynaerts, H. V. Brussel, P. Herijgers, B. Corteville, and S. Boone. 2004. "A Micro Optical Force Sensor for Force Feedback During Minimally Invasive Robotic Surgery". *Sensors and Actuators: Physical*, vol. 115, n° 2, p. 447–455.

Perry, D. M. 1997. "Multi-axis Force and Torque Sensing". *Sensor Review*, vol. 17, n° 2, p. 117–120.

Peshkin, M. 2007. "Mutual Inductance Force Sensor". *Transfer Program NU20084*.

Piller, G. 1982. "A compact six degree-of-freedom force sensor for assembly robot". In *Proc of the 12th International Symposium on Industrial Robots*. p. 121-129.

Puangmali, P., H. Liu, L. Seneviratne, P. Dasgupta, and K. Althoefer. Aug 2012. "Miniature 3-Axis Distal Force Sensor for Minimally Invasive Surgical Palpation". *Mechatronics, IEEE/ASME Transactions on*, vol. 17, n° 4, p. 646–656.

Ranganath, R., P. Nair, and T. Mruthyunjaya. 2004a. "A force-torque sensor based on a Stewart Platform in a near-singular configuration". *Mechanism and machine theory*, vol. 39, n° 9, p. 971-998.

Ranganath, R., P. Nair, T. Mruthyunjaya, and A. Ghosal. 2004b. "A Force-Torque Sensor Based on a Stewart Platform in a Near-Singular Configuration". *Mechanism and Machine Theory*, vol. 39, n° 9, p. 971-998.

Ricciardi, G. and L. Borsati. 1993. "Six Axis of Sensitivity Force Sensors for Robots". *{CIRP} Annals - Manufacturing Technology*, vol. 42, n° 1, p. 597-601.

Salisbury, J. K. 1980. "Active stiffness control of a manipulator in Cartesian coordinates". *19th IEEE Conference on Decision and Control*, vol. 19, p. 95-100.

Scheinman, V. D. 1969. "Design of a Computer Controlled Manipulator". *Stanford university of California - department of computer science*.

Sorli, M. and S. Pastorelli. 1995. "Six-Axis Reticulated Structure Force/Torque Sensor With Adaptable Performances". *Mechatronics*, vol. 5, n° 6, p. 585-601.

Takahashi, N., M. Tada, J. Ueda, Y. Matsumoto, and T. Ogasawara. 2003. "An Optical 6-axis Force Sensor for Brain Function Analysis Using FMRI". In *Sensors, Proceedings of IEEE*. p. 253–258. IEEE.

Uchiama, M., E. Bayo, and E. Palmavillalon. 1991. "A Systematic Design Procedure to Minimize a Performance Index for Robot Force Sensors". *Journal of dynamic systems measurement and control-transaction of the ASME*, vol. 113, n° 3, p. 388-394.

Uchiyama, M. and K. Hakomori. 1985. "A Few Considerations on Structural Design of Force Sensors". In *3rd Annual Conference on Japanese Robotics Society*.

Uchiyama, M. and M. Svinin. 1995. "Optimal Geometric Structures of Force/Torque Sensors". *The International journal of robotics research*, vol. 14, n° 6, p. 560-573.

Uchiyama, U., E. Bayo, and E. Palma-Villalon. 1988. "A Mathematical Approach to the Optimal Structural Design of a Robot Force Sensor". In *USA-JAPAN Symposium on Flexible Automation*. p. 539-546.

Ulmen, J. and M. Cutkosky. 2010. "A robust, low-cost and low-noise artificial skin for human-friendly robots". In *Robotics and Automation (ICRA), 2010 IEEE International Conference on*. p. 4836–4841. IEEE.

Weiyi, H., J. Hongming, and Z. Hanqing. 1993. "Mechanical Analysis of a Novel Six-Degree-of-Freedom Wrist Force Sensor". *Sensors and Actuators A: Physical*, vol. 35, n° 3, p. 203-208.

Whitney, D. T. 1985. "Historical Perspective and State of the Art in Robot Force Control". In *Robotics and Automation. IEEE International Conference*. p. 262–268. IEEE.

Xin, Z. Oct 2009. "Design of a New Type Six-Axis Force Sensor". In *Intelligent Computation Technology and Automation, 2009. ICICTA '09. Second International Conference on*. p. 446-449.

Yoshikawa, T. 1985. "Manipulability of Robotic Mechanisms". *The International Journal of Robotics Research*, vol. 4, n° 2, p. 3–9.

Young, D. J., J. Du, C. A. Zorman, and W. H. Ko. 2004. "High-temperature single-crystal 3C-SiC capacitive pressure sensor". *Sensors Journal, IEEE*, vol. 4, n° 4, p. 464–470.

Yu, Y., T. Chaen, and S. Tsujio. 2006. "High-Stiffness and High-Sensitivity 3-Axis Force Sensor Using Strain-Deformation Expansion Mechanism". In *IROS*. p. 4417-4422. IEEE.

Yussof, H., S. C. Abdullah, and M. Ohka. May 2010. "Development of Optical Three-Axis Tactile Sensor and its Application to Robotic Hand for Dexterous Manipulation Tasks". In *Mathematical/Analytical Modelling and Computer Simulation (AMS), 2010 Fourth Asia International Conference on*. p. 624-629.

Zhenlin, J., G. Feng, and Z. Xiaohui. 2003. "Design and Analysis of A Novel Isotropic Six-Component Force/Torque Sensor". *Sensors and Actuators A: Physical*, vol. 109, n° 1-2, p. 17-20.